SANDIA REPORT
SAND2009-6622
Unlimited Release
September 2009

Microstructure-Based Approach for Predicting Crack Initiation and Early Growth in Metals

Luke N. Brewer, Corbett C. Battaile, Remi P.M. Dingreville, Timothy J. Bartel, Earl D. Reedy, James V. Cox, Jay W. Foulk, John M. Emery, Brad L. Boyce, J.D. Puskar

Prepared by
Sandia National Laboratories
Albuquerque, New Mexico 87185 and Livermore, California 94550

Sandia is a multiprogram laboratory operated by Sandia Corporation,
a Lockheed Martin Company, for the United States Department of Energy's
National Nuclear Security Administration under Contract DE-AC04-94AL85000.

Approved for public release; further dissemination unlimited.

Sandia National Laboratories

Issued by Sandia National Laboratories, operated for the United States Department of Energy by Sandia Corporation.

NOTICE: This report was prepared as an account of work sponsored by an agency of the United States Government. Neither the United States Government, nor any agency thereof, nor any of their employees, nor any of their contractors, subcontractors, or their employees, make any warranty, express or implied, or assume any legal liability or responsibility for the accuracy, completeness, or usefulness of any information, apparatus, product, or process disclosed, or represent that its use would not infringe privately owned rights. Reference herein to any specific commercial product, process, or service by trade name, trademark, manufacturer, or otherwise, does not necessarily constitute or imply its endorsement, recommendation, or favoring by the United States Government, any agency thereof, or any of their contractors or subcontractors. The views and opinions expressed herein do not necessarily state or reflect those of the United States Government, any agency thereof, or any of their contractors.

Printed in the United States of America. This report has been reproduced directly from the best available copy.

Available to DOE and DOE contractors from
U.S. Department of Energy
Office of Scientific and Technical Information
P.O. Box 62
Oak Ridge, TN 37831

Telephone: (865) 576-8401
Facsimile: (865) 576-5728
E-Mail: reports@adonis.osti.gov
Online ordering: http://www.osti.gov/bridge

Available to the public from
U.S. Department of Commerce
National Technical Information Service
5285 Port Royal Rd.
Springfield, VA 22161

Telephone: (800) 553-6847
Facsimile: (703) 605-6900
E-Mail: orders@ntis.fedworld.gov
Online order: http://www.ntis.gov/help/ordermethods.asp?loc=7-4-0#online

SAND2009-6622
Unlimited Release
Printed September 2009

Microstructure-Based Approach for Predicting Crack Initiation and Early Growth in Metals

Luke N. Brewer, Corbett C. Battaile, Remi P.M. Dingreville, Timothy J. Bartel, Earl D. Reedy, James V. Cox, Jay W. Foulk, John M. Emery, Brad L. Boyce, J.D. Puskar

Sandia National Laboratories
P.O. Box 5800
Albuquerque, New Mexico 87185-MS0889

Abstract

Fatigue cracking in metals has been and is an area of great importance to the science and technology of structural materials for quite some time. The earliest stages of fatigue crack nucleation and growth are dominated by the microstructure and yet few models are able to predict the fatigue behavior during these stages because of a lack of microstructural physics in the models. This program has developed several new simulation tools to increase the microstructural physics available for fatigue prediction. In addition, this program has extended and developed microscale experimental methods to allow the validation of new microstructural models for deformation in metals. We have applied these developments to fatigue experiments in metals where the microstructure has been intentionally varied.

ACKNOWLEDGMENTS

We would like to acknowledge a great deal of assistance in preparing and measuring brass material from Mark Reece, Bonnie McKenzie, David Schmale, Alice Kilgo, and Garry Bryant.

We would also like to thank the leadership of organizations 1800, 1500, 1400, and what was previously 8700 for supporting this work.

CONTENTS

1. Introduction. 13
Section 1 References: 13

2. Experimental Methods for Observing Microstructural Mechanics. 15
2.1. New capabilities for electron backscatter diffraction (EBSD) (L.N. Brewer (01814), B.L. Boyce (01813), D.S. Schmale (01813) and J.R. Michael (01822)) 15
2.1.1 In situ testing methods. 15
2.1.2. Three dimensional FIB-EBSD 17
2.2. Quantification of Agreement between Experiment and Simulation (L.N. Brewer (01814) and C.C. Battaile (01814)) 19
Section 2 References: 26

3. Simulation Methods for Predicting Microstructural Plasticity and Crack Behavior. 29
3.1. Material Point Method in elasto-plastic deformation at finite strains: Crystal plasticity capabilities in MPALE. (R.P.M. Dingreville (01814), T.J. Bartel (06774), and C.C. Battaile (01814)) 29
3.1.1. Introduction 29
3.1.2 Material Point Method 30
3.1.3 Microstructure-based model 34
3.1.4 Numerical Examples for Crystal Plasticity 37
3.2. Stress Fields Generate by Surface Triple-Grain Junctions: Illustrative Finite Element Results (E.D. Reedy (01526) 41
3.2.1 Introduction 41
3.2.2 Analysis 42
3.2.3 Results 43
3.2.4 Discussion 51
3.2.5 Summary 54
3.3. Advancement in an Analytically Enriched XFEM (J.V. Cox (01524)) 56
3.3.1 Introduction 56
3.3.2 Previous SNL Work on the Analytically Enriched XFEM 57
3.3.3 Extensions to Mixed-Mode Fracture 57
3.3.4 Application to an Orthotropic Material 59
3.3.5 Closure 64
Section 3 References: 65

4. Applications. 70
4.1. Cyclic plasticity applied to nickel microstructures. (R.P.M. Dingreville (01814), C.C. Battaile (01814), L.N. Brewer (01814), and B.L. Boyce (01813)) 70
4.1.1 Methods for coupling experiments and simulations 71
4.1.2 Cyclic ratcheting 76
4.1.3 Limitations of the present approach 82
4.2. Inclusion of microstructure to small crack growth in hydrogen embrittlement problems 83
4.2.1 Hydrogen transport and coupling methodology. 83
4.2.2 An examination of the hydrostatic stress ahead of a crack tip. 84
4.2.3 Discussion and conclusions. 87

4.3. Systematically varied microstructures for model development and testing (L.N. Brewer (01814), J.D. Puskar (01822), B.L. Boyce (01813), C.C. Battaile (01814)) 88
4.3.1 Introduction 88
4.3.2 Production of brass materials 88
4.3.3 Monotonic, uniaxial, tension experiments 91
4.3.4 Cyclic, uniaxial, tension experiments..... 93
Section 4 References: 95

5. Connection to the future: including microstructural physics into component level predictions using probabilistic descriptions. (C.C. Battaile (01814), L.N. Brewer (01814), and J.M. Emery (01524))..... 99
Section 5 References: 101

Distribution 103

FIGURES

Figure 2.1 Design drawing of novel in situ straining stage for EBSD. (left) Test stress-strain curve on 304 stainless steel using the in situ stage. (right)…..……..….16

Figure 2.2 Inverse pole figure maps (with respect to x-tensile direction) for three grain sizes of brass strained to three different levels acquired using new in situ straining stage……...…….……...…17

Figure 2.3 Electron image (left) and ion image (right) of sample being milled during three dimensional EBSD experiment……...…18

Figure 2.4. Three dimensional EBSD data set from electrodeposited nickel material…….19

Figure 2.5. Flowchart for preparing EBSD and FEM data for quantitative comparison……21

Figure 2.6. Preparation of data from nickel polycrystal for quantitative comparison between EBSD and FEM……..……..22

Figure 2.7. EBSD data shifted and interpolated to FEM coordinate system (A). Misorientation map created by calculating and plotting the scalar, misorientation angle for each pixel (B)…….…...22

Figure 2.8. Misorientation maps comparing EBSD and FEM for increasing levels of strain……..……..……..24

Figure 2.9. Mean misorientation between EBSD and FEM for local and non-local crystal plasticity models……...……25

Figure 2.10. Normalized area match fraction plots comparing EBSD and FEM data using local and non-local crystal plasticity models……..……26

Figure 3.1. Space discretization composed of material points and computational grid…….31

Figure 3.2. Implementation of crystal plasticity in MPALE……..37

Figure 3.3. Comparison FEM (JAS3D, implicit time integration) vs. MPM (MPALE, implicit time integration) on a single crystal……..……...39

Figure 3.4. Comparison FEM (JAS3D, implicit time integration) vs. MPM (MPALE, implicit time integration) on a polycrystal……..……...40

Figure 3.5. Geometry of problem analyzed, uniformly displace right edge relative to fixed left edge in a direction parallel to the stress-free edge to generate a nominally uniform s_{11}=s……..……...42*

Figure 3.6. Radial stress dependence at pt1 (q=0°) and pt2 (q=180°) for baseline geometry and material…….....…...44

Figure. 3.7. Angular dependence of singular stress at pt1 for baseline geometry and material……..45

Figure. 3.8. Deformed geometry (highly magnified) for baseline geometry and material…….……46

Figure 3.9. FEA results for the variation of -l with g_a at pt1 of the baseline configuration with g_a=g_c=-g_d, and g_b= 0° are compared with asymptotic -l values determined using the Stroh formalism for anisotropic elasticity…….…….……49
`

Figure 3.10. Geometry of model used to examine effect of surrounding a crystal with larger crystals……..…….……51

Figure 3.11. Deformed geometry (highly deformed) for case where w_1=90° and with g_a=45°, g_b=0°, g_c= 45°, and g_d=-45°…….……..51

Figure 3.12. Problem analyzed to determine w, g_a and g_b combinations that generate a continuous s_{rr} across the grain boundary……54

Figure 3.13. Curved crack segment association……..58

Figure 3.14. Model problem at the state of the cohesive crack extending to the center……60

Figure 3.15. Reference solution mesh – 81x80……..60

Figure 3.16. Relative errors vs. element size for bending problem with approximate reference solution, n=0.17, and 2x2 quadrature…….……62

Figure 3.17. Relative errors vs. element size for bending problem with approximate reference solution, n=0.17, and 4x4 quadrature……..62

Figure 3.18. Relative errors vs. element size for bending problem, uncracked and cracked……...64

Figure 3.19. Relative error in U and ∇U vs. E_1/E_2, with E_1 varying (5x5 XFEM mesh)……..64

Figure 4.1. Methodology for coupling microstructure characterization, mechanical testing and numerical simulations……...71

Figure 4.2. Microstructure of the areas of interest (a) revealed by EBSD measurements and (b) digitized for the numerical simulations. (c) The Inverse Pole Figures (IPFs) represent the raw grain orientations measured by EBSD with respect to the loading axis. The colors of the IPFs correspond directly to the colors of the grains……73

Figure 4.3. (a) Representative microstructure composed of 199 grains with periodicity constraints on the edges. (b) Stress vs strain from experiment (black symbols), and from a simulation using best-fit constitutive parameters and grain orientations on the microstructure in (a)……...……74

Figure 4.4 Comparison for (a., left) the representative microstructure and simulated stress-strain responses for stress-controlled cyclic tests, (b., right) the accumulation of plastic deformation as a function of the cyclic history. The anisotropic Taylor hardening model, with averaged orientations per grain, was used in this set of simulations. The different areas are labeled in Figure 2……....77

Figure 4.5 Illustration of the two stages of ratcheting. Equivalent plastic deformations higher than 1×10^{-2} are plotted for Area 1 (i.e no coloring corresponds to plastic strain lower than this threshold) in the case of the Taylor hardening model with averaged orientation per grain. Note that the regions close to the edges of the simulation box presented in Figure 4.(b) have been omitted……..……78

Figure 4.6 Different idealized microstructure morphologies used to assess the influence of the microstructure on ratcheting: (a) square microstructure with one element per grain, (b) square microstructure with 100 elements per grains, (c) regular hexagonal microstructure, (d) distorted hexagonal microstructure, (e) digitized microstructure (Area 1), and (f) shuffled digitized microstructure (Area 1). Colors are assigned randomly and do not correspond to any properties……..……79

Figure 4.7. Effect of microstructure on the accumulation of plastic deformation as a function of the cyclic history. The anisotropic Taylor hardening model was used in this set of simulations. Area 1 is labeled in Figure 2…….……80

Figure 4.8. An outline of deriving the hydrogen transport partial differential equation and a schematic of the segregated coupling scheme between the Sierra codes Aria and Adagio. Hydrogen transport is solved in the reference configuration……..……...…84

Figure 4.9. Comparison between measured and synthetic microstructures. Both nickel microstructures have an average grain size of 33 μm…….85

Figure 4.10. Applied, far-field K-field displacement boundary condition…….85

Figure 4.11. Variation in the number of polycrystalline grains around the crack tip. For this randomly orientated microstructure, added grains only perturb the solution. The simulated grain size is 500 μm……..86

Figure 4.12. Differences in the hydrostatic stress field as a function of the modeling methodology. The simulated grains size is 33 μm……..87

Figure 4.13. Drawing and image of tensile bar geometry. Dimensions are in inches…….89

Figure 4.14. Pole figures from recrystallized brass as a function of grain size. (Note: x is the rolling direction and the tensile direction)……..…….90

Figure 4.15 Hall-Petch plot for cartridge brass. The two sets of data represent grain size measurements taken with and without including twin boundaries……...…….91

Figure 4.16 Inverse pole figure maps (with respect to x-tensile direction) for three grain sizes of brass strained to three different levels……..……...92

Figure 4.17 LIMIS plots for three grain sizes of brass strained to three different levels. For all figures, blue is 0º misorientation and red is 15º misorientation…….….93

Figure 4.18 Orientation (inverse pole figure) and LIMIS maps for brass before (A and C) and after fatigue. The maps in this figure are for brass heat treated at 400ºC for 2 hours with 5 cycles at 1% strain per cycle for a total strain of 5%.....94

Figure 4.19 Combination of atomic force microscope (AFM) image (left, amplitude image) and EBSD orientation map (right, inverse pole figure) showing the same areas after fatigue of brass samples (450C, 2hrs) with 5 cycles at 1% strain per cycle…….....95

Figure 4.20 Orientation (inverse pole figure) and LIMIS maps for brass after fatigue. The maps in this figure are for brass heat treated at 400ºC for 2 hours……95

Figure 5.1. Distributions of local plastic strain in a slotted polycrystalline mesh deformed to a)

0.2%, b) 0.5%, and c)1.0% applied strain. The tensile axis was perpendicular to the length of the slot…….....……...100

Figure 5.2. Histograms of the maximum plastic strain in a slotted polycrystalline mesh deformed to 1% applied strain. Simulations were performed using both plane strain and bonded boundary conditions (see text), and with both power law and Voce hardening equations. Each value of plastic strain corresponds to a distinct simulation with a random distribution of crystallographic orientations per grain…….……100

TABLES

Table 3.1. Effect of crystal properties on pt1 singular stress state……..47

Table 3.2. Effect of crystal orientation on pt1 singular stress state……48

Table 3.3. Effect of crystal orientation on pt2 singular stress state……48

Table 3.4. Effect of crystal size on pt1 singular stress state……50

Table 3.5. Effect of grain boundary interface angle on pt1 singular stress state……...50

Table 4.1 Elastic and viscoplastic parameters……75

Table 4.2 Hardening parameters…….……75

Table 4.3 Crack nucleation predictions for different microstructure morphology…..…….....82

Table 4.4 Heat Treatment Conditions and Grain Sizes for Tailored Brass Microstructures……89

Table 4.5 Experimental Matrix for Cyclic Plasticity Experiments……94

NOMENCLATURE

EBSD	Electron Backscatter Diffraction
FIB	Focused Ion Beam
AFM	Atomic Force Microscopy
PU-FEM	Partition of Unity Finite Element Method
FEM	Finite Element Method
MPALE	Material Point Automated Lagrangian Eulerian
DOE	Department of Energy
SNL	Sandia National Laboratories

This page left intentionally blank.

1. INTRODUCTION.

The fatigue of metals is one of the core problems of structural materials for which great progress has been made and yet much remains to be done. The fatigue problem has been studied since the 1850's and yet remains one of the great limitations of structural metals. [1] Volumes of great research have been made on this topic resulting in quantitative approaches for predicting fatigue damage, crack growth, and failure for specific materials. The microscale description of the phenomena that underpin the macroscale predictions have become increasingly sophisticated [2].

Despite all of this progress, the ability to predict the nucleation of fatigue cracks and the early stages of their growth for a given microstructure is still quite nascent. Much work is being done in the literature to combine microscale simulation and experiment. Even during this program, several papers have emerged trying to connect polycrystalline plasticity simulations with experiments to investigate microscale plasticity in general [3]and fatigue in particular [4].

The thrust of this program has been to include as much sensitivity to microstructure as possible in simulation and in the experimental techniques that support it. The challenge of including microstructural physics in the simulation of cyclic damage and crack nucleation and early crack growth and sustained crack growth is larger than a single program, but this report will discuss improvements in the microstructural and computational physics touching each of these areas. Section 2 of this report will discuss new experimental methods for observing plastic deformation at the microscale which will allow for a fuller and better connection to microstructural simulations. Section 3 of this report discusses several new or improved simulation techniques for including capabilities necessary for microscale simulation of the fatigue process. Section 4 addresses the application of these experimental and simulation methods to problems of cyclic plasticity and small crack growth in metals. Section 5 introduces the concept of using probabilistic descriptions of microstructure and properties as a vehicle for transporting microscale physics into macroscale predictions.

Section 1 References:

1. Suresh, S., *Fatigue of Materials*. 2nd ed. 1998, New York: Cambridge University Press.
2. Xue, Y., et al., *Micromechanisms of multistage fatigue crack gowth in a high-strength aluminum alloy.* Acta Materialia, 2007. **55**: p. 1975-1984.
3. Heripre, E., et al., *Coupling between experimental measurements and polycrystal finite element calculations for micromechanical study of metallic materials.* International Journal of Plasticity, 2007. **23**: p. 1512-1539.
4. Dunne, F.P.E., A.J. Wilkinson, and R. Allen, *Experimental and computational studies of low cycle fatigue crack nucleation in a polycrystal.* International Journal of Plasticity, 2007. **23**: p. 273-295.

This page left intentionally blank.

2. EXPERIMENTAL METHODS FOR OBSERVING MICROSTRUCTURAL MECHANICS.

As stated in section I, a key goal of this program was to gain as much microstructural understanding about the fatigue problem as possible, both experimentally and through simulation. Recently, there have been great gains in microscale, experimental techniques necessary for studying the process of fatigue at the microstructural level. Techniques such as EBSD, micro-DIC, and synchrotron, x-ray, microdiffraction have allowed the mapping of crystallography and strain down to the microscale. This section describes specific additions to the experimental capability at Sandia as well as our efforts to quantitatively compare experimental and simulation results.

2.1. New capabilities for electron backscatter diffraction (EBSD) (L.N. Brewer (01814), B.L. Boyce (01813), D.S. Schmale (01813) and J.R. Michael (01822))

Electron backscatter diffraction (EBSD) is one of the foremost experimental techniques for measuring crystallography at the microscale. With a spatial resolution down to 10nm and a spatial range of hundreds of microns, automated EBSD can rapidly map the crystallography within an ensemble of grains. In addition, the crystallography is sensitive to plastic deformation and cracking and can be used as a tool to track these phenomena during mechanical testing. EBSD orientation maps can be used both as starting configurations and as validation data for FEM simulations of deformation phenomena.

2.1.1 In situ testing methods.

While most EBSD measurements are made on polished sections of samples that were mechanically tested *ex situ*, data for use in simulations is most efficiently collected using *in situ* experiments. *In situ* experiments allow the same area of interest to be readily tracked from one strain state to the next without removal of the sample from the microscope. In addition, the atmospheric state of the sample can more readily controlled. However, few SEM's have *in situ* straining capabilities, and the *in situ* straining stages that were commercially available were not really designed with EBSD experiments in mind.

In order to more readily perform *in situ* EBSD experiments, we designed and built a new type of straining stage, specifically designed for EBSD experiments (Figure 2.1). This straining stage has a small footprint in order to be tilted to 70° without damaging the microscope lenses or other detectors. In addition, the dual-lever design keeps the microscopic, area of interest centered during deformation because the loading is symmetric with respect to the center line of the sample. This stage is instrumented to control and measure the load and the displacement using a Wheatstone bridge transducer and a linear variable differential transformer (LVDT), respectively. A test stress-strain curve on a 304 stainless steel sample can be seen in Figure 2.1.

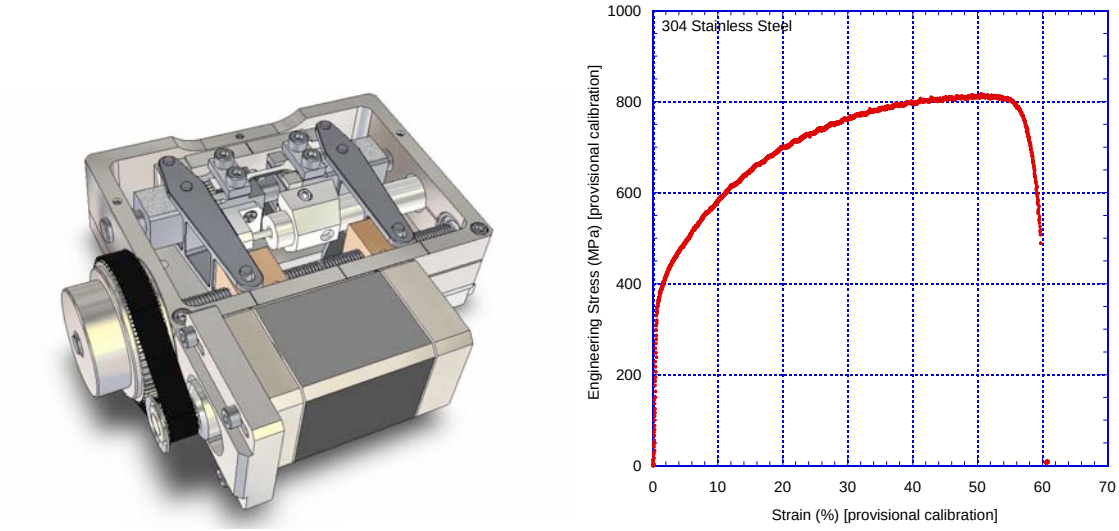

Figure 2.1 Design drawing of novel in situ straining stage for EBSD. (left) Test stress-strain curve on 304 stainless steel using the in situ stage. (right)

The *in situ* straining stage was successfully used to collect a number of data sets consisting of orientation maps of the same microstructure at multiple strain levels. (Figure 2.2). All of the experiments were monotonic and uniaxial pulls in tension. Low cycle fatigue tests would also be possible, but higher cycle fatigue tests would likely damage the *in situ* stage. As shown in Figure 2.2, we were able to easily track the same microstructural area at different strain levels. In each experiment, the strain was increased to the desired level at a nominal strain rate of 10^{-3}/s. The load at this strain level was recorded. An EBSD orientation map was then collected. The application of this new *in situ* capability will be discussed in greater detail in section 4.3 of this report.

One of the shortcomings of this approach is sample drift. Even rapid EBSD maps using the current technology at Sandia National Laboratories requires in excess of 90 minutes for a reasonably detailed map (250 by 250 points). It is possible, and has been observed, during this time that the sample can drift from its initial position. This drift is particularly problematic for in situ straining experiments as the goal is to describe the change in the microstructure due to applied to strain. If the change in observed microstructure also includes a component from drift, the data set is no longer useful.

Sample drift can be mitigated in three ways, only one of which is currently available at Sandia National Laboratories. The most basic method, and the one used for these measurements, is to simply use a protocol that waits for at least 30 minutes after loading the sample before beginning the measurement. This waiting period was combined with at least two test maps to check for drift prior to beginning a large, detailed map. In the future, these measurements could also benefit from the now commercially available fast detectors that can collect patterns between 400-700 Hz. Even at 400Hz, the mapping time would be reduced by an order of magnitude, resulting in a mapping time of approximately 10 minutes. This drastic reduction in collection time would reduce drift and would reduce the overall all time of the *in situ* experiment. Even

more recent technology now allows active drift compensation by monitoring an image of the surface of the sample and adjusting the scan area to account for sample drift.

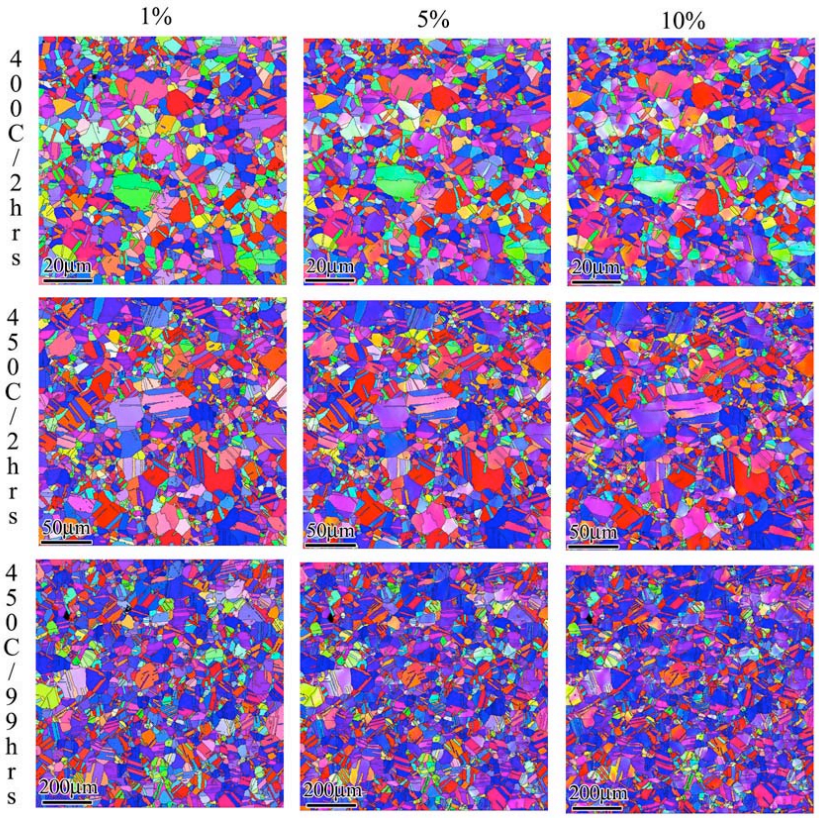

Figure 2.2 Inverse pole figure maps (with respect to x-tensile direction) for three grain sizes of brass strained to three different levels acquired using new in situ straining stage.

2.1.2. Three dimensional FIB-EBSD

Until recently, EBSD measurements have been restricted to a two dimensional sampling of a surface. In the last three years, work has begun to appear in the literature combining EBSD with focused ion beam (FIB) techniques to allow the measurement of microcrystallography in three dimensions. [1, 2] Sandia National Laboratories is now one of only a few institutions in the United States that has this three dimensional FIB-EBSD capability. This project brought this technology on line and has produced the first three dimensional microcrystallography data sets at Sandia National Laboratories.

The three dimensional experiments were performed on the new FEI Helios Nanolab instrument in the Materials Characterization Laboratory (organization 01822). This instrument is of the dual-beam type in that it has a scanning electron column on the vertical axis with a scanning gallium ion beam column at a 55 angle with respect to the vertical. This arrangement allows high resolution imaging and EBSD of an area that will be milled by the ion beam. This instrument was outfitted with the Oxford-HKL Channel 6 EBSD hardware and software system.

The experiments basically consists of ion beam-driven serial sectioning. A 30 keV gallium ion beam is used to mill a section of the sample to a flat plane. There is flexibility about the size of the milled area, but it was typically on the order of 10μm by 30μm. The size of this area (the dimension of a single slice) is restricted by the available ion beam time and sputtering problems such as redeposition. One of the unappreciated limitations of the three dimensional FIB-EBSD approach is relatively small size of volumes that can be analyzed with currently technology. In order to maintain some reasonable level of resolution in the through-thickness direction (z), it is necessary to collect many (>50 slices). For each slice, the milling can take longer than one hour followed by at least an hour for the EBSD mapping. A 50 slice measurement, could therefore easily take more than 100 hours to accomplish. As can be seen in Figure 2.3, the process is started by depositing a platinum over layer, to protect the surface of the sample, and a set of fiduciary marks in the form of an inverse pair of concentric rings. These rings allow the software to automatically reposition the area of interest if altered by drift or mechanical hysteresis. The ion beam image in Figure 4.3 shows the perspective of the ion beam milling for a given step in the process. The very edge of the sample will be milled away to a nominal depth, e.g. 50nm. After milling, the sample stage is rotated 180° to position the newly milled surface for orientation mapping using EBSD. An orientation map is then collected. The sample is then rotated back to the original position and corrected for drift or mechanical hysteresis. The next slice is then milled away by the ion beam. This process is repeated until the volume of interest has been analyzed.

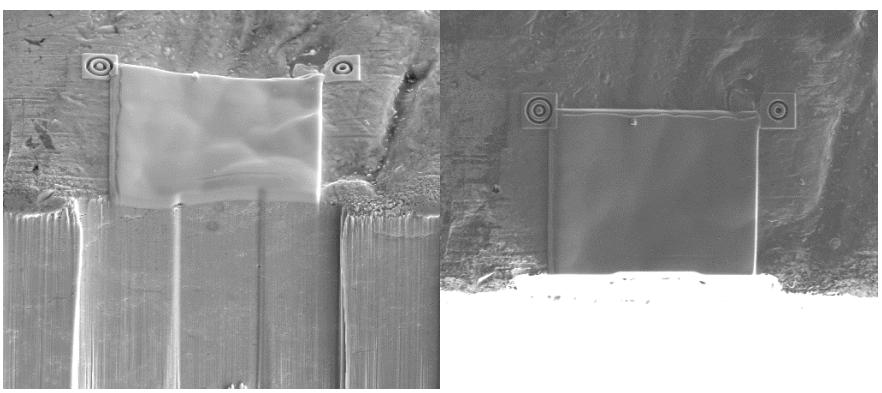

Figure 2.3 Electron image (left) and ion image (right) of sample being milled during three dimensional EBSD experiment.

The results of this process can be demonstrated with a data set from electrodeposited nickel (Figure 2.4). The value of the three dimensional measurement is immediately apparent from the extended aspect ratio of the grains. If one only mapped the x-y plane of the volume (square area in Figure 2.4), then it would be reasonable to describe the grain structure as equiaxed, albeit with possible abnormal grain growth. In addition, the cyan colored grains appear to be independent grains which are either truly small or are small because of sectioning artifacts. When the rest of the three dimensional volume is examine, it is clear that instead, the grains are quite elongated in the z-direction. The cyan-colored grains also appear to be three dimensional islands that are indeed smaller than the surrounding grains.

The three dimensional FIB-EBSD capability is only just beginning at Sandia National Laboratories. Now that we have an experimental approach which can collect data reliably, we

must now develop methods for representing and analyzing these complex data structures effectively. In fact, this analysis task is at the forefront of literature in this area. [3] As our ability to collect, digest, and utilize three dimensional data improves, we will be able to apply this approach to a number of materials problems at Sandia National Laboratories.

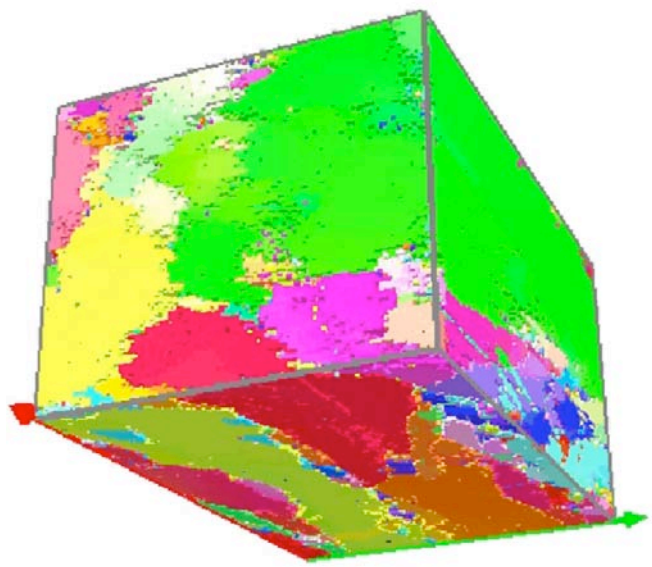

Figure 2.4. Three dimensional EBSD data set from electrodeposited nickel material.

2.2. Quantification of Agreement between Experiment and Simulation (L.N. Brewer (01814) and C.C. Battaile (01814))

As discussed, the experiments in this program were designed chiefly to be used by and compared to simulation. However, it is not clear how exactly to compare microstructural experiments with microstructural simulations. Often, the comparison in the literature is simply a qualitative description of agreement or disagreement. However, a qualitative description is not sufficient for comparing the details of the experiment and the simulation or for evaluating one plasticity model over another. The evaluation may also be too subjective if there is no quantitative figure of merit.

There are many challenges to the quantitative comparison between simulation and experiment. Foremost is the use of the correct physics for describing the plasticity or fracture. As is right, this emphasis is the one usually found in papers describing the comparison of experiment with simulation. However, there are several other important factors that make the comparison a challenge. The volumes of interest are typically not the same for experiment, e.g. EBSD, and simulation. EBSD generally works on a single two dimensional surface which is being influenced by an effectively infinite bulk lying beneath it. The simulation, e.g. FEM, generally works in a two dimensional, plane strain configuration in which the grains are extruded to infinity in the z-direction. Clearly this difference in reference volumes could cause differences in response. Additionally, there is a difference in the applied boundary conditions. The grains in the experiment experience complex, three dimensional tractions from the

neighboring grains even while the far field is some sort of simple, uniaxial tension. In many microstructural simulations, the boundaries are simple, straight-line truncations of the microstructure with simple tractions applied to these fictitious surfaces. The discrepancy in the description of boundary conditions may not be a primary factor contribution to experiment-model disagreement, but it is an important secondary factor to be considered.

For all of these challenges, there are still two important factors that have been addressed, at least in part, in this program: a difference in coordinate systems and a lack of appropriate metrics for quantitative comparison. The first is the difference in coordinate systems between an *in situ* experiment and a microstructural simulation of strain. The coordinate system during the *in situ* experiment is Eulerian. The original area of grains moves outside of the same size EBSD map after straining. The size of the EBSD map can be changed to capture the new dimensions, but it is difficult, if not impossible, to analyze exactly the same points in the microstructure. The microstructural simulation is typically performed in a Lagrangian coordinate system, i.e. the point in the grid move with the simulation. All of the same points are being analyzed at the beginning and the end of the simulation. Because of this difference in coordinate systems, work must be done to transform either the experiment or the simulation to the coordinate system of the other.

Our process for transformation the experimental and simulation data to be compared is illustrated in Figure 2.5. In this comparison, a microstructural map from EBSD was used as the starting data in the FEM simulation. After straining the sample both experimentally and in simulation, the data must be transformed. The first step is to choose a single point of reference <u>which is the same in both experiment and simulation</u>. We have used triple junctions between grains for this purpose. After choosing this reference point. The coordinate systems for both data sets are shifted such that each system has the triple junction as x,y coordinates (0,0). With the coordinate systems now shifted a reduced area for comparison must be chosen such that all of the grains to be compared are in both the experiment and the simulation. In Figure 2.5, the EBSD data is cropped; but the same can be done for simulation. At this point, the data for both EBSD and FEM represent the same set of deformed grains, but sampled at different points. The final step is to interpolate on data set onto the x,y coordinates for the other. Once this operation is complete, the data for EBSD and FEM can be compared quantitatively.

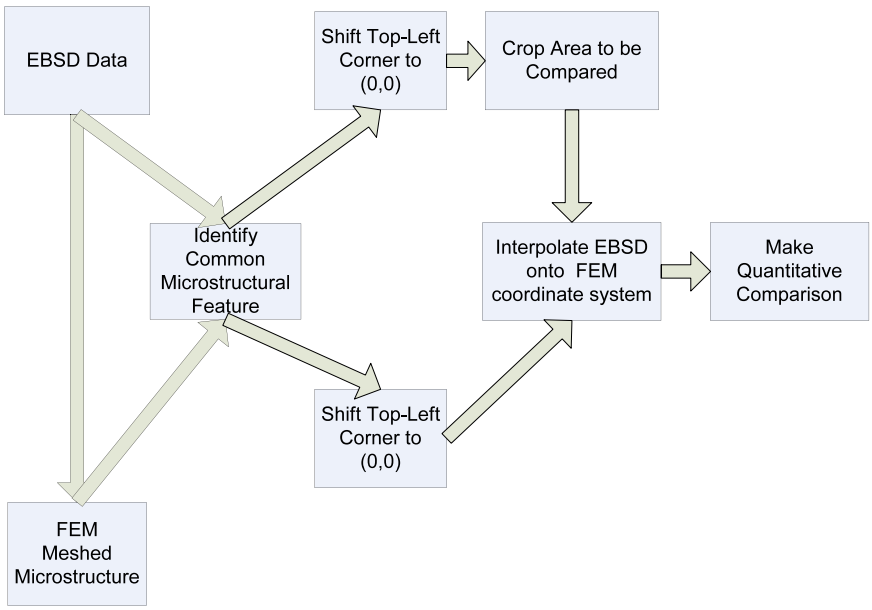

Figure 2.5. Flowchart for preparing EBSD and FEM data for quantitative comparison.

This process can be demonstrated for a microstructure of polycrystalline nickel (Figure 2.6). The top portion of the figure shows Euler color maps of orientation for FEM (left) and EBSD (right). Careful inspection of these two maps shows that they cover different numbers of grains. We chose a triple junction as the reference point for the comparison. The data sets were then shifted to make the triple junction the zero point and both were cropped to represent an area of 50µm by 50µm. As these areas still do not represent the exact, same grain areas; interpolation of the EBSD onto the FEM data results in areas for which there is no comparison (black, Figure 2.7 a). The resulting area in Figure 2.7a can now be compared directly and quantitatively with the FEM result in the bottom left of Figure 2.6. As an initial metric, the scalar, angular misorientation between all points can be plotted as demonstrated in Figure 2.7b.

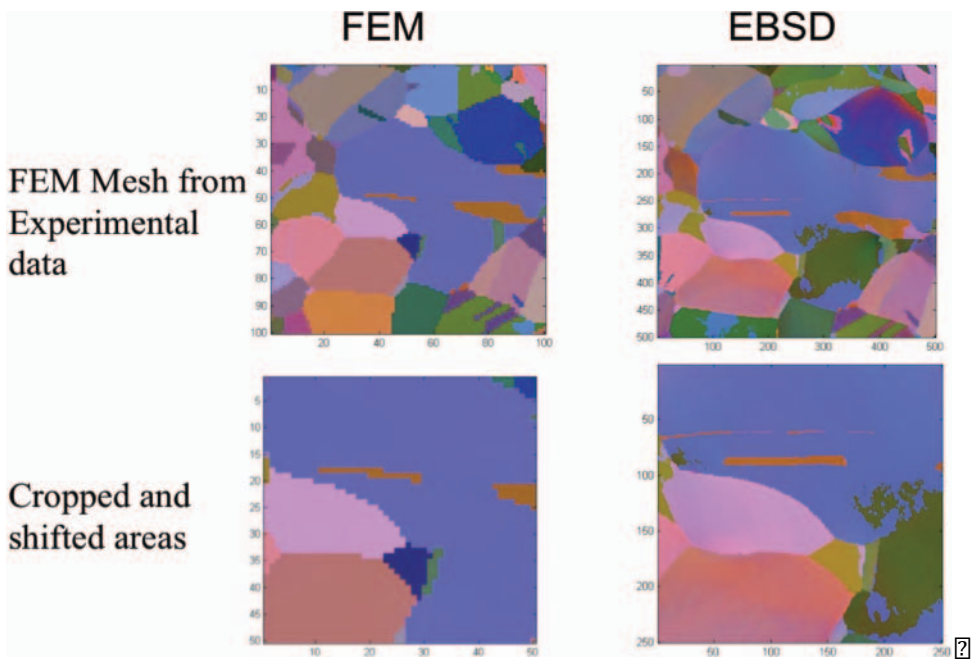

Figure 2.6. Preparation of data from nickel polycrystal for quantitative comparison between EBSD and FEM.

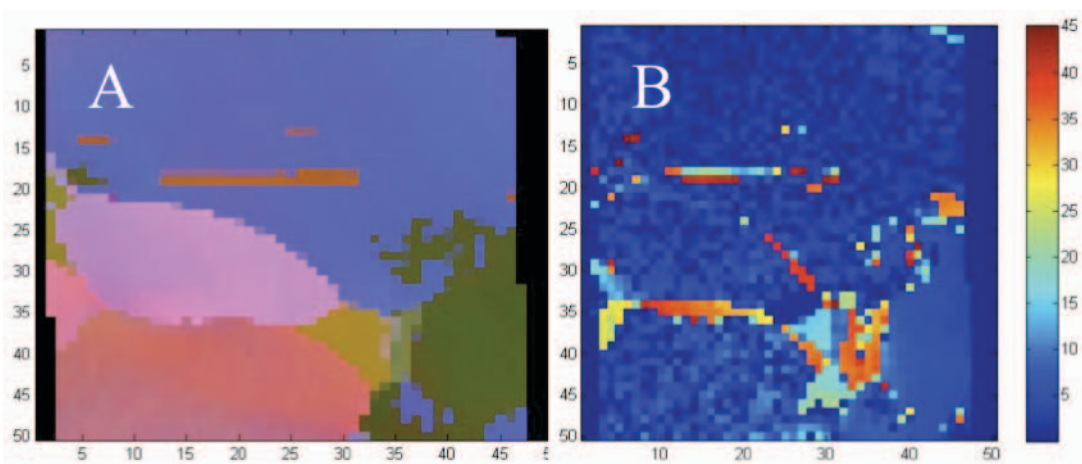

Figure 2.7. EBSD data shifted and interpolated to FEM coordinate system (A). Misorientation map created by calculating and plotting the scalar, misorientation angle for each pixel (B).

There are any number of quantitative metrics that can be used to quantitatively compare the simulation and experimental data after the appropriate transformations that have just been described. In this report, we will consider the use of scalar, angular misorientation and normalized area match fraction.

Scalar, angular misorientation is used extensively in the study of plasticity through EBSD [4]. The most basic representation of orientation through EBSD data is through the use of Euler angles (ϕ_1, Φ, ϕ_2). The orientation of a point on the x-y plane can be represented by the Euler angles through the use of an orientation matrix, G. [5]

$$G_i = \begin{pmatrix} \cos(\phi_1)\cdot\cos(\phi_2) - \sin(\phi_1)\cdot\sin(\phi_2)\cdot\cos(\Phi) & \sin(\phi_1)\cdot\cos(\phi_2) + \cos(\phi_1)\cdot\sin(\phi_2)\cdot\cos(\Phi) & \sin(\phi_2)\cdot\sin(\Phi) \\ -\cos(\phi_1)\cdot\sin(\phi_2) - \sin(\phi_1)\cdot\cos(\phi_2)\cdot\cos(\Phi) & -\sin(\phi_1)\cdot\sin(\phi_2) + \cos(\phi_1)\cdot\cos(\phi_2)\cdot\cos(\Phi) & \cos(\phi_2)\cdot\sin(\Phi) \\ \sin(\phi_1)\cdot\sin(\Phi) & -\cos(\phi_1)\cdot\sin(\Phi) & \cos(\Phi) \end{pmatrix} \quad (2.1)$$

The misorientation between any two points, 1 and 2, can also be represented by a matrix, M, which is given by

$$M = G_1^{-1} \cdot G_2 \quad (2.2)$$

The scalar, misorientation angle can then be extracted from M by

$$\theta = \cos^{-1}\left(\frac{M_{11} + M_{22} + M_{33} - 1}{2}\right) \qquad (2.3)$$

Typically, θ is used to compare points in space, such as adjacent points in an (x,y) coordinate system. However, this metric can also be used to compare the misorientation between the same (x,y) point in two different maps, i.e. EBSD and FEM. A misorientation angle of less than 0.5° is within the noise of standard EBSD measurement, and thus represents complete registry between the experiment and the simulation. A large misorientation angle represents poor registry between the experiment and the simulation.

The misorientation angle metric does show the location and the increase of disagreement between simulation and experiment as a function of strain (Figure 2.8). At 1% strain, only pixels right at grain boundaries are show large misorientation (>10°). As the strain level increases, the locations with the largest misorientation continue to be the grain boundaries. The grain boundaries appear to move more in the experiment than in the simulation. At 10% strain, the largest area of misorientation is in a grain in the lower right hand corner of the microstructure, which has a misorientation of nearly 90°. However, this large misorientation is apparently from the crystal rotation from one sector of Euler space to another. The boundaries in Euler space for a cubic symmetry system occur at 90° intervals, and thus, can create unrealistically large misorientations in the comparison maps. We are currently working on solutions to maintain the comparison in a single portion of Euler space.

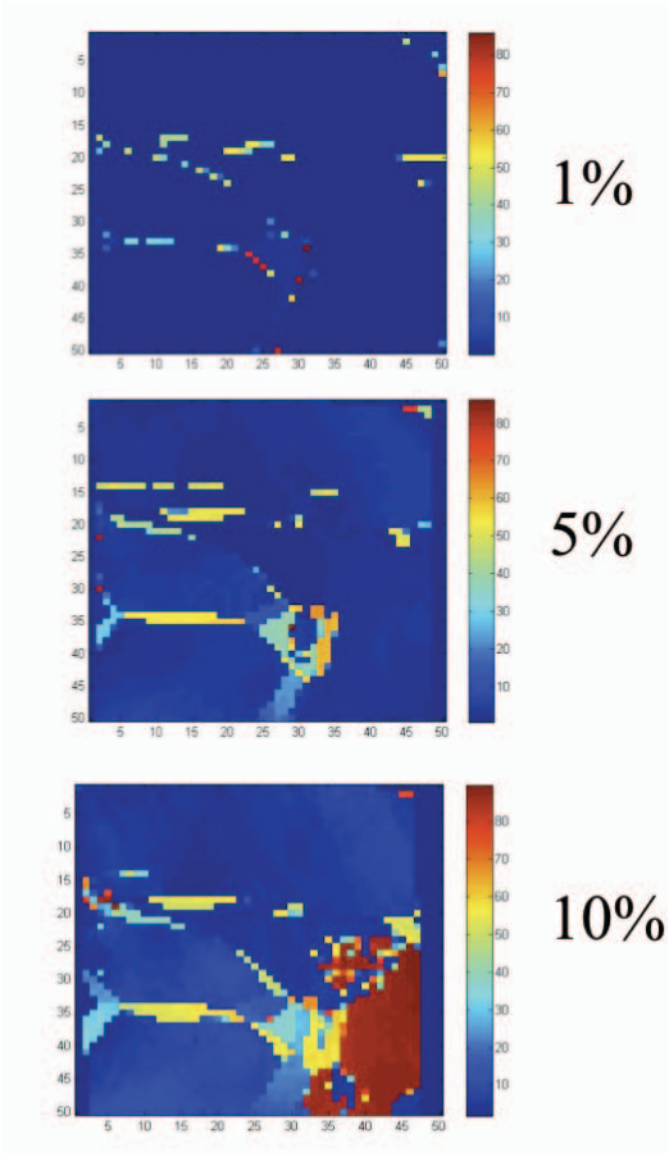

Figure 2.8. Misorientation maps comparing EBSD and FEM for increasing levels of strain.

The utility of the misorientation metric is clear when comparing local and non-local crystal plasticity models (Figure 2.9). By taking the mean value of the misorientation for maps at increasing strain levels, the amount of disagreement, in terms of misorientation, can be compared for the two types of models. In this example, the mean misorientation between experiment and simulation increases linearly for the local model; while it plateaus for the comparison between experiment and the non-local model. Actually, the local model shows better agreement at small strains than the non-local model. This kind of information is what is needed to begin to evaluate the accuracy of particular microstructural plasticity models.

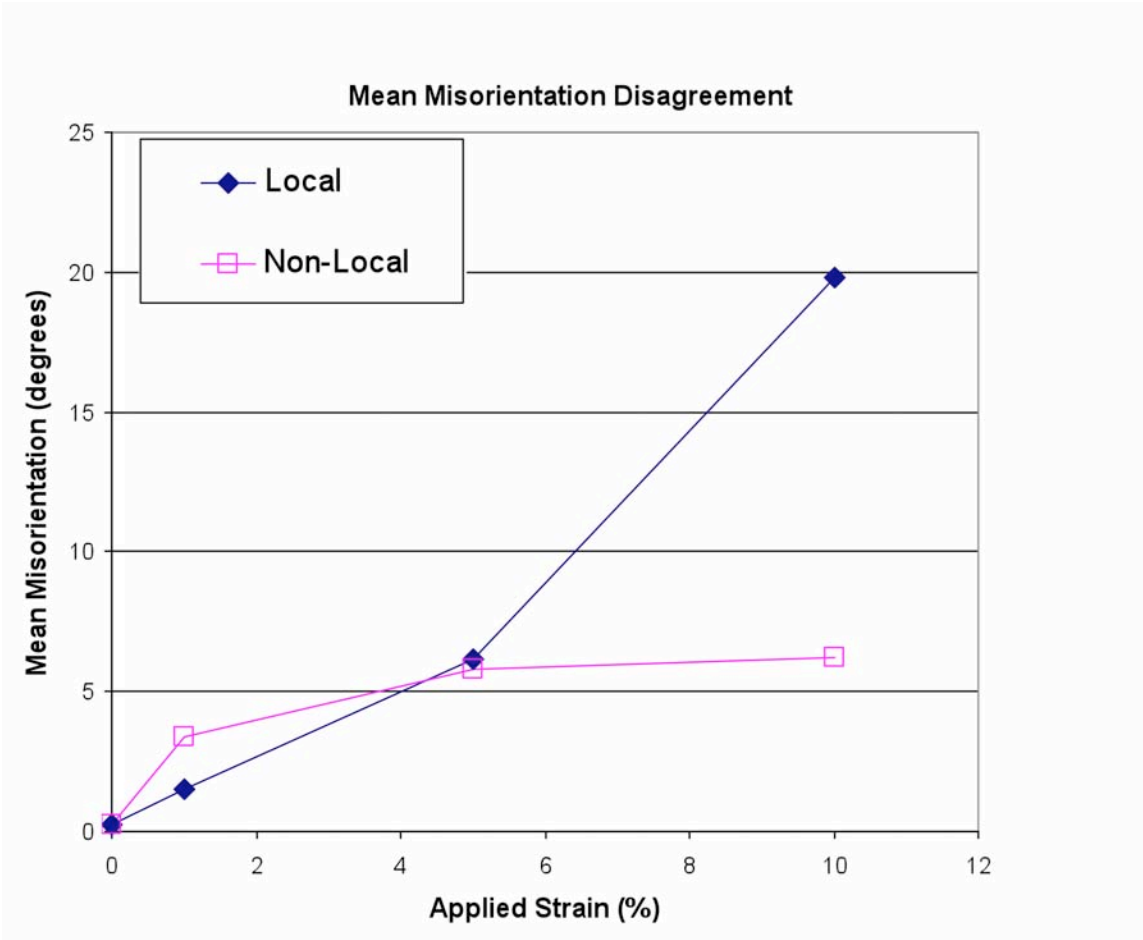

Figure 2.9. Mean misorientation between EBSD and FEM for local and non-local crystal plasticity models.

Another possibility for a comparison metric is the normalized area match fraction (NAMF). This quantity was first derived and applied to the comparison and experiments and simulations by Demirel [6]for the study of grain growth in aluminum. The NAMF is basically the percentage of pixels that have perfect agreement between experiment and simulation. The formulation in Demirel's work is too rigid for plasticity as two pixels must have exactly the same orientation to be counted as being in agreement. In equation 2.4, we suggest amending the formulation for NAMF to include an angular misorientation threshold. If the threshold is exceeded then the pixel is not counted as being in agreement.

$$NAMF = \frac{1}{Z} \sum_{x,y} \begin{cases} 1 \text{ if } \theta < threshold \\ 0 \text{ if } \theta \geq threshold \end{cases} \quad (2.4)$$

The plot of NAMF versus the strain level (Figure 2.10) gives a similar picture for the comparison of the local and non-local models as the mean misorientation (Figure 2.9); but with some added richness. Again, the local model has better agreement (larger NAMF) than the non-local (NL) model at small strain levels, but the local model agreement rapidly descends towards zero as the

strain increases. The non-local model NAMF decreases as soon as the strain begins to build, but it decays to a relatively stable value. As would be expected, the NAMF for the non-local model with the larger threshold is systematically larger than for the smaller threshold at all strain levels. Surprisingly, the NAMF at the two levels for the local model is the same at 1% and 10% strain.

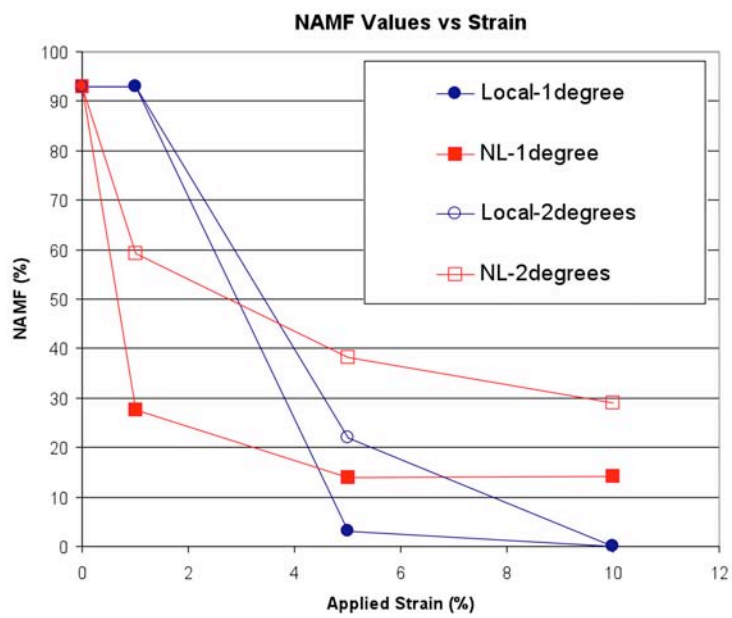

Figure 2.10. Normalized area match fraction plots comparing EBSD and FEM data using local and non-local crystal plasticity models.

Section 2 References:

1. Zaafarani, N., et al., *Three-dimensional investigation of the texture and microstructure below a nanoindent in a Cu single crystal using 3D EBSD and crystal plasticity finite element simulations.* Acta Materialia, 2006. **54**: p. 1863-1876.
2. Konrad, J., S. Zaefferer, and D. Raabe, *Investigation of orientation gradients around a hard Laves particle in a warm-rolled Fe3Al-based alloy using a 3D EBSD-FIB technique.* Acta Materialia, 2006. **54**: p. 1369-1380.
3. Lee, S.B., A.D. Rollett, and G.S. Rohrer, *Three-dimensional microstructure reconstruction using FIB-OIM.* Materials Science Forum, 2007. **558-559**(1&2): p. 915-920.
4. Brewer, L.N., D.P. Field, and C.C. Merriman, *Mapping and Assessing Plastic Deformation Using EBSD*, in *Electron Backscatter Diffraction in Materials Science*, A.J. Schwartz, et al., Editors. 2009, Springer: New York. p. 251-258.
5. Randle, V. and O. Engler, *Introduction to Texture Analysis: Macrotexture, Microtexture, and Orientation Mapping*. 2000, Amersterdam: Gordon and Breach Science Publishers.
6. Demirel, M.C., et al., *Bridging Simulations and Experiments in Microstructure Evolution.* Physical Review Letters, 2003. **90**(1): p. 016106-1-016106-4.

This page left intentionally blank.

This page left intentionally blank.

3. SIMULATION METHODS FOR PREDICTING MICROSTRUCTURAL PLASTICITY AND CRACK BEHAVIOR.

3.1. Material Point Method in elasto-plastic deformation at finite strains: Crystal plasticity capabilities in MPALE. (R.P.M. Dingreville (01814), T.J. Bartel (06774), and C.C. Battaile (01814))

3.1.1. Introduction

A crystal plasticity model was implemented for use in Sandia's material point method code (MPALE). Tests problems were performed on single crystals and polycrystals to directly compare the explicit MPM solutions with an implicit Sandia's Finite Element (FE) code (JAS3D) as a validation of the implementation. Results demonstrated the differences and concordances between the two methods. Stemming from Particle-in-Cell (PIC) methods and hydrodynamics codes (FLIP) [1-3], the material-point method (MPM) has been successfully applied to solid mechanics problems [4-7]. In this framework, the continuum is represented by a distribution of material points having a definite mass. The material-point method can be regarded as a spatial discretization method formulated in an arbitrary Lagrangian-Eulerian description of motion. MPM employs two discretizations to solve the constitutive equations and equations of motion of fluids and solids. A Lagrangian description of the material discretizes the continuum into a finite collection of unconnected material points with an assigned mass and density consistent with the material density and volume of that point. All states variables and constitutive equations are tracked at the set of material points while the equations of motion and interactions among the materials points are formulated and solved by using a background computational grid. A mapping between the two discretizations is performed at each step of the evolution of the system by means of shape functions. Since the computational grid can be defined in any arbitrary manner, mesh distortion problems are avoided.

Few studies have used MPM to investigate elasto-plastic deformation at finite deformation. In fact, most of them use a J^2 flow model of plasticity [8, 9] on the classical Taylor bar problem

In this section, we first introduce the governing equations and basic features of the material point approach. Then example solutions are given in the framework of local crystal plasticity and compared with Finite Element Method solutions to show that the MPM approach provides satisfying numerical results.

The procedure shows considerable promise applications to problems combining microstructural evolution and thermo-mechanical solicitations. The use of material points provides the basis to couple the mesoscale and macroscale models by defining both materials information at the microstructural level and thermo-mechanical information at the continuum level at the same computational particle. The incorporation of compositional and microstructural evolution based on kinetic Monte Carlo would be natural due to its canonical description of discrete ensemble.

3.1.2 Material Point Method

Let **x** denote the position of a material point in the deformed state at time *t*. This material point is defined by its initial position **X** in the undeformed state at time *t*=0 and it is considered to be a function of both **X** and *t*, with the initial condition being,

$$\mathbf{x} = \mathbf{x}(\mathbf{X}, t = 0) = \mathbf{X} \quad (3.1).$$

If the displacement vector **u** is defined by,

$$\mathbf{u} = \mathbf{x} - \mathbf{X} \quad , \tag{3.2}$$

then the velocity **v**, and the acceleration **a** vectors of that material point are defined by,

$$\begin{aligned} \mathbf{v} &= \frac{d\mathbf{x}(\mathbf{X},t)}{dt} = \dot{\mathbf{x}} = \frac{d\mathbf{u}(\mathbf{X},t)}{dt} = \dot{\mathbf{u}} \\ \mathbf{a} &= \frac{d^2\mathbf{x}(\mathbf{X},t)}{dt^2} = \ddot{\mathbf{x}} = \frac{d^2\mathbf{u}(\mathbf{X},t)}{dt^2} = \ddot{\mathbf{u}} = \frac{d\mathbf{v}(\mathbf{X},t)}{dt} = \dot{\mathbf{v}} \end{aligned} \quad . \tag{3.3}$$

Given that **x** and **X** define two spatial positions; the deformation gradient and its time derivative can be described with respect to both coordinate system. In the Lagrangian framework (i.e. with respect to the undeformed state **X**), the deformation gradient and its time derivative can be defined as,

$$\mathbf{F} = \mathbf{x}\nabla_0 \quad , \quad \dot{\mathbf{F}} = \mathbf{v}\nabla_0 \quad . \tag{3.4}$$

Assuming that the Jacobean determinant $J = \det(\mathbf{F})$ is non singular (i.e $J > 0$), the correspondence of the gradient operator between the Lagrangian and the Eulerian (i.e. with respect to the deformed configuration **x**) framework arises from the chain rule such that,

$$(\ )\nabla_0 = (\ )\nabla \cdot \mathbf{F} \quad , \quad (\ )\nabla = (\ )\nabla_0 \cdot \mathbf{F}^{-1} \quad . \tag{3.5}$$

This correspondence being defined, it follows that the spatial gradient velocity **L** is given by,

$$\mathbf{L} = (\mathbf{v})\nabla = (\mathbf{v})\nabla_0 \cdot \mathbf{F}^{-1} = \dot{\mathbf{F}} \cdot \mathbf{F}^{-1} = \mathbf{D} + \mathbf{W} \quad , \tag{3.6}$$

where **D** is the rate of deformation and the symmetric part of **L**, and **W** is the vorticity and the skew-symmetric part of **L**.

For a continuum under purely mechanical loading, the above kinematic relations are supplemented by the governing differential equations of motion derived from the conservation equation of momentum,

$$\rho\mathbf{a} = (\sigma)\nabla + \rho\mathbf{b} \quad , \tag{3.7}$$

where $\rho(\mathbf{x},t)$ is the mass density, $\sigma(\mathbf{x},t)$ is the Cauchy stress tensor and $\mathbf{b}(\mathbf{x},t)$ denotes the body force per unit mass. These governing equations are complemented by the conservation equation for mass,

$$\frac{d\rho}{dt} + \rho(\mathbf{v})\nabla = 0 \tag{3.8}$$

and a suitable constitutive equation (see Appendix). Note that in a Lagrangian framework, equation (3.8) is automatically satisfied.

The traction boundary conditions are such that if **n** denotes the outer normal to a surface, the traction **t** is given by,

$$\mathbf{t} = \sigma \cdot \mathbf{n} \tag{3.9}$$

For a given set of traction and displacement boundary conditions, the governing equations (3.1) – (3.9) are numerically solved using the MPM framework.

As already briefly stated in the introduction, MPM employs two discretizations to solve the constitutive equations and equations of motion of fluids and solids throughout the deformation process. At any given time *t*, a Lagrangian description of the material discretizes the continuum into a finite collection of $K > 0$ unconnected material points $\mathbf{x}_p^t$ with an assigned mass M_p (p=1...K) and density ρ_p^t consistent with the material density and volume of that point. Variables such as the velocity $\mathbf{v}_p^t$, the Cauchy stress tensor σ_p^t, the Green-Lagrange strain tensor $\mathbf{E}_p^{e,t}$, and any other internal state variables associated with a material point *p* can be tracked through the complete deformation history of the system. At any given time step *t*, the information associated with the material points is mapped to a background computational grid constituted of $N > 0$ nodes. This grid covers the region of interest and can be chosen arbitrarily preventing any associated problem with mesh distortion. Illustrated in Figure 3.5 is the space discretization of the computational domain of interest. The discrete formulation of equations (3.7 –3.9) allows for the momentum equation to be solved at the mesh nodes whereas the constitutive equations are evaluated at the material points.

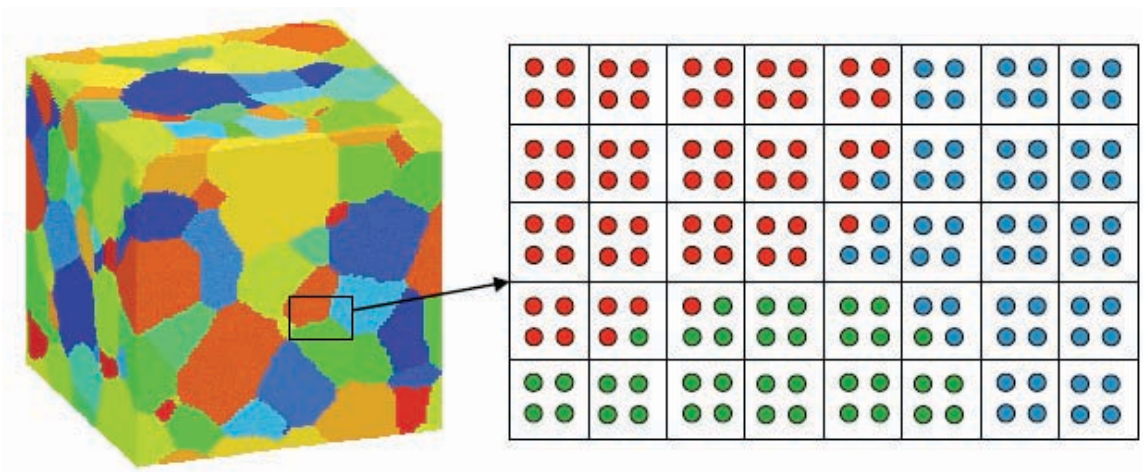

Figure 3.5. Space discretization composed of material points and computational grid.

Similarly to classical Finite Element Method (FEM), the weak form of the equation of virtual work [4, 6] can be expressed as,

$$\int_{\Omega} \rho \left(\mathbf{a} \cdot \mathbf{w} + \frac{1}{\rho} \sigma : (\mathbf{w}) \nabla \right) d\Omega = \int_{\Omega} \rho \mathbf{b} \cdot \mathbf{w} d\Omega + \int_{\partial\Omega^{\sigma}} \mathbf{t} \cdot \mathbf{w} dS + \int_{\partial\Omega^{u}} \sigma \cdot \mathbf{n} \cdot \mathbf{w} dS \quad , \forall \mathbf{w} \in W_0 \quad ,(3.10)$$

where Ω is the current region occupied by the continuum, $\partial\Omega^{\sigma}$ is the part of boundary where traction is prescribed, $\partial\Omega^{u}$ is the part of the boundary where displacements are prescribed and $\mathbf{w}$ denotes a virtual displacement function. $W_0 = \left\{ \mathbf{w} / \mathbf{w} = 0 \text{ on } \partial\Omega^{u} \right\}$ denotes the space of admissible accepted displacement fields satisfying the homogeneous boundary conditions. The initial boundary conditions completing the formulation are given by

$$\mathbf{w}(0) = \mathbf{w}^0 \quad , \quad \dot{\mathbf{w}}(0) = \mathbf{v}^0 \quad , \quad \sigma(0) = \sigma^0 \quad , \qquad (3.11)$$

where $\mathbf{w}^0$, $\mathbf{v}^0$ and σ^0 are the initial fields of displacements, velocities and stresses respectively.

The two space discretizations aforementioned allows for the continuum Ω to be divided into a finite number (*K*) of subregions represented by the material points $\mathbf{x}_p^t$, $p = 1 \ldots K$. The whole mass of a specific region is concentrated at the corresponding material points, so that the total mass density field can be written such that,

$$\rho(\mathbf{x},t) = \sum_{p=1}^{K} M_p \delta\left(\mathbf{x} - \mathbf{x}_p^t\right) \quad , \tag{3.12}$$

where $\delta(\mathbf{x})$ is the Dirac function. Substituting equation (3.12) into the equation of virtual work (3.10) converts the integral form to a discrete summation form evaluated at the material point such that the equation **Error! Reference source not found.** becomes,

$$\begin{aligned} &\sum_{p=1}^{K} M_p \left[\mathbf{a}\left(\mathbf{x}_p^t\right) \cdot \mathbf{w}\left(\mathbf{x}_p^t\right) + \sigma^{\rho}\left(\mathbf{x}_p^t\right) : (\mathbf{w}) \nabla \big|_{\mathbf{x}_p^t} \right] \\ &= \sum_{p=1}^{K} M_p \mathbf{b}\left(\mathbf{x}_p^t\right) \cdot \mathbf{w}\left(\mathbf{x}_p^t\right) + \int_{\partial\Omega^{\sigma}} \mathbf{t} \cdot \mathbf{w} dS + \int_{\partial\Omega^{u}} \sigma \cdot \mathbf{n} \cdot \mathbf{w} dS \end{aligned} \quad , \tag{3.13}$$

where $\sigma_{ij}^{\rho} = \sigma_{ij} / \rho$ is defined as the specific stress.

In order to approximate the different fields and gradient terms of equation (3.13), conventional MPM formulation uses a regular grid mesh with equally spaced nodes. This grid is constructed of 2-node cells for one-dimensional problems, 4-node cells for two-dimensional problems, and 8-node cells for three-dimensional problems. Mapping between the material points and grid points discretizations is performed at each step of the evolution of the system by means of nodal decomposition using standard finite element shape functions such as,

$$\phi(\mathbf{x}) = \sum_{i=1}^{N} \phi_i N_i(\mathbf{x}) \quad , \tag{3.14}$$

where subscript *i* refers here to the nodal value of $\phi(\mathbf{x})$.
For instance, the shape functions for 2-node cell in one-dimensional problems are,

$$\begin{cases} N_1 = 1 - \xi \\ N_2 = \xi \end{cases} \quad , \tag{3.15}$$

where ξ is the natural coordinate of a material point in the cell along the X direction. The shape functions for a 4-node cell in two-dimensional problems are,

$$\begin{cases} N_1 = (1-\xi)(1-\eta) \\ N_2 = \xi(1-\eta) \\ N_3 = (1-\xi)\eta \\ N_4 = \xi\eta \end{cases} \quad , \tag{3.16}$$

where ξ and η are the natural coordinates of a material point in the cell along the X and Y directions respectively.
Finally the shape function for a 8-node cell in three-dimensional problems are,

$$\begin{cases} N_1 = (1-\xi)(1-\eta)(1-\theta) \\ N_2 = \xi(1-\eta)(1-\theta) \\ N_3 = (1-\xi)\eta(1-\theta) \\ N_4 = (1-\xi)(1-\eta)\theta \\ N_5 = \xi\eta(1-\theta) \\ N_6 = \xi(1-\eta)\theta \\ N_7 = (1-\xi)\eta\theta \\ N_8 = \xi\eta\theta \end{cases} , \tag{3.17}$$

where ξ, η and θ are the natural coordinates of a material point in the cell along the X, Y and Z directions respectively. The coordinates $\mathbf{x}_p^t$ of any given material point in a cell are therefore mapped such that,

$$\mathbf{x}_p^t = \sum_{i=1}^{N} \mathbf{x}_i^t N_i\left(\mathbf{x}_p^t\right) \quad , \tag{3.18}$$

where $\mathbf{x}_i^t$ are the coordinates associated with node *I* at time *t*.

Similarly the displacements $\mathbf{u}_p^t$ of any given material point in a cell are defined by the nodal displacements $\mathbf{u}_i^t$ such that,

$$\mathbf{u}_p^t = \sum_{i=1}^{N} \mathbf{u}_i^t N_i\left(\mathbf{x}_p^t\right) \quad . \tag{3.19}$$

As a consequence of having the same nodal basis functions for both spatial coordinates and displacement decomposition, kinematic compatibility requires that the velocity $\mathbf{v}_p^t$ and acceleration $\mathbf{a}_p^t$ of any given material point in a cell are represented by,

$$\mathbf{v}_p^t = \sum_{i=1}^{N} \mathbf{v}_i^t N_i\left(\mathbf{x}_p^t\right) \text{ and } \mathbf{a}_p^t = \sum_{i=1}^{N} \mathbf{a}_i^t N_i\left(\mathbf{x}_p^t\right) \quad , \tag{3.20}$$

,where $\mathbf{v}_i^t$ and $\mathbf{a}_i^t$ are the nodal velocities and nodal accelerations respectively.

The framework of equations (3.18 -3.20) ensures that any associated vectors are continuous across the cell boundary. Nevertheless, the use of linear shape function does not necessarily guarantee that the gradients of these vectors are continuous across the cell boundary.

Following equations (3.4 -3.6) and combined with equations (3.18 –3.20), the spatial gradient velocity $\mathbf{L}_p^t$ and deformation gradient $\mathbf{F}_p^t$ of any given material point in a cell is given by,

$$\mathbf{L}_p^t = \sum_{i=1}^{N} \mathbf{v}_i^t G_i\left(\mathbf{x}_p^t\right) \quad , \tag{3.21}$$

$$\mathbf{F}_p^t = \sum_{i=1}^{N} \mathbf{x}_i^t G_i^0\left(\mathbf{x}_p^t\right) \quad , \tag{3.22}$$

with $G_i\left(\mathbf{x}_p^t\right) = \nabla N_i\big|_{\mathbf{x}_p^t}$ representing the gradient of each basis function at the current locations of the material points at time *t*, while $G_i^0\left(\mathbf{x}_p^t\right) = \nabla_0 N_i\big|_{\mathbf{X}_p^t}$ represents the gradient operator of each basis function with respect to the undeformed configuration.

Substituting equations (3.18 –3.20) into equation (3.13) yields,

$$\sum_{i=1}^{N} \mathbf{w}_i^t \cdot \left(\sum_{p=1}^{K} m_{ij}^t \mathbf{a}_j^t + \sum_{p=1}^{K} M_p \sigma_p^{\rho,t} \cdot \nabla N_i \big|_{\mathbf{x}_p^t} \right) = \sum_{i=1}^{N} \mathbf{w}_i^t \cdot \mathbf{b}_i^t + \sum_{i=1}^{N} \mathbf{w}_i^t \cdot \hat{\mathbf{t}}_i^t + \sum_{i=1}^{N} \mathbf{w}_i^t \cdot \hat{\mathbf{f}}_i^t \quad , \quad (3.23)$$

where m_{ij}^t is the mass matrix depending on the position of the material points with respect to the computational grid at time *t* such that,

$$m_{ij}^t = \sum_{p=1}^{K} M_p N_i \left(\mathbf{x}_p^t\right) N_j \left(\mathbf{x}_p^t\right) \quad , \quad (3.24)$$

$\sigma_p^{\rho,t} = \sigma^{\rho,t}\left(\mathbf{x}_p^t\right)$ is the specific stress tensor associated with the material point $\mathbf{x}_p^t$ at time *t*, $\mathbf{b}_i^t$ is the vector of nodal specific body force field at time *t* discretized such that,

$$\mathbf{b}_i^t = \sum_{p=1}^{K} M_p \mathbf{b}\left(\mathbf{x}_p^t\right) N_i \left(\mathbf{x}_p^t\right) \quad , \quad (3.25)$$

$\hat{\mathbf{t}}_i^t$ is the vector of nodal surface traction at time *t* defined by,

$$\hat{\mathbf{t}}_i^t = \int_{\partial\Omega^\sigma} N_i \mathbf{t} dS \quad , \quad (3.26)$$

and $\hat{\mathbf{f}}_i^t$ is vector of nodal the contact forces at time *t* given by,

$$\hat{\mathbf{f}}_i^t = \int_{\partial\Omega^u} \sigma \cdot \mathbf{n} N_i dS \quad . \quad (3.27)$$

Since the vector $\mathbf{w}_i$ is arbitrary except where the degrees of freedom are prescribed at the nodes belonging to $\partial\Omega^u$, the equation of motion (3.23) can be schematically summarized by,

$$\sum_{j=1}^{N} m_{ij}^t \mathbf{a}_j^t = \mathbf{f}_i^{\text{int,t}} + \mathbf{f}_i^{ext,t} \quad , \quad (3.28)$$

where the nodal internal force vector $\mathbf{f}_t^{\text{int},t}$ at time *t* is given by,

$$\mathbf{f}_i^{\text{int},t} = -\sum_{p=1}^{K} M_p \sigma_p^{\rho,t} \cdot G_i \left(\mathbf{x}_p^t\right) \quad , \quad (3.29)$$

with $G_i\left(\mathbf{x}_p^t\right) = \nabla N_i \big|_{\mathbf{x}_p^t}$ representing the gradient of each basis function at the current locations of the material points at time *t*. The nodal external force vector $\mathbf{f}_i^{ext,t}$ at time *t* is given by,

$$\mathbf{f}_i^{ext,t} = \mathbf{b}_i^t + \hat{\mathbf{t}}_i^t + \hat{\mathbf{f}}_i^t \quad . \quad (3.30)$$

3.1.3 Microstructure-based model

To understand and study non-linear elasto-visco-plastic behavior at the microstructural level, the material deformation is treated with a standard crystal plasticity rate-dependent formulation presented in the Appendix.

Suppose the complete state of the continuum is known at time *t*. The algorithm consists of the following steps (see Figure 3.2):

(a) For each particle, one first needs to perform the mapping operations (mass, momentum, and internal forces) from the particle points to the grid nodes. These procedure includes:

The mapping of the mass from the particles to the grid nodes containing these particles,

$$m_i^t = \sum_{p=1}^{K} M_p N_i\left(\mathbf{x}_p^t\right) \quad , \tag{3.31}$$

where m_i^t is the mass at node *i* at time *t*.

The mapping of the momentum equation from the particles to the grid nodes containing these particles,

$$\left(m\mathbf{v}\right)_i^t = \sum_{p=1}^{K} \left(M\mathbf{v}\right)_p^t N_i\left(\mathbf{x}_p^t\right) \quad , \tag{3.32}$$

where $\left(m\mathbf{v}\right)_i^t$ is the nodal momentum at node *i* at time *t*, and $\left(M\mathbf{v}\right)_p$ the momentum of particle *p* at time *t*.

Once these two mapping operations are done, the internal force vector $\mathbf{f}_i^{\text{int},t}$ is obtained at the grid nodes using equation (3.29),

$$\mathbf{f}_i^{\text{int},t} = -\sum_{p=1}^{K} G_i\left(\mathbf{x}_p^t\right) \cdot \sigma_p^t \frac{M_p}{\rho_p^t} \quad , \tag{3.33}$$

(b) The internal force vector is subsequently used to apply boundary conditions to the grid nodes and calculate the nodal force vector $\mathbf{f}_i^t$,

$$\mathbf{f}_i^t = \mathbf{f}_i^{\text{int},t} + \mathbf{f}_i^{ext,t} \quad , \tag{3.34}$$

where $\mathbf{f}_i^{ext,t}$ denotes the external nodal force vector given by equation (3.30).

(c) The nodal force vector is then use to update the momentum at the grid nodes at time $t + \Delta t$,

$$\left(m\mathbf{v}\right)_i^{t+\Delta t} = \left(m\mathbf{v}\right)_i^t + \mathbf{f}_i^t \Delta t \quad . \tag{3.35}$$

(d) Knowing the nodal force vector and nodal momentum, once can, for each particle, perform mapping operations (acceleration, velocity, displacement position) from the nodes of the cell containing the particle to the particle. These operations include:

The mapping of the nodal accelerations back to the particle,

$$\mathbf{a}_p^t = \sum_{i=1}^{N} N_i\left(\mathbf{x}_p^t\right) \frac{\mathbf{f}_i^t}{m_i^t} \quad . \tag{3.36}$$

The mapping of the updated nodal velocity back to the particle by means of the shape functions,

$$\bar{\mathbf{v}}_p^{t+\Delta t} = \sum_{i=1}^{N} N_i\left(\mathbf{x}_p^t\right) \frac{\left(m\mathbf{v}\right)_i^{t+\Delta t}}{m_i^t} \quad , \tag{3.37}$$

or alternatively, compute the updated particle velocity by using a explicit time integration scheme such that,

$$\mathbf{v}_p^{t+\Delta t} = \mathbf{v}_p^t + \mathbf{a}_p^t \Delta t \quad . \tag{3.38}$$

Note that equation (3.38), while equation(3.37) leads to higher numerical dissipation (if quasistatic this is not an issue).

The updated particle position is obtained by a backward integration using the nodal functions to ensure a continuous velocity field inside the cell and to limit numerical errors,

$$\mathbf{x}_p^{t+\Delta t} = \mathbf{x}_p^t + \bar{\mathbf{v}}_p^{t+\Delta t} \Delta t \quad . \tag{3.39}$$

The particle displacement is given by,

$$\mathbf{u}_p^{t+\Delta t} = \mathbf{x}_p^{t+\Delta t} - \mathbf{x}_p^0 \quad . \tag{3.40}$$

(e) Once the spatial information has been updated on the particles, once can update the momentum back to the grid nodes containing these particles

$$\left(m\mathbf{v}\right)_i^{t+\Delta t} = \sum_{p=1}^{K} \left(M\mathbf{v}\right)_p^{t+\Delta t} N_i\left(\mathbf{x}_p^t\right) \quad . \tag{3.41}$$

(f) The updated nodal momentum helps finding the updated nodal velocities

$$\mathbf{v}_i^{t+\Delta t} = \frac{\left(m\mathbf{v}\right)_i^{t+\Delta t}}{m_i^t} \quad . \tag{3.42}$$

(g) In the case of the deformation gradient formulation used in crystal plasticity, the current particle velocity gradient can be calculated using the gradient of each basis function at the current locations of the material points such that,

$$\mathbf{L}_p^{t+\Delta t} = \sum_{i=1}^{N} \mathbf{v}_i^{t+\Delta t} G_i\left(\mathbf{x}_p^t\right) \quad . \tag{3.43}$$

(h) Following equation (3.5), one can calculate the updated deformation gradient of a material point,

$$\mathbf{F}_p^{t+\Delta t} = \sum_{i=1}^{N} \mathbf{x}_i^{t+\Delta t} G_i\left(\mathbf{x}_p^t\right) \cdot \mathbf{F}_p^t \quad , \tag{3.44}$$

or combining equation (3.44) with the explicit time integration of the nodal positions, this gives for a Lagrangian framework,

$$\mathbf{F}_p^{t+\Delta t} = \sum_{i=1}^{N} \left(\mathbf{x}_i^t + \mathbf{v}_i^{t+\Delta t}\Delta t\right) G_i\left(\mathbf{x}_p^t\right) \cdot \mathbf{F}_p^t = \sum_{i=1}^{N} \mathbf{x}_i^t G_i\left(\mathbf{x}_p^t\right) \cdot \mathbf{F}_p^t + \sum_{i=1}^{N} \mathbf{v}_i^{t+\Delta t} \Delta t G_i\left(\mathbf{x}_p^t\right) \cdot \mathbf{F}_p^t \quad . \tag{3.45}$$

(i) The stress increment is found from the local crystal plasticity constitutive model for a given deformation gradient increment $\Delta\mathbf{F}_p^{t+\Delta t} = \mathbf{F}_p^{t+\Delta t} - \mathbf{F}_p^t$,

$$\sigma_p^{t+\Delta t} = \sigma_p^t + \Delta\sigma \quad . \tag{3.46}$$

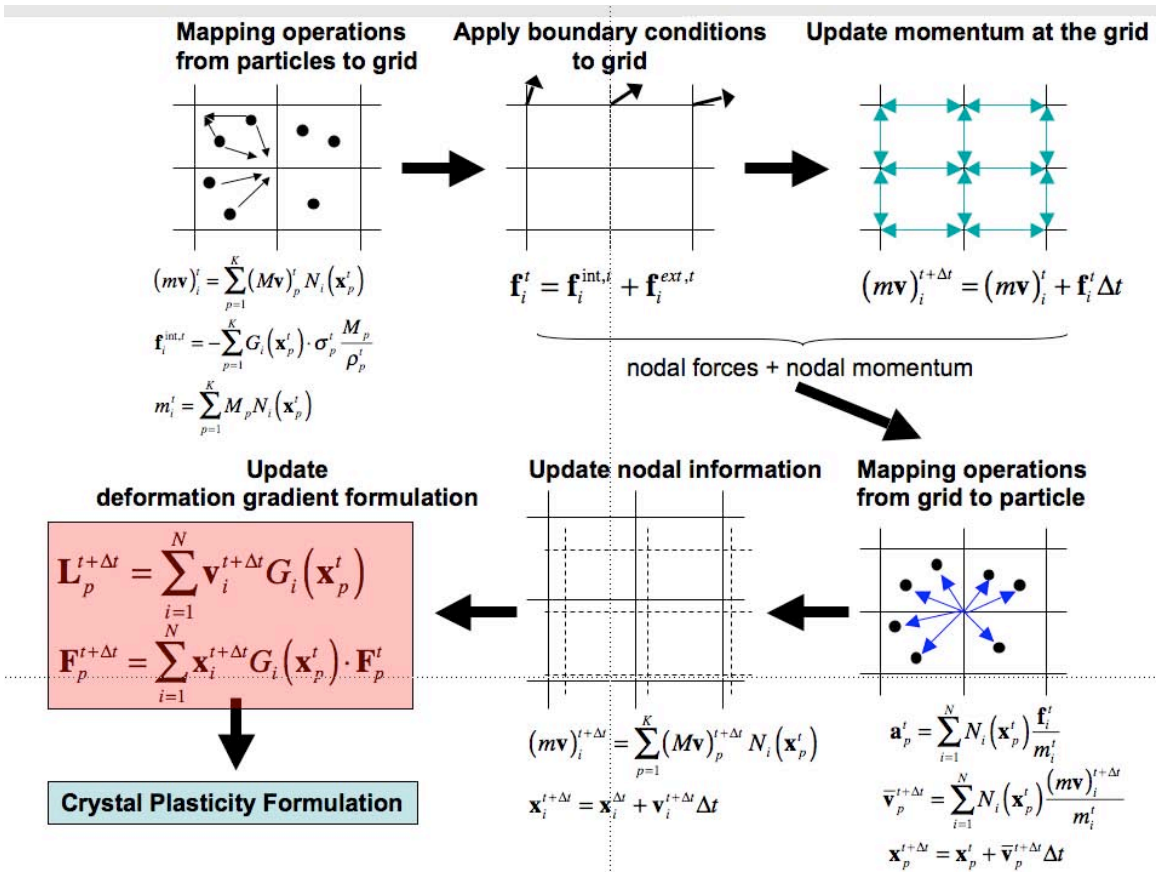

Figure 3.6. Implementation of crystal plasticity in MPALE.

3.1.4 Numerical Examples for Crystal Plasticity

As a validation of the implementation of the crystal plasticity framework into tests problems were performed on single crystals and polycrystals to directly compare the MPM solutions with Sandia's Finite Element (FE) code (JAS3D). The crystal plasticity model was incorporated into Sandia's finite element analysis code, JAS3D [10] as a standard subroutine. The FEM simulations use eight node (hexahedral) 3D isoparametric elements with a single integration point at the element centroid. To deal with zero energy modes that may arise as a result of the single point integration scheme, the code uses an hourglass control, based on the work of Flanagan and Belytschko [11]. Numerical integration of the constitutive model is performed using a forward Euler scheme. Restrictions are placed on the time step to ensure that the forward integration scheme remains stable. If the step size requested by the user is larger than the allowable size, the step is divided into subincrements of allowable size within the constitutive subroutine.

The first validation test performed was done on a single crystal. The single crystal was represented by a mesh of square cells (MPM) / elements (FEM). As shown in Figure 3.3, the cell/element resolution was taken to be same in both cases i.e. $20 \times 10 \times 10$ cells/elements. In addition, note that in the case of the MPM calculation each cell contains 8 material points. It was

found during the course of this benchmark test, that increasing the number of material points per cell (i.e. increase the resolution of points) did not improve the stress-strain curve results. Consequently, the resolution of 8 materials points per cell was used in the rest of this study. A simple traction loading condition was applied on the single crystal in the X direction, while the Y and Z direction were traction free. The main difference between the FEM and MPM calculation actually resides on the application of these boundary conditions. Indeed, the FEM code used in this study is an implicit time integration code, while the MPM code is a explicit time integration code. Therefore, while JAS3D correspond to quasistatic loading conditions (i.e insensitive to the loading rate), the MPM code does depend on the loading rate. As a result and as shown in Figure 3.3, we performed a series of calculation with different magnitude in the loading step. The smaller the loading step, the closer the MPM calculation to the quasistatic case.

The comparison between the stress-strain curve predicted by MPALE and the one obtained by FEM is shown in Figure 3.3. It is seen that as the loading step becomes smaller the MPM calculation converges toward the quasistatic solution and both methods are in good agreement. This phenomena can be explained by the fact that elastic waves are traveling through the material as it deforms. Applying a smaller loading step reduces the amplitude of these wave and therefore gives is more time to be damped throughout the materials.

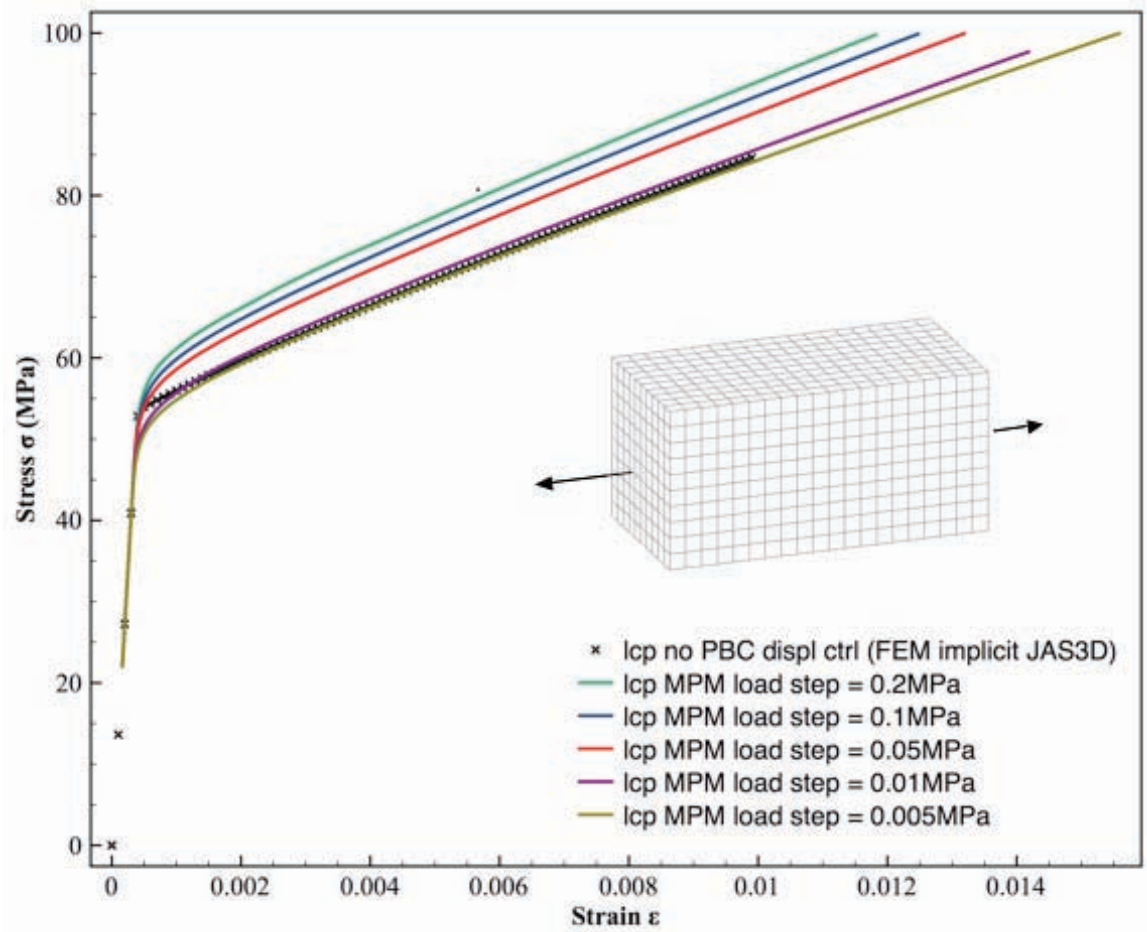

Figure 7.3. Comparison FEM (JAS3D, implicit time integration) vs. MPM (MPALE, implicit time integration) on a single crystal.

The second validation test performed was performed on a polycrystal with square grains. The single crystal was represented by a mesh of square cells (MPM) / elements (FEM). As shown in Figure 3.4, the cell/element resolution was taken to be same in both cases i.e. $40 \times 40 \times 10$ cells/elements. In addition, similarly to the single crystal example, in the case of the MPM calculation, each cell contains 8 material points. Random orientation was assigned to each grain. A simple traction in the X direction was applied to the boundary of the polycrystal while the Y and Z direction were considered traction free.

The comparison between the stress strain curve predicted by MPALE and the one obtained by FEM is shown in Figure 3.4. Contrary to the observations made in the case of the single crystal, we notice that in the case of the polycrystal the choice of the loading step has little impact on the convergence of the results, and both methods (FEM vs. MPM) are in good agreement. This remark can simply be attributed to the fact that in the case of the polycrystal the elastic waves traveling through the microstructure are naturally damped at the grain boundaries due to the discontinuity of the material properties (Dingreville and Bartel, 2009).

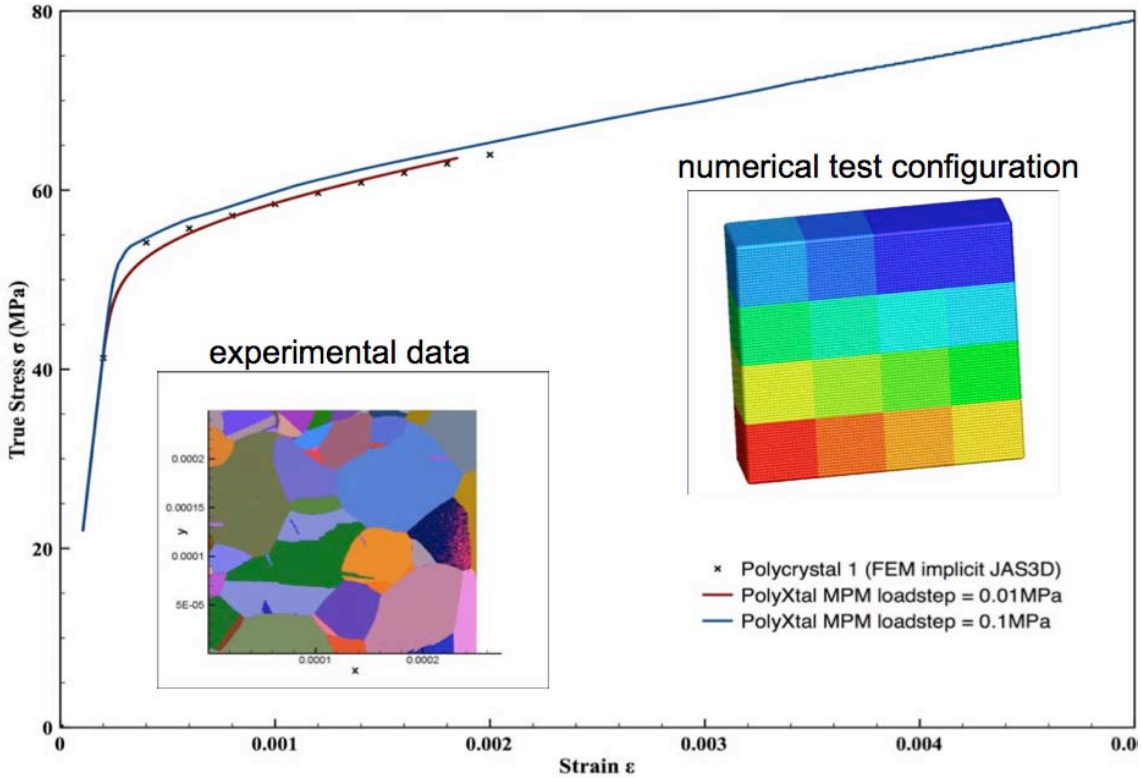

Figure 3.8. Comparison FEM (JAS3D, implicit time integration) vs. MPM (MPALE, implicit time integration) on a polycrystal.

3.2. Stress Fields Generate by Surface Triple-Grain Junctions: Illustrative Finite Element Results (E.D. Reedy (01526)

3.2.1 Introduction

Crack growth in ductile materials often initiates at surfaces. For example, when a pure, polycrystalline ductile metal is subjected to cyclic fatigue, cracks typically nucleate at locations where persistent slip bands intersect the surface [12]. The surface roughness induced by the persistent slip bands is sometimes referred to as extrusions and intrusions. There is also experimental data suggesting microstructural features such grain boundaries and crystallographic orientation effect fatigue-induced crack nucleation at a stress-free surface [13]. Regions of elevated stress within a microstructure are presumably associated with the generation of surface roughness and crack nucleation. It is well known that polycrystalline geometry and texture can introduce non-uniform stress fields under a nominally homogeneous loading. Recent work includes a 3-D finite element analysis of synthetically generated cubic crystal aggregates [14] as well as finite element models based on images of 3D crystalline microstructure [15]. Both studies found that regions of elevated stress were associated with grain boundaries and triple-grain junctions. One challenge when viewing results of such geometrically complex models is identifying correlations between the microstructure and the observed stress state. This complexity has even motivated the use of data-mining techniques [16].

Within the context of linear elasticity theory, material and geometric discontinuities in triple-grain junction-like geometries can give rise to power-law singular stress fields, i.e., $s \sim r^{l}$), where $l < 0$ and r is radial distance from the singular point [17, 18]. It has been shown that the stress intensity factors associated with such singularities can be successfully used in failure analysis in certain cases [19, 20]. There has been considerable effort aimed at studying the asymptotic nature of such singular fields with the primary aim of determining the strength (exponent) of the stress singularity. This has included the case where the joined materials are anisotropic [21, 22]. There has been relatively less work aimed at examining stress singularities within the context of cubic, polycrystalline microstructures and that work has examined interior triple-grain junctions in a columnar, polycrystalline material. Tvergaard and Hutchinson [23] performed an asymptotic analysis for a special symmetric grain geometry and crystal orientation. Picu and Gupta [24] determined the strength of the stress singularity for a range of triple-grain junction angles and crystal orientations.

The present work examines the stress fields generated at a surface triple-grain junction; the point where a grain boundary intersects a stress-free surface (i.e., the third crystal is the empty space adjacent to the surface). A highly idealized, 2-D problem is analyzed to avoid complexity; although the expectation is that the results will provide general insights. Particular emphasis is placed on determining the magnitude of such stress fields (i.e., the generalized stress intensity factor) and characterizing the region dominated by the singularity. The dependence of these quantities on crystal orientations, grain boundary orientation, crystal properties, and grain

length scale and geometry are considered. The goal of this study, which is illustrative rather than comprehensive, is to determine whether the stress fields generated at surface triple-grain junctions could possibly be associated with when and where crack growth nucleates along a polycrystalline surface.

3.2.2 Analysis

A highly idealized, 2D, plane strain problem is analyzed. As shown in Fig. 1, a cluster of four columnar crystals that are adjacent to the stress-free surface are modeled explicitly. There are three hexagonal crystals surrounding a bisected hexagonal (trapezoidal) crystal. The angles w_1 and w_2 define the orientation of the center crystal's grain boundary with respect to the stress-free surface. For a regular hexagon, $w_1 = 120^o$ and $w_2 = 60^o$. The crystals are cubic and have one axis of material symmetry perpendicular to the top surface of the material (i.e. aligned with the out-of-plane normal axis). The in-plane orientation of each crystal is defined independently with respect to the horizontal, 1-axis (i.e., g_a-g_d in Fig. 3.5). This cluster of crystals is embedded in a homogeneous, isotropic effective material with properties based upon random crystal rotations about the out-of-plane axis (see the Appendix for a derivation of the relationships used to calculate the effective elastic properties). The model's length L and width W are chosen so that they have negligible effect on the triple-grain junction local stress fields. Specifically, $L = 2W = 80s$, where $2s$ is the side length of the hexagonal crystal (Fig. 3.5). The model is loaded in uniaxial tension parallel to the stress-free surface to generate a nominally uniform $s_{11}=s^*$.

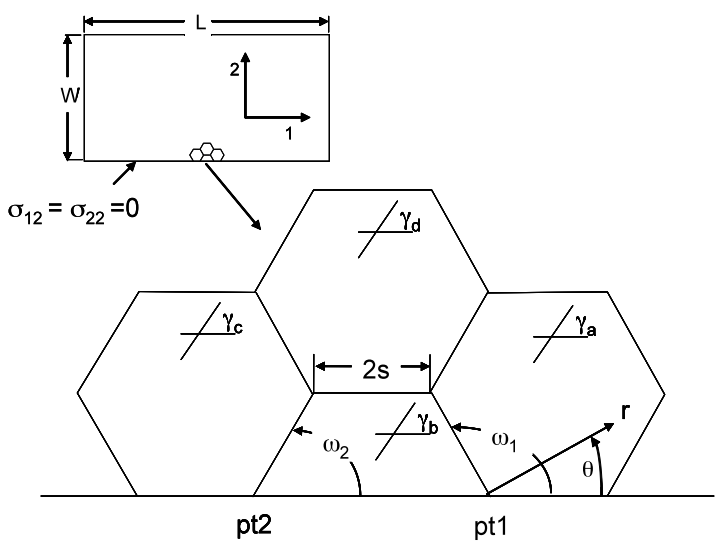

Figure 3.5. Geometry of problem analyzed, uniformly displace right edge relative to fixed left edge in a direction parallel to the stress-free edge to generate a nominally uniform $s_{11}=s^*$.

The finite element mesh is highly refined in the region surrounding the surface triple-junction points, pt1 and pt2, in Figure 3.5 in order to resolve the nature of the stress state at those points. There are twenty-one logarithmically spaced rings surrounding these triple-grain

junction points. The radius of adjacent rings differ by a factor of 1.33, with an inner ring at *r/s*=0.001 (there is a plug of elements of comparable size to those in the first ring at the center of the concentric rings). For the surface triple-grain junctions considered in the present study, it has been determined that when a stress singularity exists, it consists of a single, power-law term with an exponent between minus one and zero. In this case the singular stress state has the form

$$\sigma_{ij} = K_a r^{\lambda} f_{ij}(\theta, \text{grain boundary angle, crystal properties and orientation}) \tag{3.47}$$

with (3.48)

$$K_a = \sigma^* s^{-\lambda} A(\text{microstructure and global geometry})$$

where K_a is the generalized stress intensity factor, r is radial distance from the singular point, l is the strength of the singularity, and the function f_{ij}, which defines the angular variation of the asymptotic stress field, depends on non-dimensional quantities that define the asymptotic problem. The function A in (3.48) is a function of nondimensional material and geometric parameters that define the microstructure and global geometry.

Results for each finite element analysis are used to determine the associated K_a and l values by performing a power-law fit of stress versus distance from the singular point in the region dominated by the stress singularity. In this study, the singularity parameters were determined by fitting the finite element results over the distance *r/s*=0.001 to 0.01 along a ray with $q=0^o$ (pt1) or $q=180^o$ (pt2). The region dominated by the stress singularity is characterized by the quantity r_d. This length is defined as the distance beyond which the power-law fit and the calculated value of s_{rr} along the stress-free edge differ by more than 2% (defined along the ray with $q=0^o$ for pt1 or $q=180^o$ for pt2, i.e., along the stress-free edge and directed away from the center crystal). Since the computed stress singularities will in general have different values of both l and K_a (i.e., A), a direct comparison of singularity fields using these parameters is problematic. For this reason, the value of s_{rr} at two locations along the stress-free edge will be reported (at *r/s* = 0.01 and *r/s* = 0.10). This provides a means of comparing stress fields even when the singularity parameters differ (or even when the fields are non-singular).

In addition to the finite element-based analysis, the Stroh formalism for anisotropic elasticity [25] was used to derive the characteristic equation governing the strength of the singularity for those triple-grain junctions analyzed by the finite element analysis. These results were used to verify the accuracy of the finite element calculations. The Stroh-based anisotropic elasticity analysis also confirms that when a surface, triple-grain junction singularity exists, the singularity is a single power-law term for the material and geometric parameters considered in this study. The use of the Stroh formalism to determine the nature of the asymptotic stress field at material and geometric discontinuities in anisotropic elastic materials is now well established and will not be discussed here. The interested reader can find details on how this type of analysis is performed in references [26-28].

3.2.3 Results

<u>Baseline configuration</u>

Results will first be presented for a baseline configuration. Subsequent sections will present results for material and geometric variations from this baseline. The baseline configuration has regular, hexahedral grains (w_1 =120° and w_2 =60°), a grain side length 2s=10 mm, and crystal orientations of $g_a = g_c = -g_d = 60^o$ and $g_b = 0^o$ (see Fig. 1). The baseline crystal material is copper (Cu) with cubic elastic constants of C_{11}=168 GPa, C_{12}=122 GPa, and C_{66}=76 GPa. The calculated effective isotropic properties for Cu, based on the relationships derived in the Appendix, are E=115 GPa and n =0.354.

Figure 3.6 plots the variation of the stress component s_{11} with distance from pt1 (pt2) along the stress-free edge (along the ray q=0° for pt1 and along the ray q=180° for pt2). Note that s_{11} is the only non-zero, in-plane stress component along the stress-free edge. The stress state is singular at pt1 while that at pt2 is nonsingular. This is consistent with published asymptotic stress analysis results for interior triple-grain junctions that show that there is only a certain range of crystal orientations for a given grain boundary angle that produce singular behavior [24]. The singularity at pt1 is much weaker than that found at a crack tip (-0.17 vs -0.5), but it dominates a very large region. The FEA results are within 2% of the power-law fit for r/s<0.5. Furthermore, stress is elevated over a significant region (s_{11}/s^* >1 for r/s < 0.2).

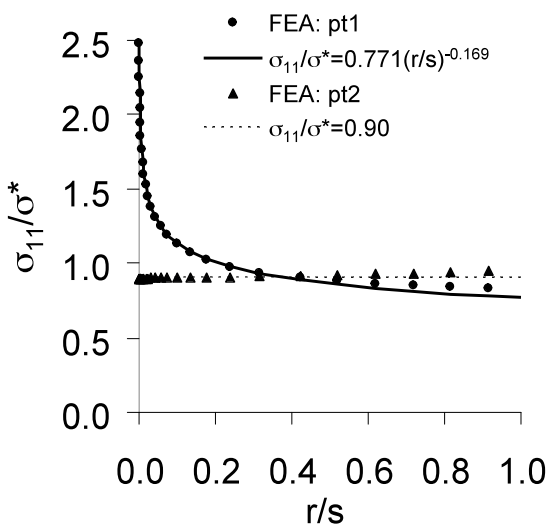

Figure 3.6. Radial stress dependence at pt1 (q=0°) and pt2 (q=180°) for baseline geometry and material.

Figure 3.7 plots the angular variation of the singular stress components about pt1. The f_{ij} functions that define this angular variation (Eq. 3.47) have been normalized by setting $f_{tt}(q=90^o)$ = 1. The plotted results are for the ring with r/s = 0.001, although results for rings with r/s = 0.010 and 0.1000 essentially overlay those for r/s =0.001. This is consistent with the region of dominance suggested by the power-law fit in Fig. 2. Continuity of stress across the grain boundary is reflected in the observed continuity in f_{tt} and f_{rt} at q=120°. On the other hand, f_{rr} can be discontinuous across the grain boundary, and that is the case when there is a stress

singularity. There is also a discontinuity in the slope of f_{rt} at the grain boundary. The magnitude of the stress along the stress-free edge can be quite different in the two adjacent crystals. In the outer crystal (i.e., the crystal to the right of pt1), where g_a=60°, f_{rr}(0°)=1.37, while in the center crystal, where g_b=0°, f_{rr}(180°)=0.9. As Fig. 3.8 shows, the deformed microstructure (highly magnified) is complex and can include shear coupling induced displacements. Although there are differences in detail, the results for the baseline configuration are representative of all the junctions examined.

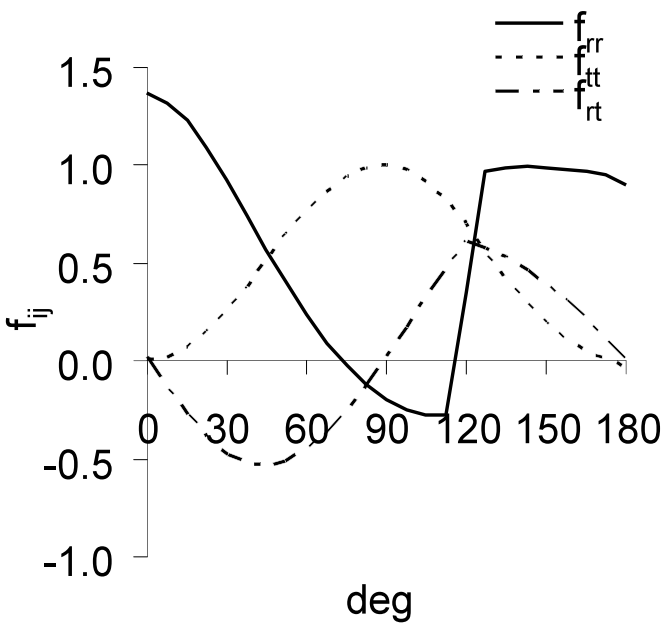

Figure. 3.7. Angular dependence of singular stress at pt1 for baseline geometry and material.

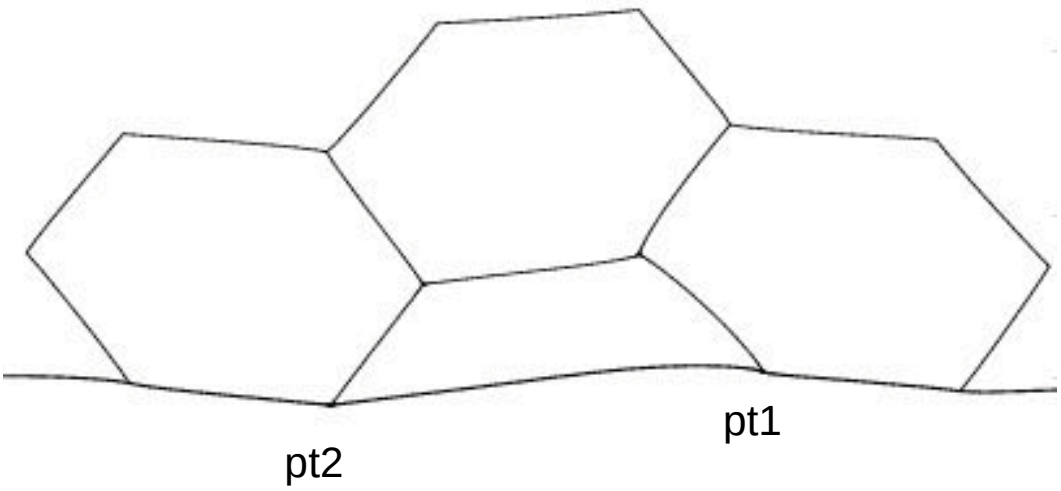

Figure. 3.8. Deformed geometry (highly magnified) for baseline geometry and material.

<u>Effect of crystal properties</u>

Results for the baseline crystal material, copper, are compared with those for nickel (Ni) and silicon (Si) with all other parameters defining the baseline configuration unchanged. The elastic constants used in the nickel (Ni) calculation are C_{11}=248 GPa, C_{12}=155 GPa, and C_{66}=124 GPa, along with computed effective isotropic properties of E=201GPa and n=0.310 for the surrounding bulk. Likewise the elastic constants used in the silicon (Si) calculation are C_{11}=166 GPa, C_{12} =64 GPa, and C_{66}=80 GPa, along with computed effective isotropic properties of E=156 GPa and n =0.222 for the surrounding bulk. The level of crystal anisotropy is often characterized by the parameters R and Q, where $R=(C_{12} + 2C_{66})/C_{11}$ and $Q=C_{66}/C_{12}$, (R=1 for an isotropic material). Table 3.1 compares the calculated results for the stress singularity at pt1. Note that for a specified nominal applied stress s^* and grain side length $2s$, the magnitude of the stress intensity factor K_a scales directly with the value of A (Eq. 3.48). As anticipated, the singular stress field does depend on crystal elastic properties. The strength of the singularity and the stress magnitude at r/s=0.01 and 0.10 are greatest when the crystals are copper. In all cases, the region dominated by the singularity, characterized by r_d, is rather large (>0.5s) and there is a significant elevation in the stress level out to a distance of r/s=0.10.

Table 3.1. Effect of crystal properties on pt1 singular stress state.

	R	Q	A (eq. 2)	λ	r_d/s	$\sigma_{rr}(\theta=0^o)/\sigma^*$ r/s=0.01	$\sigma_{rr}(\theta=0^o)/\sigma^*$ r/s=0.10
Si	1.35	1.25	0.84	-0.058	0.72	1.21	1.06
Ni	1.63	0.80	0.64	-0.133	0.52	1.53	1.12
Cu	1.63	0.62	0.56	-0.169	0.52	1.68	1.13

<u>Effect of crystal orientation</u>

First consider a variation from the baseline configuration where the set of crystal orientations considered have $g_a=g_c=-g_d$, $g_b=0$ (Figure 3.5). The calculated strength of the stress singularity at pt1 for $g_a=0^o$, 15°, 30°, 45°, 60°, and 75° is plotted in Fig. 3.9 ($g_a=60^o$ is the baseline configuration). A stress singularities (l < 0) is generated only when $30^o<g_a<90^o$. Not all surface triple-grain junctions generate a stress singularity. Also plotted in Fig. 3.9 is a curve where the l-values were calculated using the Stroh formalism for anisotropic elasticity. Singularity strengths determined from the finite element analysis are in good agreement with those determined using the Stroh formalism, verifying the accuracy of the finite element approach.

Results that further characterize pt1 and pt2 stress states for the crystal orientations considered in Figure 3.7, as well as results for three other sets of crystal orientations, are presented in Tables 3.2 and Table 3.3, respectively. These results suggest the following general observations. First, there are combinations of crystal orientation that generate elevated stress of more than 1.4*s** for *r/s* < 0.1. Consequently, surface triple-grain junctions are likely to influence when and where plastic deformation occurs. Second, the magnitude of the elevated stress can be affected by grains other then those at the singular point (e.g., Table 3.2: $g_a=60^o$, $g_b=0^o$, $g_c=60^o$, $g_d=-60^o$ vs. $g_a=60^o$, $g_b=0^o$, $g_c=60^o$, $g_d=0^o$). Presumably local variations in orientation-induced stiffness can effect load transfer within a microstructure and influence to what extent a stress singularity is excited. Thirdly, orientation combinations with a more negative *l* (stronger singularity) do not necessarily generate a higher stress at *r/s* = 0.1 (e.g., Table 3.3: $g_a=60^o$, $g_b=75^o$, $g_c=15^o$, $g_d=-15^o$ vs. $g_a=30^o$, $g_b=0^o$, $g_c=30^o$, $g_d=-30^o$). A higher K_a (i.e., *A*) can compensate for a weaker singularity (smaller –*l*).

Table 3.2. Effect of crystal orientation on pt1 singular stress state.

γ_a (°)	γ_b (°)	γ_c (°)	γ_d (°)	A (eq. 2)	λ	r_d/s	$\sigma_{rr}(\theta=0^o)/\sigma^*$ r/s=0.01	$\sigma_{rr}(\theta=0^o)/\sigma^*$ r/s=0.10
0	0	0	0	-	-	-	0.78	0.78
15	0	15	-15	-	-	-	0.66	0.75
30	0	30	-30	-	-	-	0.90	0.90
45	0	45	-45	0.708	-0.113	0.62	1.55	1.19
60	0	60	-60	0.562	-0.169	0.52	1.68	1.13
75	0	75	-75	0.606	-0.108	0.52	1.20	0.93
60	0	60	0	0.726	-0.168	0.18	2.16	1.48
60	45	30	-45	1.091	-0.078	0.08	1.73	1.41
60	75	15	-15	0.850	-0.077	0.82	1.38	1.16

Table 3.3. Effect of crystal orientation on pt2 singular stress state.

γ_a (°)	γ_b (°)	γ_c (°)	γ_d (°)	A (eq. 2)	λ	r_d/s	$\sigma_{rr}(\theta=180^o)/\sigma^*$ r/s=0.01	$\sigma_{rr}(\theta=180^o)/\sigma^*$ r/s=0.10
0	0	0	0	-	-	-	0.78	0.78
15	0	15	-15	0.606	-0.108	0.52	1.20	0.93
30	0	30	-30	0.562	-0.169	0.52	1.68	1.13
45	0	45	-45	0.708	-0.113	0.62	1.55	1.19
60	0	60	-60	-	-	-	0.90	0.90
75	0	75	-75	-	-	-	0.66	0.75
60	0	60	0	-	-	-	0.96	0.98
60	45	30	-45	1.091	-0.078	0.08	1.73	1.41
60	75	15	-15	0.883	-0.139	0.10	2.10	1.50

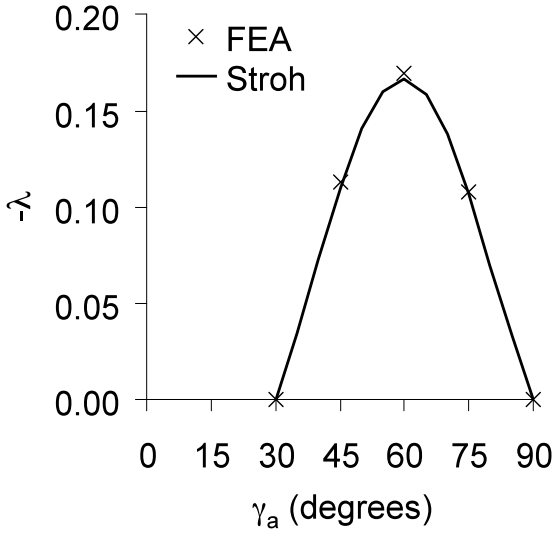

Figure 3.9. FEA results for the variation of -l with g_a at pt1 of the baseline configuration with g_a=g_c=-g_d, and g_b= 0° are compared with asymptotic -l values determined using the Stroh formalism for anisotropic elasticity.

Size effects

As in linear elastic fracture mechanics, there is an intrinsic size effect for a triple-grain junction, with side length 2*s* playing the role of crack length. A uniform increase in the size of all crystals results in a K_a value that scales as s^{-l} (Eq. 48). Therefore for a specified *s**, stress at a fixed radial distance *r* from the singular point scales as s^{-l}. For example, if the value of *s* for the baseline configuration is increased from 5 mm to 10 mm, the magnitude of the stress at a fixed distance *r* from the singular point will increase by a factor of 1.12, provided that this position is within the region dominated by the stress singularity (i.e. $2^{0.169}$ = 1.12).

The effect of increasing the size of only some of the crystals is less obvious. To examine this effect, the embedded crystal geometry shown in Fig. 3.10 was analyzed. Here the center crystal geometry is the same as that of the baseline, but the size of the surrounding crystals is increased. Results for the baseline geometry (Figure 3.5) are compared to the Fig. 3.10 geometry in Table 3.4. These results are for pt1, with g_a=g_c =-g_d, g_b=0 and *s*=5 mm. Note that since the grain boundary angle w_1 (Figure 3.5) is the same for both crystal aggregate geometries, both geometries will generate the same *l* value for the specified g_a (i.e., they share the same asymptotic problem). This limited set of results indicate that there is no consistent trend; the stress at a fixed *r* can either increase or decrease when the center crystal is surrounded by larger crystals.

Table 3.4. Effect of crystal size on pt1 singular stress state.

geometry	γ_a (°)	A (eq. 2)	λ	r_d/s	$\sigma_{rr}(\theta=0^o)/\sigma^*$ r/s=0.01	$\sigma_{rr}(\theta=0^o)/\sigma^*$ r/s=0.10
Fig. 1	60	0.562	-0.169	0.52	1.68	1.13
Fig. 6	60	0.515	-0.170	0.13	1.54	1.03
Fig. 1	45	0.708	-0.113	0.62	1.55	1.19
Fig. 6	45	0.735	-0.113	0.62	1.61	1.24

<u>Effect of grain boundary angle</u>

A limited number of calculations were also performed to examine the effect of grain boundary angle of the stress state at triple-grain junction. The same microstructural geometry shown in Figure 3.10 was analyzed, except pt1 (pt2) were moved to change the grain boundary angle w_1 (w_2) from 120° (60°) to 90° (90°) or 150° (30°). As anticipated, the grain boundary interface angle affects the nature of the triple-grain junction stress field. Table 3.5 presents results for pt1. In the cases examined, the stress state is non-singular when the grain boundary interface is perpendicular to the stress-free edge. Interestingly, in one of the cases examined, where g_a=45°, g_b=0°, g_c=45°, g_d=-45°, the magnitude of the nonsingular stress field is quite high with $s_{rr}(q=0^o)/s^*$=1.6 at r/s=0.1. Examination of the calculated results showed stress generated by a undulation along the stress-free surface in the region of the triple-grain junction (Figure 3.11). The peak stress does not occur at the triple-grain junction, but at *r/s*=0.042. It should be noted that the S_{11} compliance component of the copper crystal, when rotated at 45° to the 1-axis, is about half that of the unrotated compliance. Consequently, there is a large mismatch in local 1-direction compliance. This result shows that some crystals in a polycrystalline aggregate might be subjected to relatively high stress even when the triple-grain junction stress field is non-singular. Large compliance mismatches can influence crystal deformation and load transfer through a crystal aggregate. Clearly, one can not simply ignore all nonsingular triple-grain junctions. Regions of large differences in local compliance in the direction parallel to the stress-free edge should also be considered.

Table 3.5. Effect of grain boundary interface angle on pt1 singular stress state.

ω (°)	γ_a (°)	γ_b (°)	γ_c (°)	γ_d (°)	A (eq. 2)	λ	r_d/s	$\sigma_{rr}(\theta=0)/\sigma^*$ r/s=0.01	$\sigma_{rr}(\theta=0)/\sigma^*$ r/s=0.10
90	45	0	45	-45	-	-	-	1.57	1.60
90	0	45	0	-15	-	-	-	0.65	0.77
90	0	15	0	0	-	-	-	0.80	0.81
150	45	0	45	-45	-	-	-	0.42	0.59
150	75	0	75	-75	0.690	-0.040	0.24	0.83	0.77
150	75	15	75	-75	0.694	-0.142	0.13	1.40	1.02

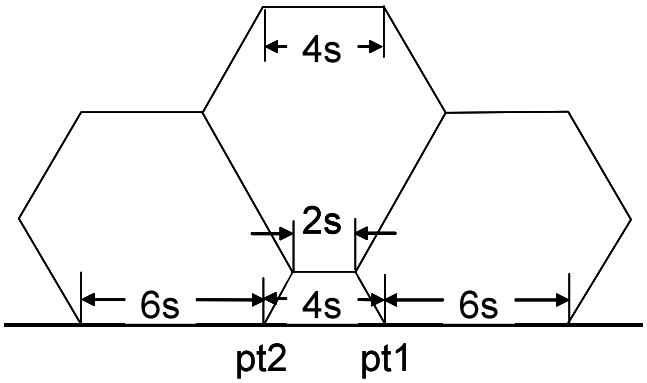

Figure 3.10. Geometry of model used to examine effect of surrounding a crystal with larger crystals.

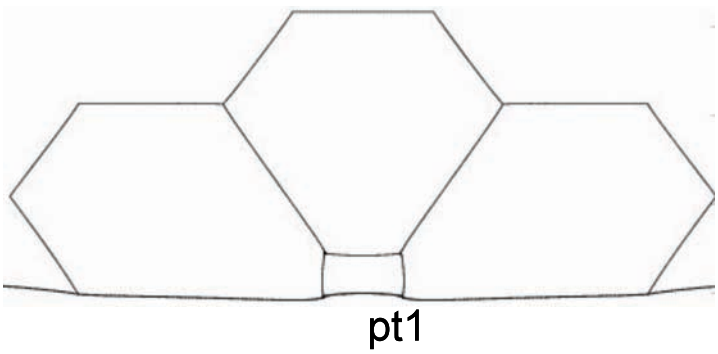

Figure 3.11. Deformed geometry (highly deformed) for case where w_1=90° and with g_a=45°, g_b=0°, g_c= 45°, and g_d=-45°.

3.2.4 Discussion

The combinations of crystal and grain boundary orientations that generate a singular stress state can be determined by an analysis of the asymptotic problem. This type of analysis can determine the strength of the singularity *l*, but cannot determine the magnitude of the stress in the region dominated by a triple-grain junction. The magnitude of the stress field at a triple-grain junction and the size of the region dominated by the singular field can only be determined by performing a full solution of the polycrystalline aggregate of interest. In this work, a finite element analysis that utilized a highly refined mesh about the triple-grain junction was used to

fully determine the nature of the stress singularity (i.e., determine l and K_a). Many of the results published in the literature attempt to model complex polycrystalline microstructures, but do so using a relatively coarse mesh. The existence of a region of highly elevated stress adjacent to a triple-grain junction might not be apparent in such an analysis. One alternative approach is to use results, such as those reported here, to help identify triple junctions of particular interest and refine the mesh accordingly. One might expect that there are relatively few combinations of crystal and grain boundary orientations that generate stress levels that are significantly higher than the nominal value. However, as the results reported here show, there is no definitive method for picking out that one triple-junction that is of most interest. Local variations in orientation-induced stiffness can effect load transfer within a microstructure and influence to what extent a stress singularity is excited. Furthermore, there can be special cases where significantly elevated stress is generated near a triple-grain junction that has a nonsingular stress field. Regions of large differences in local compliance in the direction parallel to the stress-free edge should also be considered. Nonetheless, one should be able to narrow the universe of possibilities.

The asymptotic analysis indicates that there are specific combinations of grain boundary and crystal orientations that generate a non-singular triple-junction stress state with l=0 (e.g., Figure 3.9). Simple considerations permit the identification of such combinations.
A triple-grain junction stress singularity is associated with a discontinuity in the radial stress s_{rr}(q=w) across the grain boundary interface (see Figure 3.7). Note that interfacial stress and displacement continuity conditions at the interface permits, but does not require, a radial stress discontinuity to exist. There might be certain combinations that generate a fully continuous stress state across the interface, and those combinations should generate a nonsingular triple-grain junction.

Figure 3.12 shows to half-planes separated by an oblique interface defined by the orientation w that separates two cubic crystals that differ only in their crystal orientation. Material A has crystal orientation g_a while material B has crystal orientation g_b. The half-plane is subjected to a uniform stress $s_{11}=s^*$, which is consistent with the stress-state found along the stress-free edge of the triple-grain junction asymptotic problem. The interfacial continuity conditions are:

$$\sigma_{r\theta}^{a}(\theta=\omega)=\sigma_{r\theta}^{b}(\theta=\omega)=-\sigma^{*}\sin(\omega)\cos(\omega) \qquad (3.49)$$

$$\sigma_{\theta\theta}^{a}(\theta=\omega)=\sigma_{\theta\theta}^{b}(\theta=\omega)=\sigma^{*}\sin^{2}(\omega) \qquad (3.50)$$

$$\varepsilon_{rr}^{a}(\theta=\omega)=\varepsilon_{rr}^{b}(\theta=\omega) \qquad (3.51)$$

where the superscripts a and b identify the cubic material with crystal orientation g_a and g_b, respectively.

Combinations of w, g_a, and g_b that generate

$$\sigma_{rr}^{a}(\theta=\omega)=\sigma_{rr}^{b}(\theta=\omega)=\sigma^{*}\cos^{2}(\omega) \qquad (3.52)$$

are of interest. Now, one can express the strain compatibility requirement (3.51) in terms of the associated stress components through the crystal's compliance components S_{ij}^{*}.

$$\varepsilon_{rr}^{a}(\theta=\omega)=S_{11}^{*'}(\omega-\gamma_a)\sigma_{rr}^{a}(\theta=\omega)+S_{12}^{*'}(\omega-\gamma_a)\sigma_{\theta\theta}^{a}(\theta=\omega)+S_{16}^{*'}(\omega-\gamma_a)\sigma_{r\theta}^{a}(\theta=\omega) \quad (3.53)$$

$$\varepsilon_{rr}^{b}(\theta=\omega)=S_{11}^{*'}(\omega-\gamma_b)\sigma_{rr}^{b}(\theta=\omega)+S_{12}^{*'}(\omega-\gamma_b)\sigma_{\theta\theta}^{b}(\theta=\omega)+S_{16}^{*'}(\omega-\gamma_b)\sigma_{r\theta}^{b}(\theta=\omega) \quad (3.54)$$

Note that plane strain cubic crystal compliances must be transformed to the 1'-2' coordinate system, which is aligned with the interface, from the coordinate system in which they are defined (e.g., for material A, a rotation of w-g_a, since the cubic material A is aligned at an angle g_a from the 1-axis).

The governing equation is then defined by substituting Eqs. 3.49, 3.50, and 3.52 into Eqs. 3.53 and 3.54, and then equating Eqs. 3.53 and 3.54. The resulting relationship is

$$\begin{aligned}&(\cos(4(\omega-\gamma_a))-\cos(4(\omega-\gamma_b)))\cos^2(\omega)\\&-(\cos(4(\omega-\gamma_a))-\cos(4(\omega-\gamma_b)))\sin^2(\omega)\\&+2(\sin(4(\omega-\gamma_a))-\sin(4(\omega-\gamma_b)))\sin(\omega)\cos(\omega)=0\end{aligned} \quad (3.55)$$

Interestingly, Eq. 3.55 depends only on w, g_a, and g_b (i.e., there is no dependence on the crystal compliances). Eq. 3.55 can be further simplified to yield

$$\cos(4\gamma_a-2\omega)-\cos(4\gamma_b-2\omega)=0 \quad (3.56)$$

Eq. 3.56 has two solutions

$$\gamma_a=\gamma_b+n\frac{\pi}{2} \quad \text{where } n=\text{integer} \quad (3.57)$$

$$\omega=\gamma_a+\gamma_b+n\frac{\pi}{2} \quad \text{where } n=\text{integer} \quad (3.58)$$

The Eq. 3.57 solution is the trivial result that the stress state is continuous across the grain boundary interface when the two adjoining crystals have the same orientation (additional 90° rotations do not effect the cubic crystal properties). Eq. 3.58 is the more interesting result and test calculations confirm that l=0 when w=g_a+g_b (e.g., see Figure 3.9).

There is one other choice of orientation parameters that generates a nonsingular stress field; whenever w=90° for all g_a and g_b. When the grain boundary interface is normal to the stress-free edge, consistency with the stress-free boundary condition requires that the radial stress along the boundary equals zero in both materials A and B (e.g., see Table 3.5).

These simple relationships (Eq. 3.57 and 3.58) provide a demarcation between ranges of orientations that generate either singular or non-singular triple-grain junction stress states.

Finally note that the surface triple-grain junction that generates the highest shear stress is not necessarily the junction where plastic flow will first initiate. Slip is generated by the shear stress that acts on the available crystal slip systems. A junction that generates a lower shear stress, but is better aligned with a slip system, could be the first to initiate plastic flow. To explore this possibility, one can use the calculated surface triple-grain junction stress field and resolve the stress on the available slip systems for that particular crystal orientation. See, for example, the approach used by Feron, Zhang, and Suo [29] to determine the critical slip system at a sharp corner in strained silicon. Note that along the stress-free interface, the in-plane stress is uniaxial, so the maximum in-plane shear is at +/- 45° with respect to the stress-free surface.

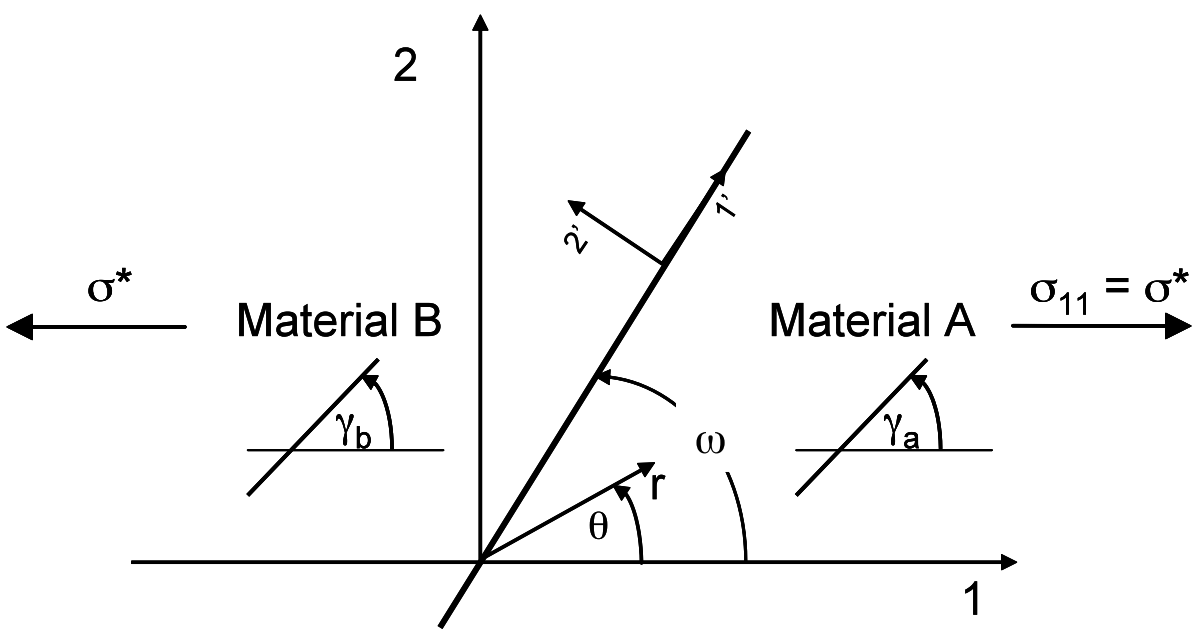

Figure 3.12. Problem analyzed to determine w, g_a and g_b combinations that generate a continuous s_{rr} across the grain boundary.

3.2.5 Summary

The stress field generated at surface triple-grain junction (the third crystal is the empty space adjacent to the surface) was investigated by analyzing an idealized, plane strain problem that embedded four columnar cubic crystals within an effective isotropic media. When a surface triple-grain junction singularity exists, it can be described by a single, power-law singular term.

This stress singularity is much weaker than that found at a crack tip (e.g., -0.17 vs. -0.5) although the region dominated by the stress singularity can be relatively large. The illustrative calculations performed in this study identified grain boundary and crystal orientation combinations that generate stress levels that exceed the nominal applied stress by 40% at a distance equal to 5% of the crystal's side length. Those triple-grain junctions that generated significantly higher elevated stress were almost exclusively those associated with a relatively strong power-law stress singularity. Some crystals in an aggregate, however, are subjected to high stress even when the triple-grain junction stress field is non-singular. Compliance mismatches between neighboring crystals can influence local crystal deformation and load transfer through a crystal aggregate. It would seem that one cannot simply ignore all nonsingular triple-grain junctions. Regions of large differences in local compliance in the direction parallel to the stress-free edge might also be regions of significantly elevated stress. The overall conclusion of this work is that only a few special triple-grain junctions along a surface may dominate behavior and possibly influence where a persistent slip band will nucleate. The type of analysis reported here may allow one to identify those triple-grain junctions that should be observed more closely in an experimental study or analyzed in greater detail in a numerical simulation.

3.3. Advancement in an Analytically Enriched XFEM (J.V. Cox (01524))

3.3.1 Introduction

This component of the LDRD project addressed a computational approach to fracture modeling that has several advantages over more traditional finite element approaches (*e.g.*, smeared crack, embedded discontinuity, and interface element formulations). In particular it addresses the changing topology associated with propagating cracks, via the underlying basis functions for the approximation (*i.e.*, shape functions from an element perspective) rather than through changes in the mesh topology or constraining the crack to propagate along existing element edges. That is, the basis functions themselves contain the discontinuity. It also models the crack opening as being continuous across elements and their boundaries. While these are desirable attributes they come at a price. In typical implementations, additional degrees of freedom (associated with the additional basis functions) are adaptively added to nodes as the crack propagates. Some codes are not structured to have an arbitrary number of degrees of freedom, and so clever alternatives (*e.g.*, introducing coincident elements) have been adopted.

Finite element methods that augment the basis locally to enrich the approximate solution with features that the typical polynomial basis can not either represent or can not represent efficiently are generically referred to as *enriched methods*. To maintain the local support and continuity of the solution between elements, [30] introduced the partition of unity finite element method (PUFEM). The PUFEM name reflects the form of the enrichment; the approximate solution space was enriched locally by a product of enrichment functions and a set of functions that constituted a "partition of unity." The partition of unity (typically either a subset of the original basis functions or a basis of a different order) has the key property that the sum of the functions has a value of unity at all points in the desired region of enrichment. As an example, one could use quadratic elements but use the bilinear shape functions associated with the corner nodes as the partition of unity. The displacement in the element then has contributions from the original shape functions and from the product of the shape functions associated with the partition of unity and enrichment functions. This can represented by the expression

$$\mathrm{u}(\mathrm{x}) = \sum_{i=1}^{N_N} \mathbf{N}_i(\mathrm{x})\mathrm{u}_i + \sum_{j=1}^{N_\Lambda}\sum_{i=1}^{N_{N^*}} \Lambda_j(\mathrm{x})\mathbf{N}_i^*(\mathrm{x})\alpha_{ij} \tag{3.59}$$

where

$N_i(\mathbf{x})$ ~ shape functions for the element,

$N_i^*(\mathbf{x})$ ~ shape functions associated with the partition of unity

$\Lambda_j(\mathbf{x})$ ~ enrichment functions

u_i ~ degrees of freedom associated with the nodal shape functions

a_{ij} ~ degrees of freedom associated with the enrichment.

In Melenk and Babuska's work an underlying motivation was to incorporate analytically derived functions in the basis for the approximate solution space: for example, terms from a series solution for a re-entrant corner.

Belytschko and Black [31] were the first to exploit the partition of unity properties for enrichment of linear elastic fracture mechanics (LEFM) problems. Their enrichment functions consisted of the four linearly independent functions that occur in the asymptotic solution for the

displacement field. (For an early review of the related works on fracture, see Karihaloo and Xiao [32].) Belytschko and colleagues presented several advancements and referred to their method as the *extended finite element method* (XFEM) (Sukumar *et al*. [33]) distinguishing it from the standard PUFEM in its representation of geometric features (*i.e.*, the crack) by the enrichment functions.

3.3.2 Previous SNL Work on the Analytically Enriched XFEM

For cohesive crack problems the literature abounds with studies that have used generalized Heaviside or sign functions for enrichment. Their simplicity facilitates implementation, and they are sufficient to allow the discontinuity of the crack to be introduced. The use of analytically based enrichment functions for XFEM, while common for LEFM, has been very limited for the cohesive-crack problem. The only studies I am aware of are those conducted at Sandia (see *e.g.*, Cox [34, 35]) and those of Xiao and Kariloo [36]. The motivation for analytical enrichment (both for LEFM and cohesive crack mechanics) is one of "efficiency of scale." That is given a sufficiently fine mesh one can always use Heaviside enrichment to model a crack. For some problems in which LEFM is applicable, *i.e.*, the process zone can be idealized in 2D as a point, the scale of discretization necessary to resolve a cohesive zone idealization can be very small. In some cases adaptive mesh refinement would have to be used in conjunction with XFEM to make the problem tractable. The same issue exists for cohesive crack problems, just not to the same degree. In both cases, the potential exists for using a relatively coarse mesh that is sufficient to represent the gross response and capturing the local response in the vicinity of the crack via the analytical enrichment. To advance the XFEM toward the goal of applying it to future micro-structural investigations of fatigue, we sought to investigate and improve the accuracy of an analytically enriched formulation that was recently further developed under Sandia ESRF funding (Cox [34]).

The earliest work on this analytically enriched XFEM, was aimed at proving the concept by showing the quasi-static propagation of a mode-I cohesive crack across a square domain could be accurately reproduced. Since the analytical solutions [37, 38] that were the underlying sources of the enrichment functions were based upon ideal quasi-brittle fracture (*i.e.*, the zone of plastic hardening or perfect yielding was assumed to be negligibly small – Bazant and Planas [39]), the first test problems were idealized as being quasi-brittle too. From the viewpoint of investigating the strengths and weaknesses of the numerical formulation, the added simplicity, relative to ductile fracture, makes the evaluation more straightforward. For example, if (1) the bulk material is idealized as being elastoplastic and (2) the localized elements are integrated in a manner that accounts for the location of the crack, internal variables for the elastoplastic model must be mapped to new points with the change of the integration scheme. This additional error source makes it more difficult to initially evaluate the merit of the enrichment functions. Obviously, the more complex problem must be addressed to assess the applicability of the enrichment functions to ductile fracture (the subject of an on-going ESRF project), but other more general issues that affect the solution accuracy were addressed in this study, namely: (1) curved crack mapping, (2) "stress field smoothing" (also called "stress extraction"), (3) stress relief for multiple cracks, and (4) effects of anisotropy on the accuracy.

3.3.3 Extensions to Mixed-Mode Fracture

Once the potential of the formulation was demonstrated for mode-I cracking, the formulation was extended to mixed-mode cracking. This project contributed by addressing

issues (1) and (2) listed above, which were critical for effective mixed-mode solutions. For a particular test problem, (3) was also potentially important.

Analytical solutions used for enrichment, have the underlying assumption that the crack is straight. To address curved cracks, a mapping must be used to map from the "actual curved" crack to the straight crack of the analytical solution. The earliest formulations for LEFM (Belytschko and Black [31]) included a curved-crack mapping algorithm. Consistent with the early mapping algorithms, the module that contained the enrichment functions in this formulation had a piecewise linear description of the crack geometry, the defining points of which corresponded to the intersects with the element edges. The module did not however have access to the mesh data. In brief, the algorithm used the simple idea that each response point ($\mathbf{x}^r$) in the domain was associated with a particular segment of the crack, initially determined by the first segment that satisfied the inequality

$$\left(\mathbf{x}^r - \mathbf{x}_2^s\right) \cdot \mathbf{t}^s > 0 \tag{3.60}$$

where

$\mathbf{x}_2^s$ ~ coordinates of the second end point of segment *s*. The second point is further from the cohesive zone tip, as measured along the crack path.

$\mathbf{x}_1^s$ ~ coordinates of the first end point of segment s.

$\mathbf{t}^s$ ~ tangent vector for the segment, $\mathbf{x}_1^s - \mathbf{x}_2^s$.

This is graphically depicted in Figure 3.13 for the point $\mathbf{x}^r$. As illustrated in the figure the initial association of the point with segment 1 is updated when it is determined that segment *n* also satisfied the inequality and is closer than segment 1. Once the associated segment is determined the local coordinates relative to the crack tip are determined from (1) the perpendicular distance (*y*) and (2) the sum of the segment lengths from the crack tip to $\mathbf{x}_1^s$ plus a scaled tangential distance between the norms of the end points, $\mathbf{n}^s$ and $\mathbf{n}^{s-1}$, (*x*). Note that the scaling simplifies the expressions, relative to some mapping schemes in the sense that trigonometric functions are not directly used in the mapping.

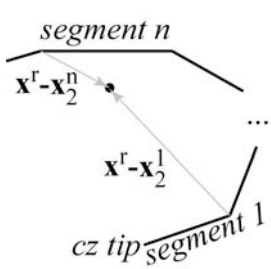

Figure 3.13. Curved crack segment association.

A common approach is to use the analytical enrichment "near the crack tip," and then to switch to Heaviside enrichment in the wake of the crack. For some implementations, "near the crack tip" simply translates to "for the element containing the crack tip." For brevity, the results shown here adopt analytical enrichment over the length of the crack. (Reference Cox [34, 35]for earlier related work that examined both enrichment schemes.)

For a displacement-based FEM solution, secondary variables such as stress are approximated less accurately. In particular, for an un-enriched 4-node quadrilateral element (as used in study), displacements are second order accurate and stresses are first order accurate. Further more, while the displacement field is continuous, the stress field is discontinuous. Less accuracy in the stress field led to arrestment of the crack at element edges (Cox [34]). In addition to crack arrestment, inaccuracy of the stress field can significantly affect the approximation of the crack direction (*e.g.*, when based upon the principal stress direction). For analytical enrichment, these inaccuracies can be more significant, since the enrichment should allow one to use a coarser mesh. Two approaches that previous researchers have adopted are to use a polynomial approximation or a nonlocal measure of the stress field. In this study the two are combined in a weighted least squares approximation of the stress field. Let the difference between the FE approximation and that of polynomial representation be given by $d(\mathrm{x}) = \sigma^{p}(\mathrm{x}) - \sigma^{xfem}(\mathrm{x}) = c_0 + c_1 x + c_2 y + \ldots - \sigma^{xfem}(\mathrm{x})$. A weighting function is adopted from the nonlocal constitutive model work of Bazant and Pijaudier-Cabot [40] as $\Omega(\mathrm{x}) = \exp\left[-\omega\left(r/L_{\omega}\right)^2\right]$ where w and L_{w} are weighting parameters, and r is the distance to the position x. A weighted difference can be defined as $R^2 = \int_A \left[\Omega(\mathrm{x})d(\mathrm{x})\right]^2 dA$ and minimized (with respect to $\{\mathrm{c_i}\}$) using the method of least squares. The area (A) is taken to be a disk or half-disk defined by a radius, r_s., and integration is approximated using $\mathrm{s}^{\mathrm{xfem}}$ values at element gauss points. In the limits, the relations provide a nonlocal stress measure ($s^p = c_0$) or a least-squared polynomial fit (w=0). This calculation was applied to each component of the stress field to evaluate initiation, crack direction, and propagation.

The effect of smoothing on the accuracy of the crack propagation history (for a single mode I test problem) is shown to be approximately equivalent to halving the element size [35]. However, without using the smoothing the crack path can be artificially jagged – *i.e.*, the lack of smoothness is due to numerical not physical sources.

For problems, that involve multiple cracks and stable quasi-static propagation, the potential for stress relief of one crack due to opening of another should be considered. This was relevant to the commonly used example examined in this study [35]. To address this, a multi-level solver scheme only allowed one crack to initiate or propagate at a time – the one that satisfied the criterion most strongly. A new equilibrium solution was then obtained and potential points of initiation or propagation were re-evaluated. Execution continued in this level of the solver until no further initiation or propagation occurred for the load step.

3.3.4 Application to an Orthotropic Material

An aspect of the study that was not previously documented, is an examination of the accuracy of the formulation when underlying assumptions for the analytically derived enrichment functions are violated. In particular, the effect of relaxing the assumption of an isotropic material is examined here. For simplicity, the model problem previously presented to evaluate the formulation for quasi-brittle fracture [34, 35] is re-examined for an orthotropic material with the Young's modulus for one principal material direction perturbed. Previous analyses of this model problem focused on the ability of the formulation to represent the

propagation history of the cohesive zone and crack tip. For the current investigation, we examine the accuracy in the fields for the crack at a particular state – the tip of the cohesive zone on centerline. Figure 3.14 depicts the plane stress model problem. The previous isotropic properties were given as E= 37 GPa, and n=0.17. For this illustrative study only the boundary conditions for problem 1 are addressed. To access the accuracy of the fields, reference solutions using very finely meshed FEM domains were obtained. Figure 3.15 shows the mesh for the cracked domain case, which is concentrated near the center.

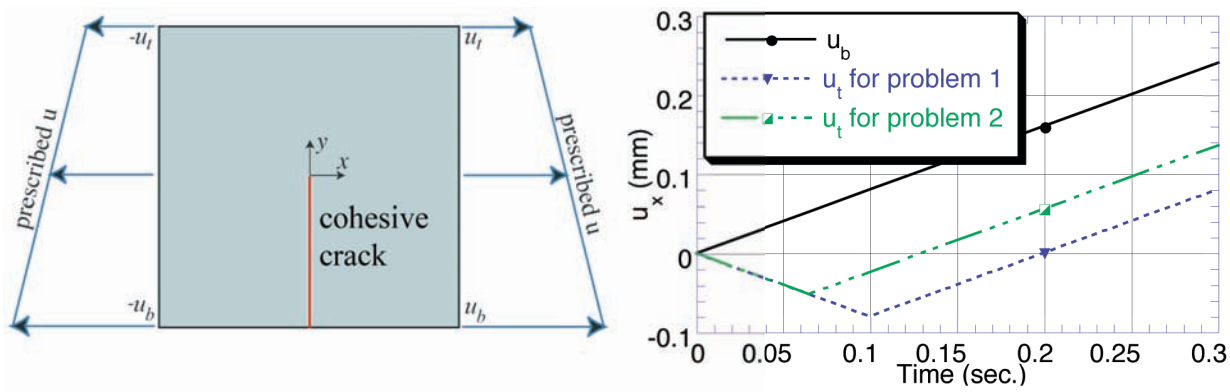

Figure 3.14. Model problem at the state of the cohesive crack extending to the center.

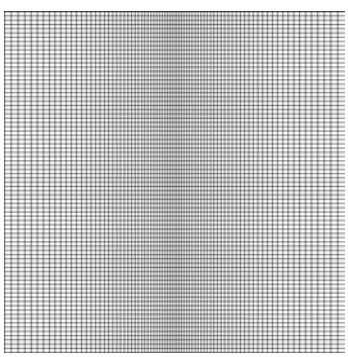

Figure 3.15. Reference solution mesh – 81x80.

Using an approximate reference solution can be problematic. First of all, it is more difficult to calculate a norm of the difference between the two solutions, compared with an exact reference solution, which can easily be sampled at an arbitrary point. Secondly, if the reference solution is not sufficiently accurate, the norm of the difference is not an accurate representation of the error. To calculate error norms a new utility was created, that would allow either exact or approximate reference solutions. Part of the motivation for creating a new utility is that XFEM

elements had a variable number of gauss points depending upon if they were un-enriched, enriched but not localized, and enriched and localized. The standard FE quad element and the XFEM quad element were modified to give both displacements and their gradients at element gauss points. The difference or "error" calculations were integrated using the gauss points of the coarse mesh solution (later to be the XFEM solution). To sample the "same points" of the reference solution a similar smoothing technique, as described in the previous section, was implemented. In this application since the reference solution had a significant spatial variation in the mesh density, the number of closest neighbors was prescribed instead of prescribing the size of the neighborhood. Smoothing was limited to polynomial fitting (*i.e.*, the weighting function was unity), and parameter studies were conducted to examine the effect of using different orders of polynomial and different numbers of neighbors. The results showed that if the problem is not sufficiently over-determined (*e.g.*, a linear polynomial based upon 4 neighbors), the error calculations can be inaccurate. With a sufficient number of neighbors, constant, linear, and quadratic polynomials all gave consistent results, typically agreeing in 2 to 5 digits. Most of the results presented here used a second order polynomial and 32 neighboring points.

To both verify the correctness of the norm calculations and the validity of using an approximate reference solution, first the simpler problem of the square domain subjected to bending without cracking was considered. The *x*-component of displacement was displaced as depicted in Figure 3.14 (for time<0.1). The *y*-component of displacement along each edge was held relatively fixed, with an extremely stiff "end plate." An exact solution was obtained using Euler-Bernoulli beam theory for the special case of n=0. Approximate solutions were obtained for meshes of 4x4, 8x8, 16x16, and 32x32 elements. Linear relationships (on a log-log plot) between the relative norm of the error in the displacement field and relative element size gave slopes of 1.99 for the exact reference solution and 2.07 for the approximate reference solution – both reflecting second order convergence of the displacements. For this study the accuracy for a given mesh is emphasized more than the rate of convergence, but examining the rate of convergence allows us to both verify the norm calculation and evaluate the use of an approximate reference solution. Defining $n \neq 0$, complicates the problem some due to the constraints along the sides. This is reflected in Figure 3.16, where the apparent rate of convergence increases to 2.3-2.4 (depending upon the smoothing parameters used). (Note that the initial version of the norm calculator only included Sobolev norms, so $\|.\|_0$ denotes a 0-Sobolev norm – equivalent to the L_2 norm of the displacements or their errors. L ~ 1 m – the size of the domain, h ~ element height, and U_{ref} ~ the displacement field for the reference solution.) The greater deviation from the theoretical optimum is attributed to the more complicated response near the corners of the domain, but there are two contributing factors: (1) the reference solution is further from the exact solution, and (2) the error is more difficult to integrate. While the 2x2 integration is sufficient to integrate the elements' stiffness and residual contributions, the error field may require more accurate integration. To examine this the same analyses are conducted with elements that are over-integrated (4x4 quadrature). Figure 3.17 shows the results for this case for both sets of smoothing parameters. The apparent orders of convergence decrease and are in better agreement for the two smoothing schemes.

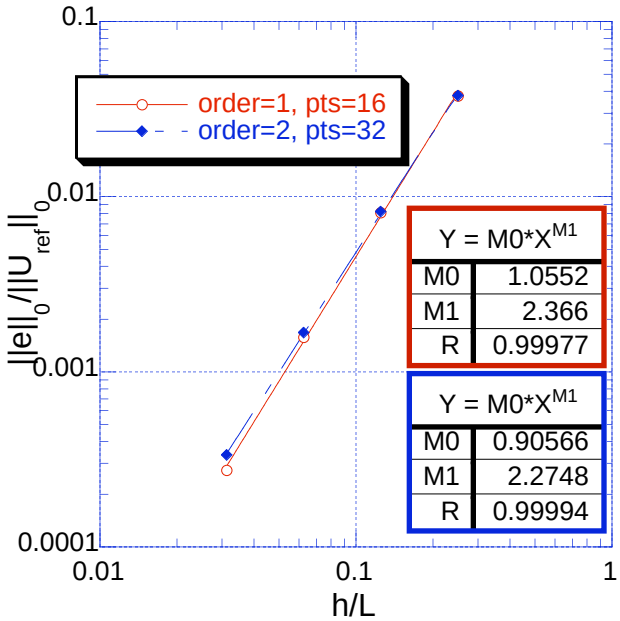

Figure 3.16. Relative errors vs. element size for bending problem with approximate reference solution, n=0.17, and 2x2 quadrature.

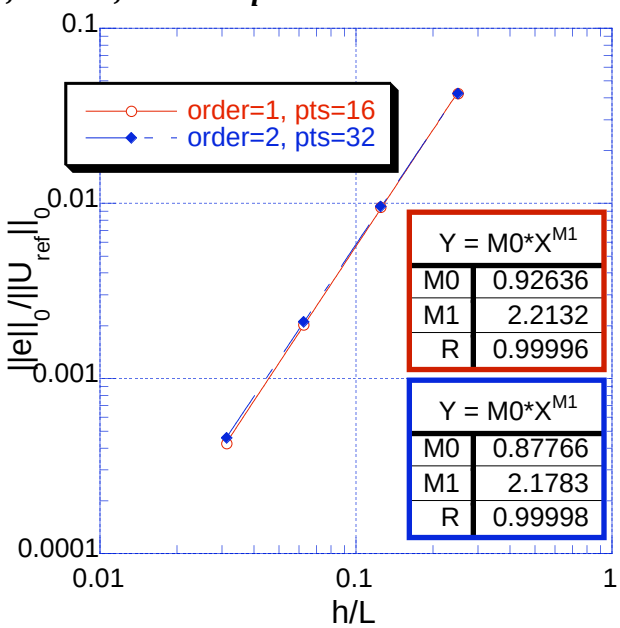

Figure 3.17. Relative errors vs. element size for bending problem with approximate reference solution, n=0.17, and 4x4 quadrature.

The reference solutions for the cracked case incorporated a column of interface elements through the center of the domain (x=0) *a priori*. The research code used in this study was defined to examine propagating cracks, not stationary cracks, so to examine each case the cohesive crack had to be forced to the center of the domain. The time at which the crack reaches the center for the reference solution, was the maximum time applied in the XFEM solutions. However, generally the state of the crack for the XFEM solution differed with that of the FEM solution. To address this a few different approaches were examined, the simplest of which was to make the criterion for propagation spatially dependent, requiring the principal stress to be

much higher than the tensile strength for $y>0$; this caused the crack to stall at the center of the domain as desired. Figure 3.18 shows the results for an isotropic domain in comparison to the uncracked bending results. Consider two observations: (1) for relative coarse meshes the relative errors are very similar with and without the crack, and (2) the apparent order of convergence for the XFEM is not optimum. The size of the cohesive zone is on the order of one element for the 5x5 mesh and yet the error in the displacement field is about 2%. The lack of optimum convergence rate was expected since the enrichment has not been adjusted for the transition from the FEM basis to the enriched basis – the so-called *blending region* problem. Solutions to this problem exist but have not been implemented, since I would prefer to first examine the effect of enriching a larger neighborhood; for the current analyses the approximate solution space of the coarser meshes is not contained in that of the finer meshes, since only nodes whose support are intersected are enriched. Thus for the current enrichment scheme, the region of enrichment shrinks with mesh refinement leading to "less and less use of the enrichment."

Only a very limited examination of the effect of deviating from isotropy was possible in this study, and it was limited to a single orthotropic material. A single material parameter, Young's modulus for the 1-material axis, was varied while the other elastic constants remained fixed. To illustrate the variation of accuracy with a deviation from isotropy, E_1 is perturbed by the sequence of factors {0.6, 0.8, 1.2, 1.4}. A 5x5 mesh is selected for the XFEM analyses because: (1) the initial emphasis of this work was upon trying to use relative coarse meshes and let enrichment "pick up the rest," (2) enrichment is then applied over a larger region, and (3) use of the approximate reference solution is more accurate for a coarser mesh. In the first set of analyses, the 1-material axis was defined to correspond to the 1-global axis. Figure 3.19 presents results for both primary (U) and secondary variables (∇U). Note that for the displacement field the relative error changes from about 2% to just over 3%, while the relative errors in ∇U change from about 10.5% to 12%. The fact that the errors for this coarse mesh are a minimum for the isotropic case reflect that this is the case the enrichment was derived for, and that it is apparently helpful in representing the field around the crack. On the other hand, the results indicate that applying the enrichment functions to problems that involve, at least weak anisotropy may still be beneficial. Analyses that have the 1-material axis rotated at 45 degrees relative to the 1-global axis have been undertaken, but convergence is lost in the reference solution before the crack reaches the center of the domain. Further examination of the problem is in progress. Admittedly this later problem is more contrived since the crack is still assumed to propagate vertically through the domain.

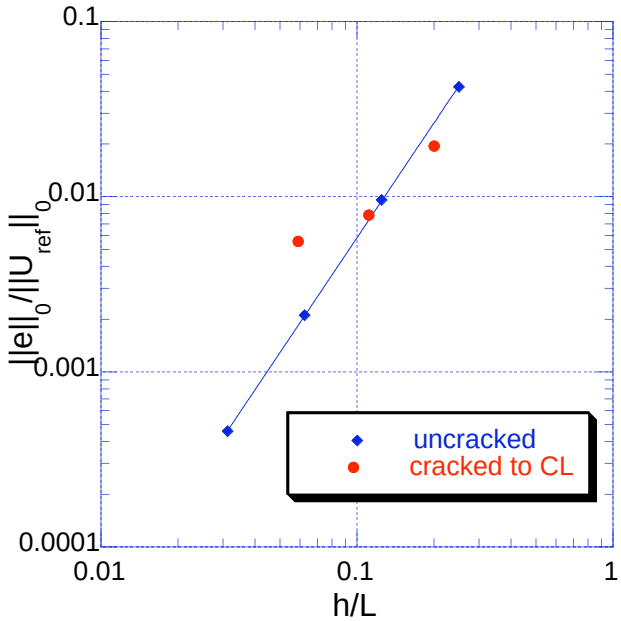

Figure 3.18. Relative errors vs. element size for bending problem, uncracked and cracked.

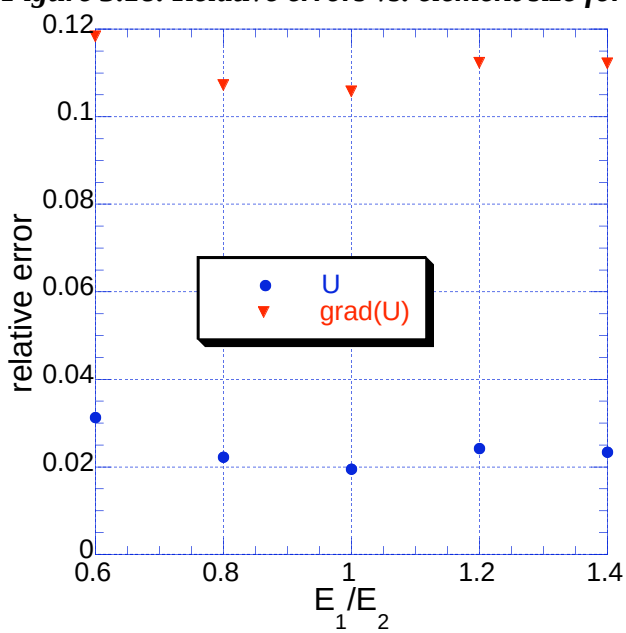

Figure 3.19. Relative error in U and ∇U vs. E_1/E_2, with E_1 varying (5x5 XFEM mesh).

3.3.5 Closure

The analytically enriched XFEM formulation advanced in this study is apparently one of only two published efforts at using analytically derived enrichment functions for the cohesive crack problem. Efforts to address (1) curved crack mapping, (2) "stress field smoothing" (also called "stress extraction"), and (3) stress relief for multiple cracks were successful and contributed to an earlier publication [35] that addressed propagation of curved cracks. To further evaluate the utility of the analytical enrichment and its limitations when the material is anisotropic, fields around a stationary crack were examined. The case of an isotropic material was examined first to verify the correctness of the norm calculations and to determine the

applicability of an approximate reference solution in measuring the error. Using an approximate reference solution yielded apparent rates of convergence that were on the order of 10-20% higher than the optimum value, but these reference solutions are still considered sufficient for examining field errors in XFEM analyses with relatively coarse meshes. Further study on the effect of neighborhood enrichment and specialized enrichment for the blending regions upon the accuracy of field predictions is merited since both have been shown to improve results for other analytical enrichments. A limited examination of the effect of anisotropy upon the accuracy of analyses (using the current enrichment) suggests that some problems with anisotropic material properties could benefit from the analytical enrichment; more extensive study is needed, as the current study did not examine the effect upon the calculated crack direction.

Section 3 References:

1. Harlow, F.H., *The Particle-in-Cell Computing Method for Fluid Dynamics in Fundamental Methods in Hydrodynamics*, in *Experimental Arithmetic, High-Speed Computations and Mathematics*, B. Alder, F. S., and M. Rotenberg, Editors. 1964, Academic Press. p. 319-345.
2. Brackbill, J.U. and H.M. Ruppel, *FLIP: A method for adaptively zoned, particle-in-cell calculations in two dimensions.* Journal of Computational Physics, 1986. **65**: p. 314-343.
3. Burgess, D., D.L. Sulsky, and J.U. Brackbill, *Mass matrix formulation of the FLIP particle-in-cell method.* Journal of Computational Physics, 1992. **103**: p. 1-15.
4. Sulsky, D.L., Z. Chen, and H.L. Schreyer, *A particle method for history-dependent materials.* Computer Methods in Applied Mechanics and Engineering, 1994. **118**: p. 179–196.
5. Sulsky, D.L. and H.L. Schreyer, *Axisymmetric Form of the Material Point Method with Applications to Upsetting and Taylor Impact Problems.* Computer Methods in Applied Mechanics and Engineering, 1996. **139**: p. 409-429.
6. Sulsky, D.L., S.J. Zhou, and H.L. Schreyer, *Application of a particle-in-cell method to solid mechanics.* Computer Physics Communications, 1995. **87**: p. 236–252.
7. Wieckowski, Z., *The material point method in large strain engineering problems.* Computer Methods in Applied Mechanics and Engineering, 2004. **193**(39-41): p. 4417–4438.
8. Love, E. and D.L. Sulsky, *An Energy Consistent Material-Point Method for Dynamic Finite Deformation Plasticity*, in *Technical Report HPC@UNM2005-001*. 2005: The Center for High Performance Computing, University of New Mexico, Albuquerque, NM.
9. Gadala, M.S., *Recent trends in ALE formulation and its applications in solid mechanics.* Computer Methods in Applied Mechanics and Engineering, 2004. **193**(39-41): p. 4247–4275.
10. Biffle, J.H., *A three-dimensional finite element computer program for the nonlinear quasi-static response of solids with the conjugate gradient method*, in *SAND Report*. 1987: Albuquerque, NM. p. SAND87-1305.
11. Flanagan, D.P. and T. Belytschko, *A uniform strain hexahedron and quadrilateral with orthogonal hourglass control.* International Journal for Numerical Methods in Engineering, 1981. **17**: p. 597-609.
12. Suresh, S., *Fatigue of Materials*. 2nd ed. 1998, New York: Cambridge University Press.

13. Dunne, F.P.E., A.J. Wilkinson, and R. Allen, *Experimental and computational studies of low cycle fatigue crack nucleation in a polycrystal.* International Journal of Plasticity, 2007. **23**: p. 273-295.
14. Kamaya, M., Y. Kawamura, and T. Kitamura, *Three-dimensional Local Stress Analysis on Grain Boundaries in Polycrystalline Material.* International Journal of Solids and Structures, 2007. **44**: p. 3267-3277.
15. Lewis, A.C., K.A. Jordan, and A.B. Geltmacher, *Determination of Critical Microstructural Features in an Austenitic Stainless Steel Using Image-Based Finite Element Modeling.* Metallurgical and Materials Transactions A, 2008. **39A**: p. 1109-1117.
16. Lewis, A.C., et al., *Quantitative Analysis and Feature Recognition in 3-D Microstructural Data Sets.* JOM, 2006(58): p. 52-56.
17. Bogy, D.B., *Two Edge-Bonded Elastic Wedges of Different Materials and Wedge Angles Under Surface Tractions.* Journal of Applied Mechanics, 1971. **38**: p. 377-386.
18. Bogy, D.B., *Stress Singularities at Interface Corners in Bonded Dissimilar Isotropic Elastic Materials.* International Journal of Solids and Structures, 1971. **7**: p. 993-1005.
19. Reedy, E.D., Jr. and T.R. Guess, *Comparison of Butt Tensile Strength Data with Interface Corner Stress Intensity Factor Prediction.* International Journal of Solids and Structures, 1993. **30**: p. 2929-2936.
20. Dunn, M.L., et al., *Fracture initiation at sharp notches under mode I, mode II, and mild mixed mode loading.* International Journal of Fracture, 1997. **84**: p. 367-381.
21. Chen, H.P., *Stress Singularities in Anisotropic Multi-Material Wedges and Junctions.* International Journal of Solids and Structures, 1998. **35**: p. 1057-1073.
22. Chue, C.H. and C.I. Liu, *A General Solution on Stress Singularities in an Anisotropic Wedge.* International Journal of Solids and Structures, 2001. **38**: p. 6889-6906.
23. Tvergaard, V. and J.W. Hutchinson, *Microcracking in Ceramics Induced by Thermal Expansion or Elastic Anisotropy.* Journal of The American Ceramic Society, 1988. **71**: p. 157-166.
24. Picu, R.C. and V. Gupta, *Singularities at Grain Triple Junctions in Two-Dimensional Polycrystals with Cubic and Orthotropic Grains.* Journal of Applied Mechanics, 1996. **63**: p. 295-300.
25. Ting, T.C.T., *Anisotropic Elasticity: Theory and Applications*. 1996: Oxford University Press.
26. Ting, T.C.T., *Explicit Solution and Invariance of the Singularities at an Interface Crack in Anisotropic Composites.* International Journal of Solids and Structures, 1986. **22**: p. 965-983.
27. Ting, T.C.T. and S.C. Chou, *Edge Singularities in Anisotropic Composites.* International Journal of Solids and Structures, 1981. **17**: p. 1057-1068.
28. Suwito, W., et al., *Elastic moduli, strength, and fracture initiation at sharp notches in etched single crystal silicon microstructures.* Journal of Applied Physics, 1999. **85**: p. 3519-3534.
29. Feron, M., Z. Zhang, and Z.G. Suo, *Split singularities and dislocation injection in strained silicon.* Journal of Applied Physics, 2007. **102**(2): p. Article number 023502.
30. Melenk, J.M. and I. Babuska, *The partition of unit finite element method: basic theory and applications.* Computer Methods in Applied Mechanics and Engineering, 2000. **129**: p. 289-314.

31. Belytschko, T.B. and T. Black, *Elastic crack growth in finite elements with minimal remeshing.* International Journal for Numerical Methods in Engineering, 1999. **45**: p. 601-620.
32. Karihaloo, B.L. and Q.Z. Xiao, *Modeling of stationary and growing cracks in FE framework without remeshing: a state-of-the-art review.* Computers and Structures, 2003. **81**: p. 119-129.
33. Sukumar, N., et al., *Extended finite element method for three-dimensional crac modeling.* International Journal for Numerical Methods in Engineering, 2000. **48**(11): p. 1549-1570.
34. Cox, J.V., *A partition of unity finite element method for cohesive crack modeling*. 2007, Sandia National Laboratories: Albuquerque, NM.
35. Cox, J.V., *An extended finite element method with analytical enrichment for cohesive crack modeling.* International Journal for Numerical Methods in Engineering, 2009. **78**: p. 48-83.
36. Xiao, Q.Z. and B.L. Karihaloo, *Improving the accuracy of XFEM crack tip fields using higher order quadrature and statically admissible stress recovery.* International Journal for Numerical Methods in Engineering, 2006. **66**: p. 1378-1410.
37. Hong, S. and K. K.S., *Extraction of cohesive zone laws from elastic far fields of a cohesive crack tip: a field projection method.* Journal of the Mechanics and Physcs of Solids, 2003. **51**: p. 1267-1286.
38. Zhang, W. and X. Deng, *Mixed-mode I/II fields around a crack with a cohesive zone ahead of the crack tip.* Mechanics Research Communications, 2007. **34**(2): p. 172-180.
39. Bazant, Z.P. and J. Planas, *Fracture and Size Effect*, in *Concrete and Other Quasibrittle Materials*. 1998, CRC Press.
40. Bazant, Z.P. and G. Pijaudier-Cabot, *Nonlocal continuum damage, localization, instability, and convergence".* ASME Journal of Applied Mechanics, 1988. **55**: p. 287-293.

This page left intentionally blank.

This page left intentionally blank.

4. APPLICATIONS.

4.1. Cyclic plasticity applied to nickel microstructures. (R.P.M. Dingreville (01814), C.C. Battaile (01814), L.N. Brewer (01814), and B.L. Boyce (01813))

This section assesses the sensitivity of cyclic plasticity to microstructure morphology by examining and comparing the microplastic ratcheting behavior (cycle-dependent accumulation of plastic strain) of different idealized microstructures (square, hexagonal, tessellated, and digitized from experimental data). Whereas ratcheting is typically thought of as a continuum phenomenon [1-13], the present study investigates the possible microstructural origins of microplastic ratcheting (purely tensile cyclic loading where $R > 0$) and proposes a combination of experiments and FEM simulations for predicting microstructural plasticity and evaluating its sensitivity to the microstructure to answer the following question: *"how detailed of a microstructural representation is necessary to capture micro-plastic ratcheting?"* In other words, we are interested in assessing the effect of the description of the microstructure on the simulation of micro-plastic ratcheting. A number of key physical characteristics are taken into account in the modeling and simulations to accurately represent the onset and development of microplastic ratcheting. As illustrated in Figure 4.1, we use a coupling between microstructural characterization, mechanical testing and numerical simulations to compare experimental and numerical results at both macroscopic and microscopic level. While the present study considers one isolated problem in cyclic plasticity (purely tensile microplastic ratcheting), the approach could be extended to address other cyclic plasticity issues, such as microstructural crack initiation and small crack growth [14] or cyclic evolution of residual stresses [15].

The computational model explicitly addresses the effects of microstructure by including realistic topological information (grain morphology, topology and crystallography) taken from EBSD data. The physics of deformation of the face centered cubic (FCC) polycrystal are incorporated through a classical crystal plasticity formulation that explicitly considers the different dislocation slip systems, and the elasto-plastic crystallographic anisotropies at the grain level. A computer-generated, representative microstructure is used to calibrate the crystal plasticity parameters to the experimental data.

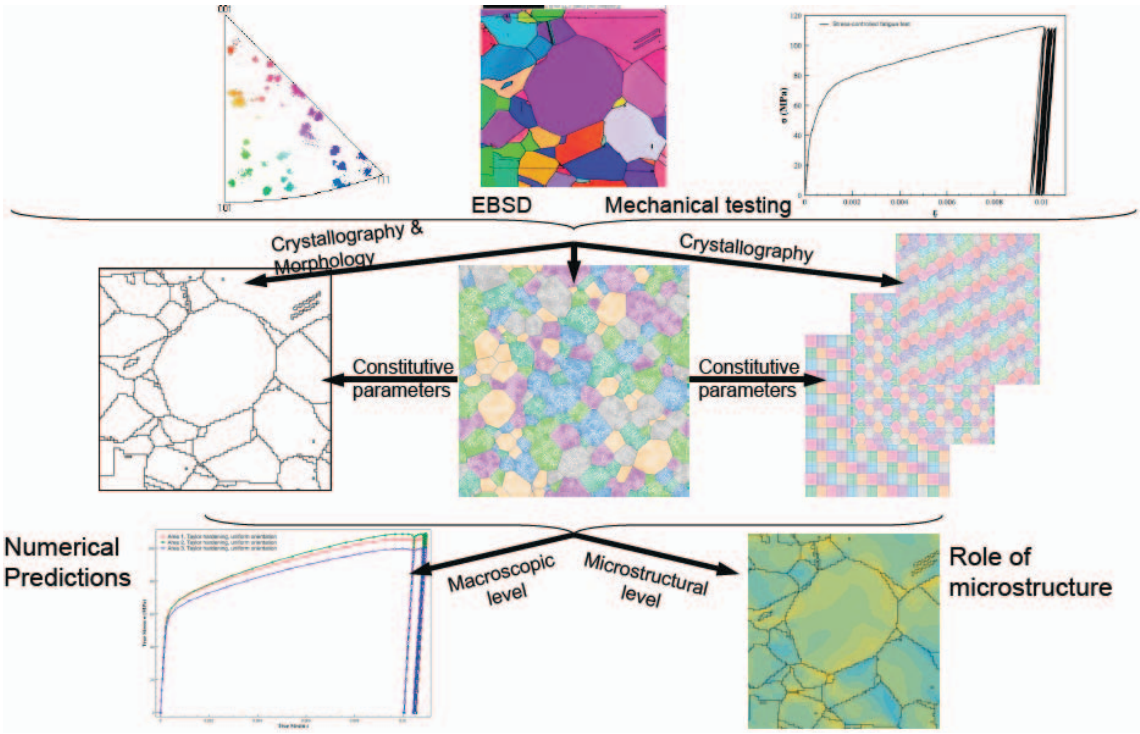

Figure 4.1. Methodology for coupling microstructure characterization, mechanical testing and numerical simulations.

4.1.1 Methods for coupling experiments and simulations

Finite element implementation

To examine microplastic ratcheting at the microstructural level, the material deformation was treated with a crystal plasticity rate-dependent formulation [16]. This crystal plasticity model was incorporated into Sandia's finite element analysis code, JAS3D [17] as a standard subroutine. The simulations use eight node (hexahedral) 3D isoparametric elements with a single integration point at the element centroid. To deal with zero energy modes that may arise as a result of the single point integration scheme, the code uses an hourglass control, based on the work of Flanagan and Belytschko [18]. Numerical integration of the constitutive model is performed using a forward Euler scheme. Restrictions are placed on the time step to ensure that the forward integration scheme remains stable. If the step size requested by the user is larger than the allowable size, the step is divided into subincrements of allowable size within the constitutive subroutine.

Parameters for the constitutive models were calibrated using a representative microstructure that is meant to approximate the actual specimen's microstructure to not only provide a larger population of grains than provided by the experimental data, but also to overcome the artifacts generated by the pixelization of the grain boundaries induced by the EBSD-generated microstructure. This representative microstructure, illustrated in Figure 4.3(a), was obtained by means of a two-dimensional Potts model of grain growth [19] with an imposed periodicity constraint at the boundaries of the polycrystalline mesh. The grain growth simulation used to generate the representative microstructure employed the Monte Carlo Potts model to

simulate ideal normal grain growth with isotropic grain boundary energy and mobility. Hereafter, this 199-grain fictitious polycrystal is designated as the representative microstructure. The representative microstructure consists of 35873 elements, extends only a single element into the third dimension (perpendicular to the plane in Figure 4.3(a)) and contains linear (as opposed to stepped) grain boundaries. Periodic boundary conditions were applied in all directions, which is equivalent to simulating a columnar microstructure of infinite extent in all directions.

The crystallographic orientations assigned to each grain of the representative microstructure were assigned from orientation distribution functions generated from the EBSD experimental data. For every pixel in the experimental digitized images from each of the three areas of interest, a set of three Euler angles $\left(\varphi_1, \Phi, \varphi_2\ ,\ 0 \le \varphi_1 < 360^\circ,\ 0 \le \Phi < 90^\circ,\ 0 \le \varphi_2 < 90^\circ \text{ for a crystal with cubic symmetry}\right)$ were generated from the EBSD measurements. A cumulative probability density function $F_\theta(x)$ was then defined from this experimental dataset for each Euler angle such that,

$$\begin{cases} x \rightarrow F_\theta(x) = P(\theta \le x) = \sum_{x_i \le x} p(x_i) \\ p(x_i) = \dfrac{N_i}{N} \end{cases}, \qquad (4.10)$$

where N_i is the total number of pixels having an orientation ranging from θ_i to $\theta_i + \Delta\theta$, N is the total number of data points, and $p(x_i)$ is the probability of observing an orientation θ in the angular interval θ_i to $\theta_i + \Delta\theta$. Subsequently, 199 sets of Euler angles were randomly generated and chosen from the experimental cumulative probability functions $F_\theta(x)$ and assigned to each grain of the representative microstructure. Equivalent orientations based on crystal symmetry have been used to assure that the desired orientation distribution was actually imposed. To guarantee this artificial polycrystal was the closest representation of the actual experimental polycrystal, 100 different random orientation sets (each one of them containing 199 sets of three Euler angles) were generated. Each orientation set was then deformed to 1% elongation with the Taylor model resulting in 100 stress-strain responses. The average response of these 100 different stress-strain curves was subsequently determined. As shown in Figure 4.3(b) the simulated stress-strain response obtained from the average orientation distributions agrees well with the experimental data. The orientation set giving the stress-strain response closest to this average behavior was chosen as the representative orientation set and, although not shown here, the deviations between the 100 different stress-strain curves are relatively small. Consequently, the representative microstructure coupled with the chosen orientation set was considered as statistically representative of the macroscopic experimental tensile specimen. This constitutes a valid assumption

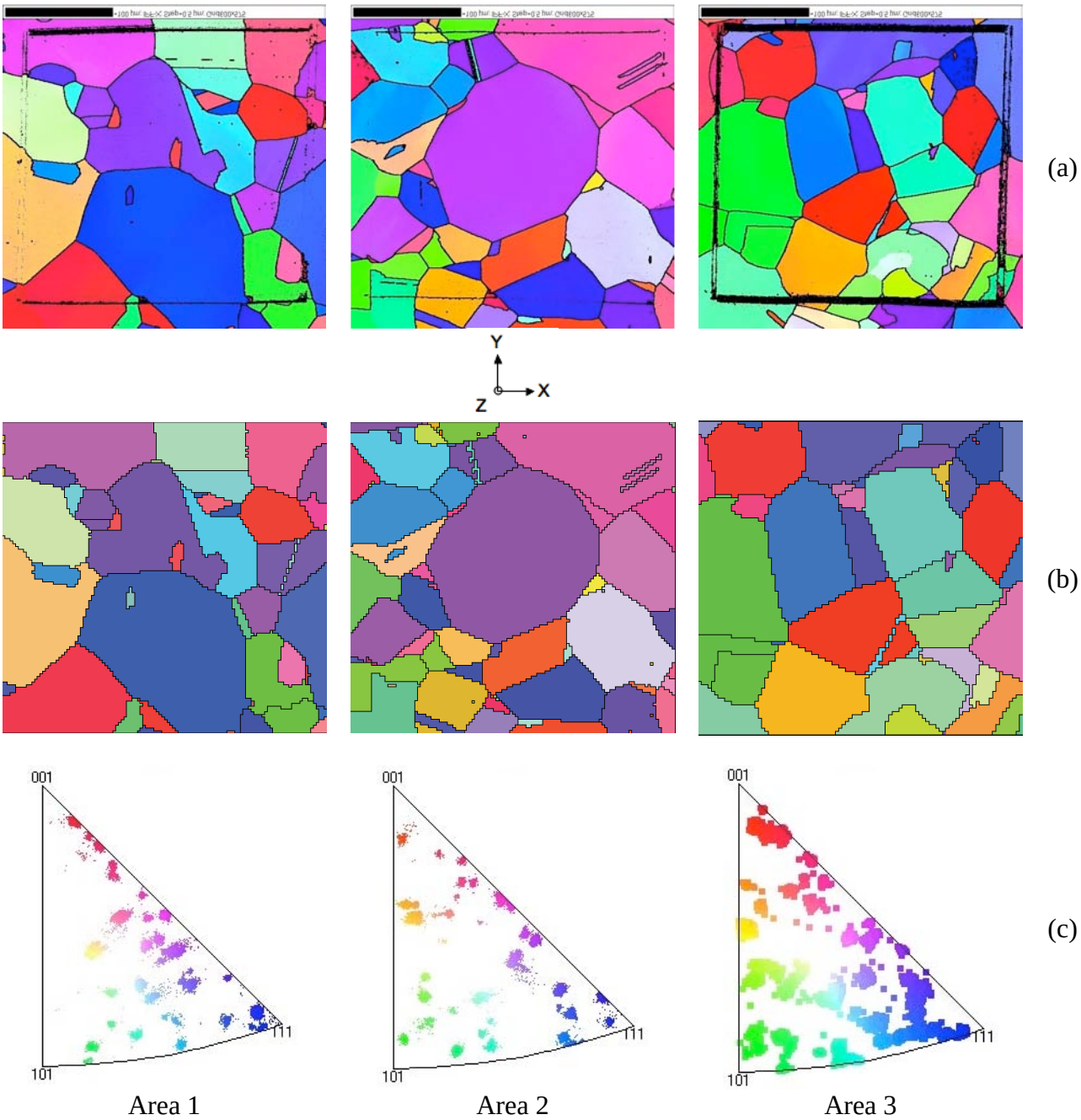

Figure 4.2. Microstructure of the areas of interest (a) revealed by EBSD measurements and (b) digitized for the numerical simulations. (c) The Inverse Pole Figures (IPFs) represent the raw grain orientations measured by EBSD with respect to the loading axis. The colors of the IPFs correspond directly to the colors of the grains.

given the fact that the experimental data is sparse and the microstructure appears to have a random texture. Furthermore, it should be noted that because this work is using a local model (i.e the length scale of the microstructure is implicitly accounted for in the materials fitting parameters), the effect of the grain size distribution is not primary. Therefore, correspondence

between the modeled and experimental grain size distributions is not a concern in the present work.

The representative microstructure with the chosen orientations was used to calibrate the material parameters to the macroscopic experimental response. These parameters include two flow parameters $(m, \dot{\gamma}_0)$, five hardening parameters $(\tau_0, H_1, H_2, \lambda, b)$ for three different hardening laws (only the first three are defined for the power and Voce hardening laws), and one threshold parameter $\bar{\alpha}$. The flow parameters and the hardening parameters were initially fitted analytically and then adjusted to the experimental tensile test to further agreement at 1% deformation (prior to any stress-controlled cycling or first unloading phase), while the threshold parameter was evaluated from the experimental cyclic response and its ratcheting behavior. Results are shown in Figure 4.3(b).

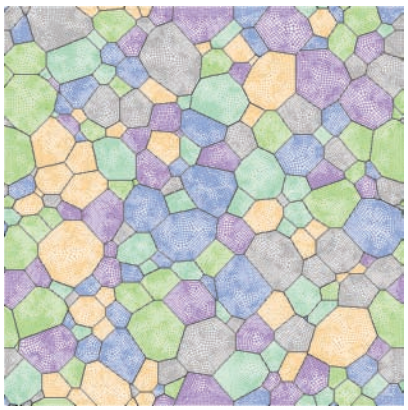

(a)

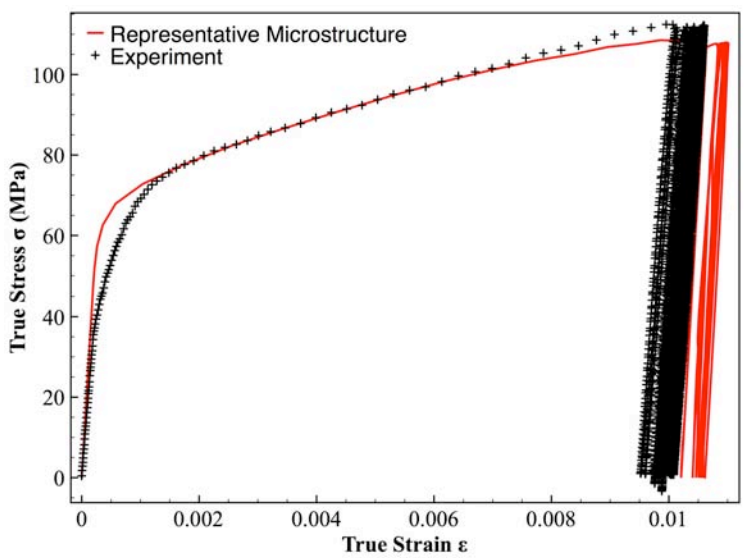

(b)

Figure 4.3. (a) Representative microstructure composed of 199 grains with periodicity constraints on the edges. (b) Stress vs strain from experiment (black symbols), and from a simulation using best-fit constitutive parameters and grain orientations on the microstructure in (a).

Tables 4.1 and 4.2 list the parameters used for the different constitutive models employed in this study. Note that the different sets of hardening parameters used in this work are characteristic of the average grain size of the experimental samples.

Table 4.1 Elastic and viscoplastic parameters

C_{11} (GPa)	C_{12} (GPa)	C_{44} (GPa)	m	$\dot{\gamma}_0$ (1/s)	$\bar{\alpha}$
246.5	147.3	124.7	0.04	1	0.832

Table 4.2 Hardening parameters

	Power law hardening	**Voce hardening**	**Taylor hardening**
τ_0	76.0* (MPa)	76.0* (MPa)	24.84 (MPa)
H_1	2314 (MPa)	398 (MPa)	4.906 (10^8/m)
H_2	0.8768	4298 (MPa)	26.65
λ	-	-	0.5
b	-	-	2.517 (Å)
M	3.06	3.06	-

* Note that the initial slip resistance τ_0 is weighed by the Taylor factor M

IV.a.1.3 Initial microstructure and boundary conditions

The deformation behavior of the nickel polycrystalline specimen under cyclic uniaxial tension was studied using the crystal plasticity model for comparison against experimental results. The three EBSD-generated microstructures were represented by meshes of square, hexahedral, three-dimensional, isoparametric elements. These meshes consisting of $120 \times 115 \times 1$ elements representing 36 grains for the first area of interest (Area 1), $120 \times 115 \times 1$ elements representing 45 grains for second area of interest (Area 2) and $97 \times 94 \times 1$ elements representing 35 grains for the third area of interest (Area 3). As shown in Figure 4.4, the mesh is superimposed onto the microstructure, and grain orientations obtained from the EBSD texture analysis are assigned to the corresponding elements. Note that the square grid used in both the EBSD and finite element representations, necessitates that most grain boundaries contain right-angle segments to conform to the topology of the grid. However, during the course of this study, it was found that mesh refinement did not substantially alter the results of the macroscopic ratcheting response and consequently the analysis was carried out with the coarser mesh.

Even in a pure, nominally undeformed metal, the crystallographic data collected by EBSD is not uniform within a single grain. This is due to several factors, including random error associated with the measurement itself and any significant lattice imperfections present in the

material. On one hand, the nickel material used in this study is not expected to contain any significant deformation. On the other, it is not straightforward to ascertain the specific source of crystallographic inhomogeneity in practice (e.g. “noise” in experimental measurements or real local misorientation). Therefore, we will consider two treatments for each EBSD data set: one in which all intragranular crystallographic inhomogeneity is assumed to be important (i.e., “raw” orientations), and another in which the orientation of each grain is assigned as the average value from the EBSD data within the grain (i.e., averaged orientations). The orientation maps of the three area of interest are shown in Figure 4.2(c) in the case of the raw orientation.

To simulate the loading conditions of the experiments, a triangular waveform uniform traction was applied on both X faces of the reconstructed microstructures, while the Y faces were constrained to remain planar and parallel. The applied traction was chosen for each area of interest in order to attain 1% deformation after the first tensile cycle, as in the experiments. Periodic boundary conditions were applied to the front and the back faces equivalent to simulating a columnar microstructure. Note that the EBSD data, and therefore the simulated microstructures, represent only a small fraction of the test specimen. The real microstructures extend well beyond the boundaries of the regions considered in this study, and this surrounding material undoubtedly imposes non-uniform boundary conditions unlike those used here. It is obvious that the present boundary conditions are constraining and affecting the mechanical behavior of some of the grains near these boundaries. This issue will be addressed in a subsequent publication [20]. In this paper, we therefore neglect grains close to the edges of the computational domains.

4.1.2 Cyclic ratcheting

Numerical simulations vs. experiments

The comparisons of the experimental data to the representative microstructure and the predicted cyclic stress-strain responses for the three areas of interest are illustrated in Figure 4.4 in the case of the Taylor hardening model with average grain orientation. The microstructure-based approach adopted in this work provides good prediction of the microplastic ratcheting response. The cyclic behavior of the representative microstructure and the three digitized microstructures agrees well with the experimental results. The three digitized microstructures exhibit a similar cycle-dependent accumulation of plastic strain at a similar rate. The differences between the three different areas and the experiment mainly stem from the small population of grains in each area, the effect of the local texture (the three digitized microstructures are softer than the representative microstructure) and the nature of the microstructural representation (square elements for the digitized microstructures as opposed to paved elements for the representative microstructure). As a consequence of the aforementioned discrepancies, the microplastic ratcheting for the digitized microstructures occurs mainly in the first three cycles while it occurs across five or six cycles in the case of the representative microstructure and the experiments.

In all cases, both experimental and computational, two different stages can be observed in terms of strain accumulation and ratcheting rate. The first stage consists of a rapid accumulation

of the plastic strain for the first few cycles, while the second stage exhibits a steady state where the accumulation of plastic strain is very small after each cycle. Both stages are illustrated in Figure 4.5, where only equivalent plastic deformations greater than 1% are shown. In the first stage of ratcheting, the material hardens rapidly and pockets of plastic deformation form in grains with preferred orientations. In the second stage, where ratcheting stabilizes, the cyclic hardening is very small after each cycle resulting in a slowly dissipating (approximately constant) ratcheting rate.

The EBSD technique is capable of providing information about deformation-induced crystallographic reorientation with subgrain resolution, which is a subset of the information available from our computational approach. However, just as the accumulation of plastic strain saturates after only a very few cycles in Figure 4.4(b), the evolution of subgrain-scale deformation beyond the first cycle is not significant relative to the measurement uncertainty (approximately 0.5° local misorientation). Therefore, while the agreement between the ratcheting simulations and experimental response is good at the macroscopic level, a comparison between simulation and experiment at a subgrain level does not provide additional benefit to the present analysis. Nonetheless, it should be noted that these simulations explicitly consider the microstructure morphology and micromechanical evolution, and therefore produce more accurate representations of the microstructure's response than continuum based models such as the Armstrong-Frederick kinematic hardening law or earlier FEM studies [21, 22].

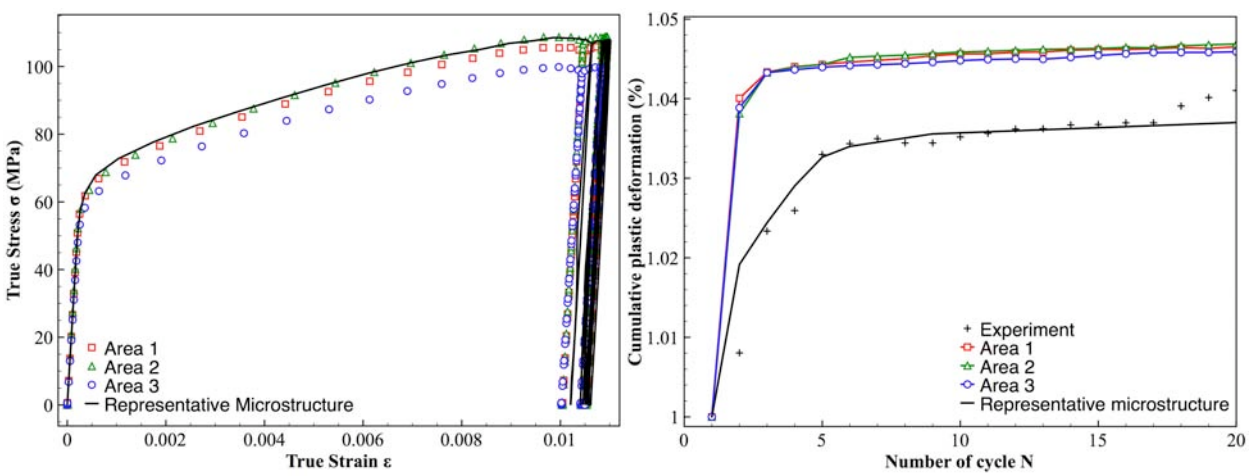

Figure 4.4 Comparison for (a., left) the representative microstructure and simulated stress-strain responses for stress-controlled cyclic tests, (b., right) the accumulation of plastic deformation as a function of the cyclic history. The anisotropic Taylor hardening model, with averaged orientations per grain, was used in this set of simulations. The different areas are labeled in Figure 2.

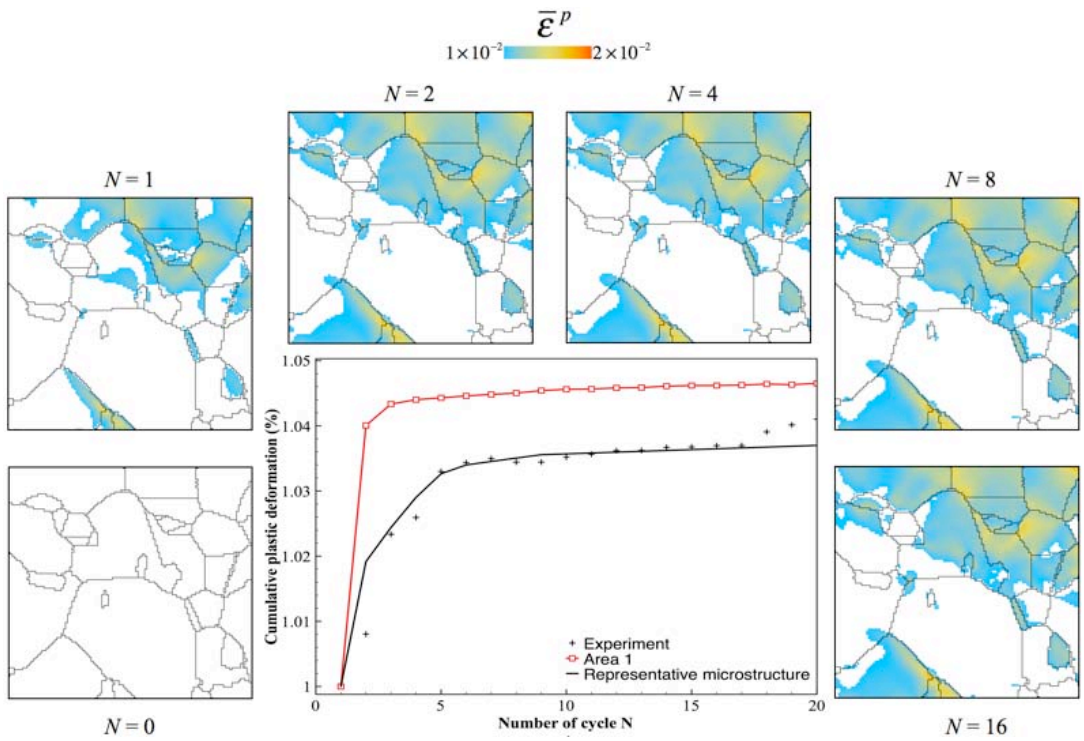

Figure 4.5 Illustration of the two stages of ratcheting. Equivalent plastic deformations higher than 1×10^{-2} ***are plotted for Area 1 (i.e no coloring corresponds to plastic strain lower than this threshold) in the case of the Taylor hardening model with averaged orientation per grain. Note that the regions close to the edges of the simulation box presented in Figure 4.(b) have been omitted. Area 1 is labeled in Figure 2.***

Effect of microstructure representation

The effort dedicated to a realistic and detailed description of the microstructure in numerical simulations is important as morphology/microstructure representation can have a significant influence on the mechanical response. The difference in the microplastic ratcheting behavior between the three different areas presented in the previous section suggests the sensitivity of cyclic plasticity to the details of the microstructure.

To have a better assessment of this sensitivity and to ascertain the level of microstructural detail required to adequately capture ratcheting behavior both at the macroscopic and microscopic scales, we considered several different idealized microstructures that follow a natural "microstructural evolution" towards the representative microstructure and compare their behavior to the representative microstructure and the three digitized areas. As illustrated in Figure 4.6, this progression starts from a microstructure with square grains comprised of one element each (Figure 4.6 (a)), to square grains with a 100 elements per grain (Figure 4,6 (b)), to a regular array of hexagonal grains containing several elements each (Figure 4.6 (c)), to a microstructure of distorted hexagonal grains containing several elements each (Figure 4.6 (d)). The distorted hexagonal microstructure was obtained by randomly displacing the corners of the hexagonal grains by a small amount (less than 15% displacements relative to the regular hexagonal grains). These idealized geometries allow for periodic boundary conditions to be

applied in all directions. For the square grains with 100 elements per grain, and the hexagonal grains, the crystallographic orientations assigned to each grain were obtained through the same procedure used in the case of the representative microstructure presented in section IV.a.1.1.2. The orientations for the square grains with one element per were the same as for the square grains with 100 elements per, while the orientations for the distorted hexagonal microstructure were the same as for the regular hexagonal grain microstructure. Additionally to these four microstructures, we also considered a "shuffled" digitized microstructure (Figure 4.6 (f)). We used the Fisher-Yates shuffling algorithm [23] to randomly permute the orientation set of three Euler angles between elements of one of the digitized microstructures (Area 1), i.e. the shuffled digitized microstructure consists of a same square mesh with the same population of elements and orientation set as the digitized microstructure except that the grain topology is lost in the permutation process. The Taylor hardening model was chosen to describe the evolution of the overall resistance to slip τ^{α}_{CRSS}, while the orientation per grain is assumed to be uniform.

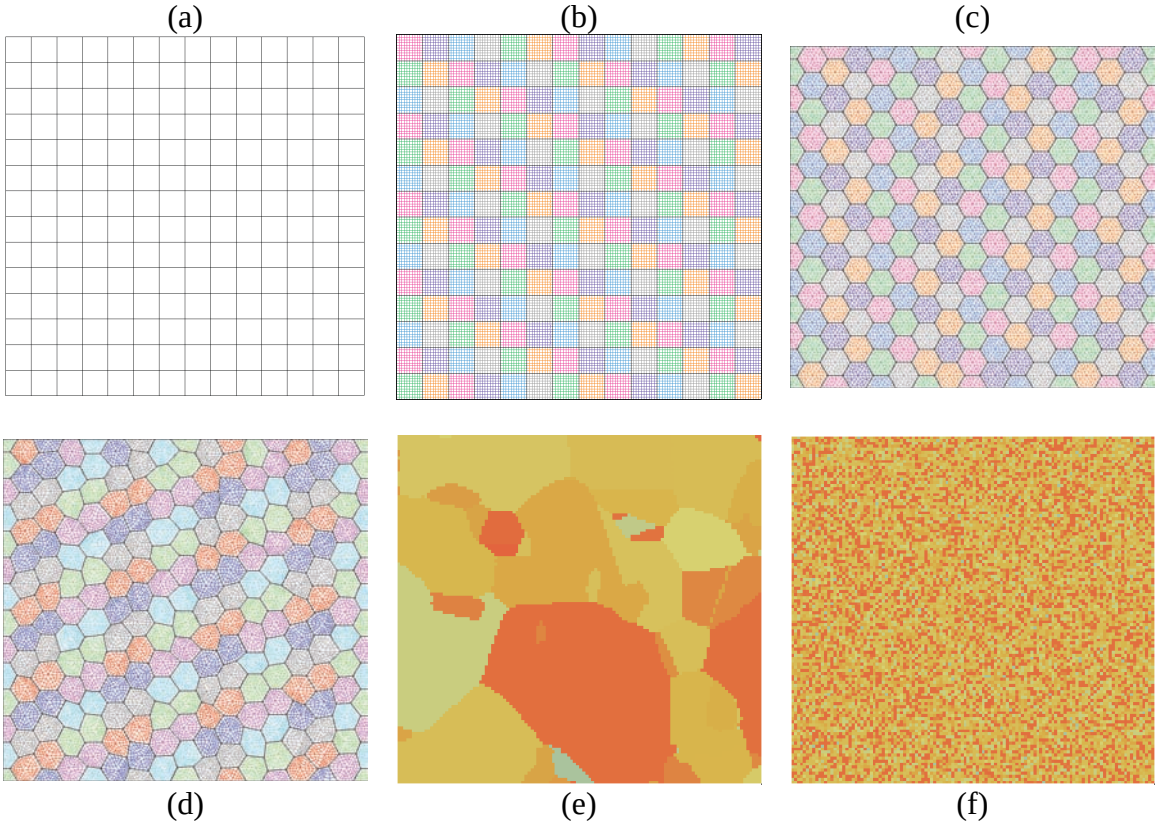

Figure 4.6 Different idealized microstructure morphologies used to assess the influence of the microstructure on ratcheting: (a) square microstructure with one element per grain, (b) square microstructure with 100 elements per grains, (c) regular hexagonal microstructure, (d) distorted hexagonal microstructure, (e) digitized microstructure (Area 1), and (f) shuffled digitized microstructure (Area 1). Colors are assigned randomly and do not correspond to any properties. Area 1 is labeled in Figure 2.

The comparison between the macroscopic ratcheting behaviors of the different idealized microstructures is illustrated in Figure 4.7. The microstructural effects of the grain morphology do not bring any substantial improvement to the numerical predictions of ratcheting. The idealized microstructures give roughly the same amount of ratcheting as the digitized microstructures but deviate from the representative microstructure. This is partly due to the fact that the digitized microstructure possesses jagged right angle grain boundaries, which provides the same effect as the square microstructure. In terms of ratcheting rates, the differences between the very simple representations of the microstructure and the digitized microstructures are smaller than the differences they have with the experiment/representative microstructure. From a continuum point of view, as long as the orientation distribution is reasonable, adding microstructural details slows down the simulations but does not significantly improve macroscopic predictions over phenomenological models.

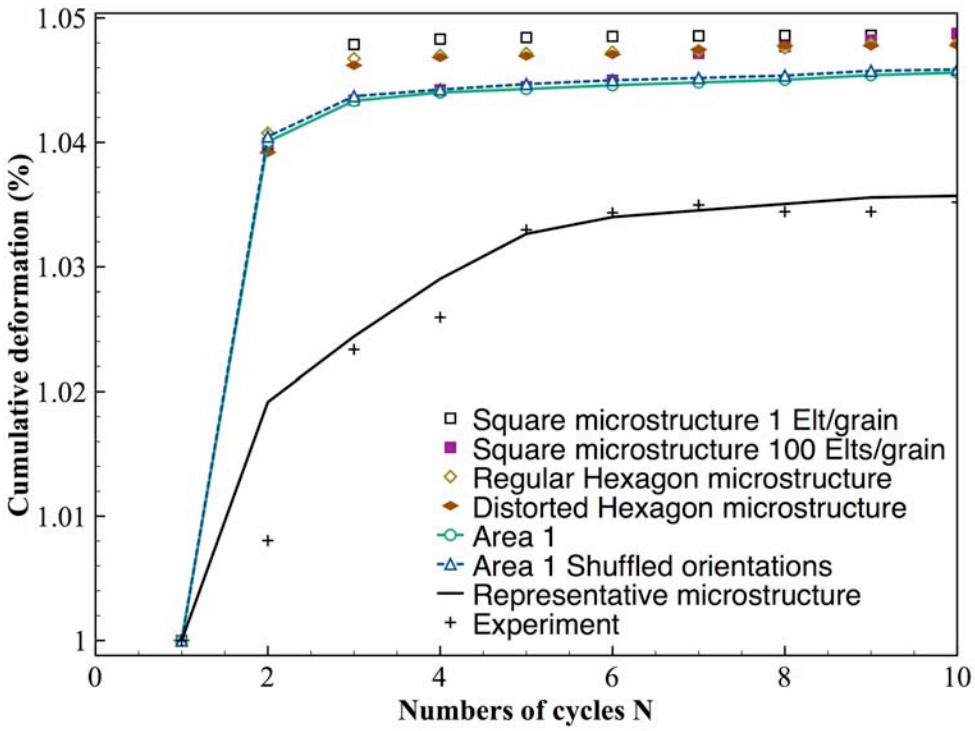

Figure 4.7. Effect of microstructure on the accumulation of plastic deformation as a function of the cyclic history. The anisotropic Taylor hardening model was used in this set of simulations. Area 1 is labeled in Figure 2.

Despite the apparent similarity in ratcheting response at the macroscale, significant differences in the microscale distribution of plasticity were observed for the different microstructural representations. To illustrate these differences, a simple pointwise (local) crack nucleation model is used as a common metric at the microstructural level (microscopic scale) to evaluate the sensitivity of the cyclic behavior to the microstructure. Based on a slowly

dissipating accumulation of plastic deformation (assumed linear for simplicity), this crack nucleation model depends on the magnitude of the plastic strain at the microstructural level. In this model, a crack is considered to nucleate when a critical maximum equivalent plastic deformation $\varepsilon_{nucleation}$ is locally attained [24] such that,

$$N_{nucleation} = N_0 + \frac{\left(\varepsilon_{nucleation} - \bar{\varepsilon}_0^{p,\max}\right)}{\left[\dfrac{\partial \bar{\varepsilon}_0^{p,\max}}{\partial N}\right]_{N_0}} \quad , \tag{4.2}$$

where N_0 is the number of cycles for ratcheting to stabilize, $\bar{\varepsilon}_0^{p,\max}$ is the maximum effective plastic strain reached during the N_0^{th} cycle , and $\left[\dfrac{\partial \bar{\varepsilon}_0^{p,\max}}{\partial N}\right]_{N_0}$ is the rate of maximum effective plastic strain after N_0 cycles. The nucleation strain $\varepsilon_{nucleation}$ is assumed to be independent of the morphology considered and was arbitrarily chosen to be $\varepsilon_{nucleation} = 0.1$.

Table 4.3 presents the crack nucleation predictions for the different idealized microstructures. As expected, a notable difference can be observed between the different cases. The square microstructure with one element per grain tends to under predict both the magnitude and rate of increase of the local maximum plastic strain, and therefore over predicts the number of cycles to crack nucleation. As the microstructural morphology becomes more complex and the mesh more refined, more localized plastic deformation occurs in the microstructure, thereby lowering the predicted number of cycles to crack nucleation. By increasingly adding details to the microstructure, one starts gradually resolving localized phenomena such as inhomogeneous deformation. It is interesting to note that both the representative microstructure and the digitized microstructures predict local maximum equivalent plastic strains of the same order of magnitude. Furthermore, despite the small population of grains and the disparity in grain morphology, the three different digitized microstructures show similar nucleation predictions.

Even though the description of the microstructure has a weak influence on the macroscopic prediction of ratcheting, the grain morphology strongly impacts the behavior at the microscopic scale. The level of detail necessary to describe a microstructure is therefore closely related to the scale and phenomenon of interest. From a continuum perspective idealized microstructures might be sufficient to describe the cyclic behavior of a polycrystalline material. However, to adequately describe microscopic mechanisms such as crack nucleation, a more faithful depiction of the microstructure might be necessary.

Table 4.3 Crack nucleation predictions for different microstructure morphology

Microstructure morphology	N_0	$\bar{\varepsilon}_0^{p,\max}$	$\left[\frac{\partial \bar{\varepsilon}_0^{p,\max}}{\partial N}\right]_{N_0}$	$N_{nucleation}$
Square grain (1 element / grain)	6	1.3662×10^{-2}	9.70×10^{-7}	89057
Square grain (100 elements / grain)	6	1.7680×10^{-2}	3.30×10^{-6}	24951
Regular hexagonal grain	6	1.7592×10^{-2}	1.73×10^{-6}	47640
Distorted hexagonal grain	6	1.7819×10^{-2}	1.78×10^{-6}	46175
Representative microstructure	6	1.9446×10^{-2}	8.77×10^{-6}	9191
Shuffled digitized microstructure (Area1)	6	1.8782×10^{-2}	1.48×10^{-6}	54840
Area 1	6	2.1897×10^{-2}	3.21×10^{-6}	24337
Area 2	6	2.2226×10^{-2}	4.74×10^{-6}	16418
Area 3	6	2.0622×10^{-2}	3.77×10^{-6}	21054

4.1.3 Limitations of the present approach

Although the procedure presented here provides good predictions of the ratcheting behavior and an assessment of sensitivity to the microstructure description, several factors should be kept in mind when comparing experimental results to the numerical simulations.

First of all, the simulated stress-strain responses soften slightly as the mesh refinement is increased since the number of degrees of freedom within each grain is also increased. This is a direct consequence of the lack of length scale in the physical models. No mechanism exists within the present framework to define a microstructural length scale. A non-local crystal plasticity formulation would provide a better resolution of the texture evolution, and localization and distribution of stresses and strains, at the microstructural level. Incorporating a length scale would intensify the role of the microstructure's morphology on microplastic ratcheting.

As previously mentioned, due to the limited microstructural information obtained from EBSD measurements, the FE model does not extend beyond the areas of interest studied here and consequently the boundary conditions applied to simulate the uniaxial cyclic deformation of these regions do not properly account for the surrounding microstructure. This constraint can induce local errors [20] in the predictions of the behavior of the grains close to the edges of the mesh.

A related issue concerns the influence of the underlying microstructure on the surface fields since deformation mechanisms activated in each grain are three-dimensional. The microstructure below the surface cannot be determined with the experimental procedures used in this work. Experiments combining focused ion-beam and electron back scattered diffraction may be able to tackle this issue by their ability to map in three dimensions the grain shape, grain size and crystallography within a microstructure.

4.2. Inclusion of microstructure to small crack growth in hydrogen embrittlement problems

We often speak of fatigue crack growth and environmental effects as separable. Experimental findings, however, indicate that the environment can measurably affect small crack behavior. In fact, in some alloys, Stage I growth can be suppressed in vacuum [25]. Details of the material system and its susceptibility to a particular environment become increasingly important. In fact, it is this confluence of the environment and the microstructure that makes predicting fatigue crack initiation and propagation difficult and, consequently, empirical.

In an effort to narrow the focus and introduce microstructure as a simplifying assumption, we consider hydrogen embrittlement. This focus has relevance to our mission in gas transfer systems (GTS) and materials selection for the hydrogen economy. Specifically, we intend to focus on the pertinent mechanical and concentration fields ahead of crack tip in an infinite medium. In this small example, we will briefly review the hydrogen transport equation and a segregated coupling methodology employing Aria and Adagio. An examination of the mechanical fields will provide the motivation for incorporating idealized microstructure. Finally, we compare fields of total hydrogen concentration and make remarks on the processes of embrittlement.

4.2.1 Hydrogen transport and coupling methodology.

The derivation for hydrogen transport is taken from Sofronis [26]and Krom [27]. For brevity we will only introduce the needed information to justify the current coupling. We propose that hydrogen resides on lattice sites (having concentration C_L) and at trap sites (having concentration C_T). Although one can assume multiple trap sites, we will first just focus on dislocations as the dominant (and evolving) trapping mechanism. We note that empirical relations have expressed the number of trap sites N_T in terms of the equivalent plastic strain e_p [28]. We can then write a conservation law for the total hydrogen concentration ($C_T = C_L + C_T$) and propose a constitutive model for the flux through the boundary $\mathbf{J}_L$ that is derived from a chemical potential m_L. A key assumption of Oriani [29]assumes a local equilibrium between lattice and trap sites and enables one to write $C_T = C_T(C_L)$. One can now write a nonlinear partial differential equation governing the transport of hydrogen in terms of material constants and variables C_L, S_H, and e_p, where S_H is the hydrostatic stress derived from the 2nd Piola-Kirchoff stress. An outline of the derivation is presented in Figure 4.8. For completeness, we state that M_L is the lattice mobility, V_H is the partial molar volume, T is the temperature, R is the universal gas constant, and $\mathbf{D}_L$ is the diffusivity tensor.

In addition, Figure 4.8 also illustrates the segregated scheme between the quasi-static code Adagio and the transient transport code Aria. Currently, the constitutive model is independent of the concentration but future work will incorporate lattice dilation and the impact of hydrogen on the yield stress and hardening behavior. We should also note that the equivalent plastic strain is not a good representation of the dislocation density and the number of trap sites N_T. Future work will link better representations such as the isotropic hardening variable to the evolution of trap sites.

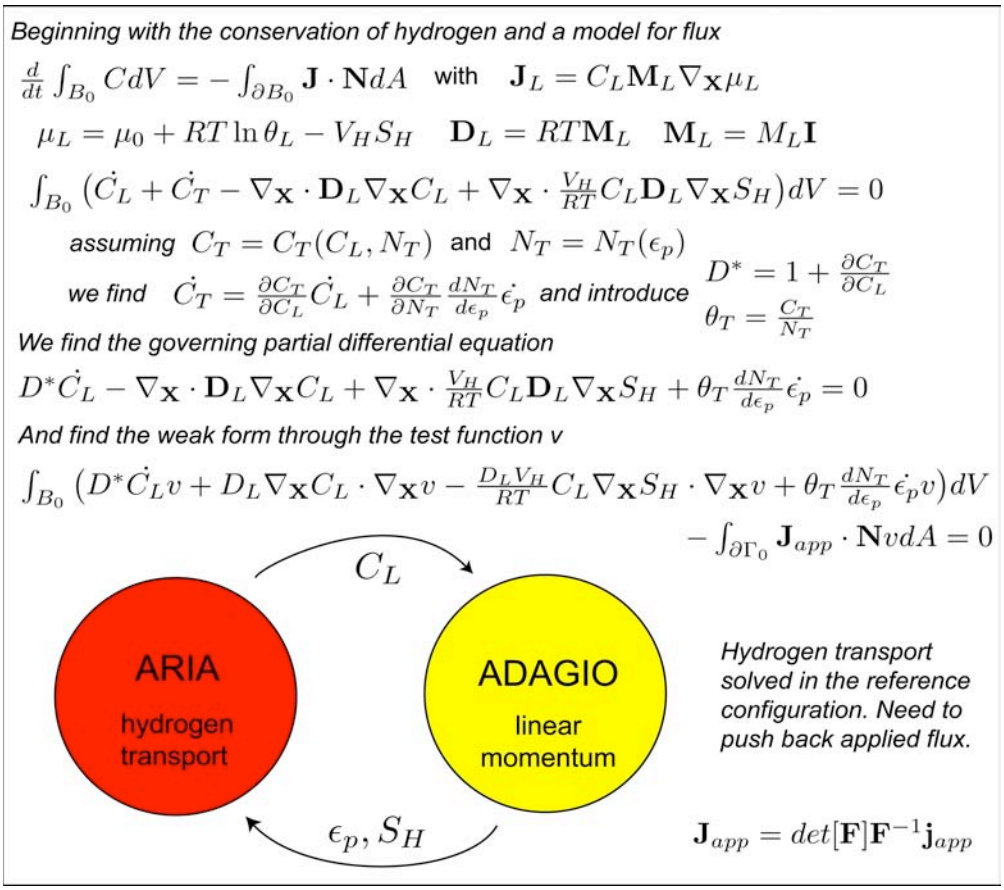

Figure 4.8. An outline of deriving the hydrogen transport partial differential equation and a schematic of the segregated coupling scheme between the Sierra codes Aria and Adagio. Hydrogen transport is solved in the reference configuration.

4.2.2 An examination of the hydrostatic stress ahead of a crack tip.

In order to obtain a better understanding of surface flaws that could be induced through environmental effects, edge defects were examined in a polycrystal. The implementation of Marin [30]with Voce hardening was employed. The evolution of slip in the flawed and surrounding grains was examined. An outcome of the study was that the hydrostatic stresses ahead of the crack tip were consistently greater than those predicted by J_2 plasticity. As previously noted, because the chemical potential is a function of the hydrostatic stress, those differences will affect hydrogen transport. Moreover, Gangloff has asserted that elevated stresses are needed to raise lattice and trapped concentration at the crack tip to justify proposed

mechanisms of embrittlement (eg., lowering cohesive strength) [31]. In seeking to obtain higher stresses hydrostatic stresses, Gangloff invokes strain-gradient plasticity. Through strain gradient plasticity and an assumed length scale, one can obtain hydrostatic stresses greater than 10 times the yield stress s_y. We note that for J_2 plasticity, the peak hydrostatic stress is ~ $5s_y$. We seek to show that elevated hydrostatic stresses can be the product of microstructure and one does not need to invoke strain-gradient plasticity. Leveraging the work of Dingreville [32], we employ both the crystal plasticity model and parameters (for nickel) for our model system. The idealized system of hexagons is noted in Figure 4.9(b). Although it does contrast the measured microstructure Figure 4.9(a), hexagonal grains provide a baseline for analysis. In both cases, the average grain size is 33 μm.

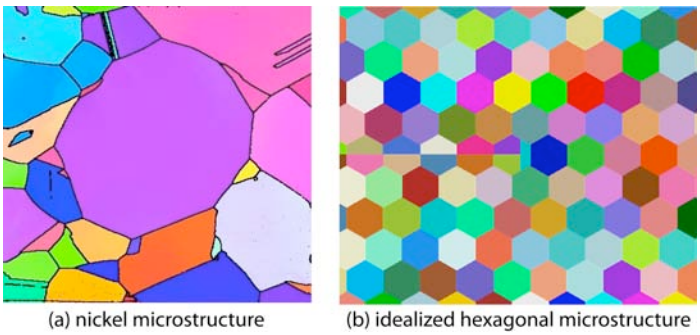

Figure 4.9. Comparison between measured (Dingreville, [32]) and synthetic microstructures. Both nickel microstructures have an average grain size of 33 μm.

To simplify the loading and maintain a known driving force, we elect to apply a K-field boundary condition. Given an applied stress intensity factor K and the location of the crack tip, we can apply a displacement field at the far-field (disk boundary) derived from the linear elastic fracture mechanics (LEFM) solution (Figure 4.10). Provided the plastic zone size is small compared to the disk radius and the majority of inelasticity is confined to the region of crystal plasticity, isotropic J_2 plasticity will provide a smooth transition and will reduce to isotropic elasticity at the far-field.

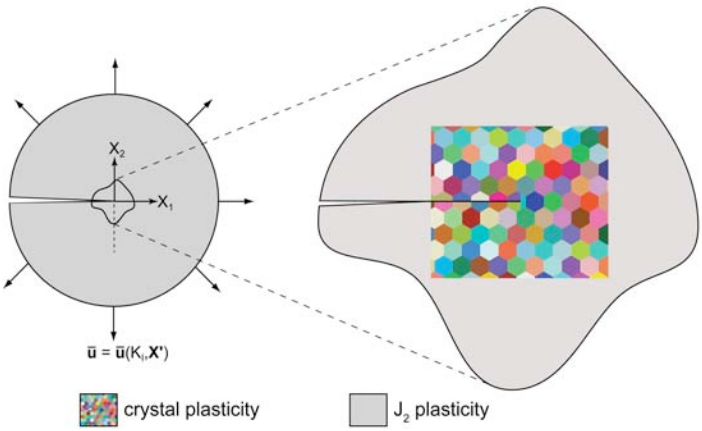

Figure 4.10. Applied, far-field K-field displacement boundary condition.

To confirm if our assumption regarding J_2 plasticity is valid, we examine the quantity of interest, the hydrostatic stress, ahead of the crack tip by varying the number of grains surrounding the crack tip. For this particular case, the grain size is 500 μm and the applied stress intensity is 89.7 MPa(m)$^{1/2}$. As shown in Figure 4.11, the peak stress occurs in the first grain. In Figure 4.10, a key attempts to orient the reader as to which randomly oriented grains are modeled with crystal plasticity. If the dotted line contains or intersects the grain, crystal plasticity with Taylor hardening was employed. Grains exterior to the dotted line are modeled with J_2 power-law hardening. In hopes of maintaining a consistent representation, we fit our power-law hardening model, $s_p = 46.1 + 327e_p^{0.358}$ (MPa), from the averaged macroscopic response of 100 randomly oriented cases for a 199 grain representative volume element [32]. As noted in Figure 4.1.3, all curves collapse beyond 2.5 mm, just beyond the crystal plasticity/J_2 interface. More striking, polycrystalline simulations beyond 1 hexagon (grain) oscillate around the J_2 solution (with a single grain). For this case, the first grain dominates the hydrostatic stress.

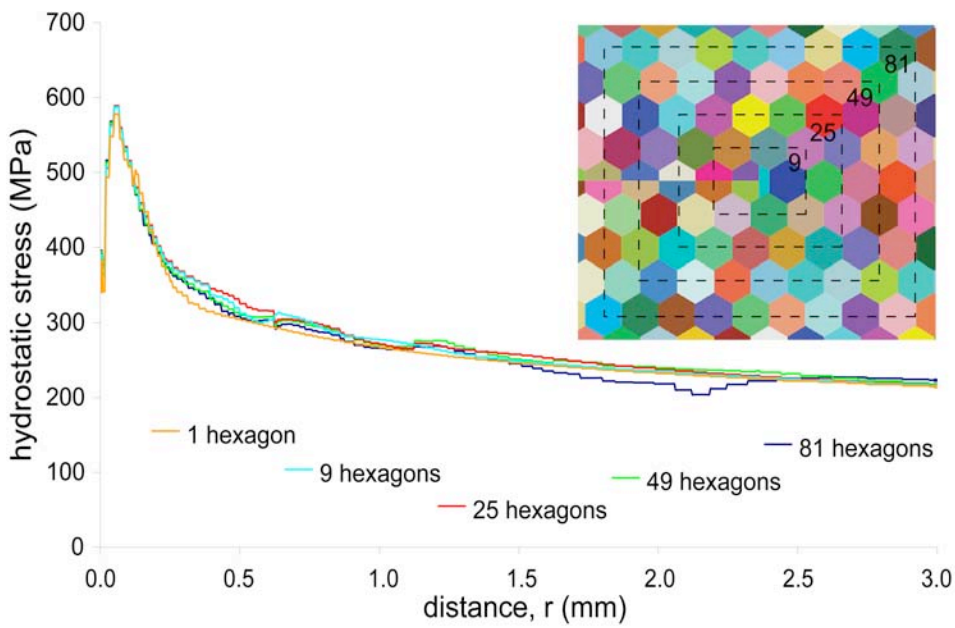

Figure 4.11. Variation in the number of polycrystalline grains around the crack tip. For this randomly orientated microstructure, added grains only perturb the solution. The simulated grain size is 500 μm.

We should also add that although local crystal plasticity does not have a length scale, we have introduced a length scale into the problem through both the chosen grain size l_d and the applied stress intensity K_I where $l_{app} \sim gK_I^2/s_y^2$ and g is a geometric factor (eg., 1/2p). If l_{app} is on the same order as l_d, we expect the solution to be more sensitive to microstructure – few grains will be sampled. In contrast, for $l_{app} >> l_d$, we expect the solution to be less sensitive to microstructure and more aligned with J_2 plasticity.

For lower stress intensities K_I = 36.5 MPa(m)$^{1/2}$, we compare crystal plasticity and J_2 power-law hardening for 81 grains (hexagons) having a grain size of 33 mm. For the case shown in Figure 4.12, the long crack solution mirrors previous observations for surface cracks. The hydrostatic

stresses ahead of the crack tip are significantly higher if one considers microstructure. To compare with previous works, we choose to identify the yield stress not through the chosen yield for the power-law fit, s_y = 46.1 MPa, but through 0.2% offset, s_y = 81 MPa. This confirms that for substantial hardening, J_2 yields a s_H/s_y ratio of ~5 while crystal plasticity yields a ratio of ~8. A snapshot of the hydrostatic stresses at the peak loading is also shown in Figure 4.1.5 and one can notice the non-uniformity of the hydrostatic stress field. We note that for this loading, l_{app} is extremely large and in the tens of mm (32 mm for g = 0.16) because the initial yield for pure nickel is small compared to structural metals. Nonetheless, even for $l_{app} >> l_d$, significant differences remain between the solutions.

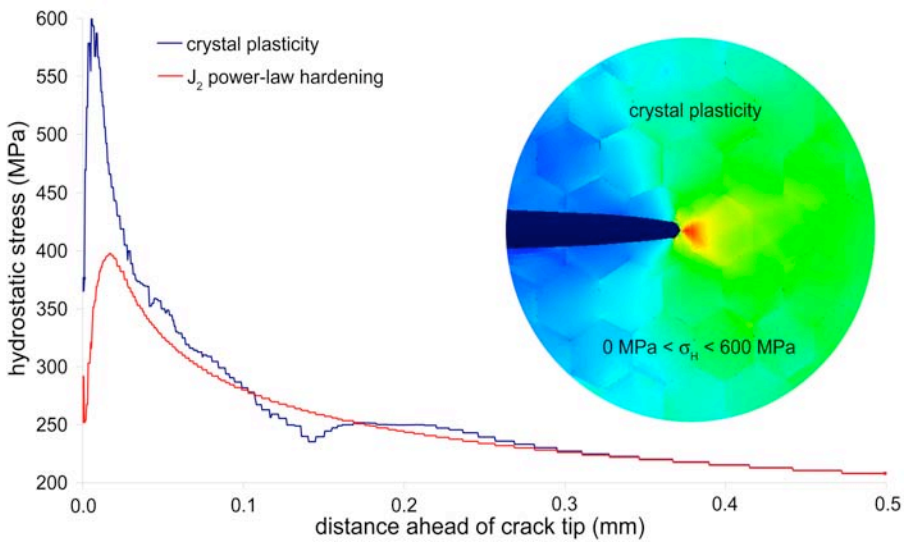

Figure 4.12. Differences in the hydrostatic stress field as a function of the modeling methodology. The simulated grains size is 33 μm.

4.2.3 Discussion and conclusions.

These initial findings show promise and reveal how the incorporation of microstructure can significantly alter the local crack tip fields. We should note that hydrogen transport is affected by the gradient of the hydrostatic stress. Near-tip gradients in the hydrostatic stress are significantly different between modeling methodologies (although we only show a 1-D slice). Additional non-uniformity also exists in the equivalent plastic strain and future coupled simulations of deformation and transport will determine the impact on both lattice and total hydrogen concentration; the source of hydrogen embrittlement. Like all efforts involving microstructure, we must also investigate ensembles of grain rotations and applied loadings (for constant grain size) to determine if the differences shown are statistically significant. We regret that the current findings, while interesting, are mostly speculative. Although we have exercised the Aria-Adagio coupling for relatively blunt notches, solving systems with large pressure gradients at crack tips might require stabilization. We do assert, however, that our speculations do derive from examining microstructure rather than attempting to build more complexity into a continuum model. It is our hope that coupled simulations of microstructure do confirm our hypothesis and improve our understanding of hydrogen embrittlement.

4.3. Systematically varied microstructures for model development and testing (L.N. Brewer (01814), J.D. Puskar (01822), B.L. Boyce (01813), C.C. Battaile (01814))

4.3.1 Introduction

As has been made clear in this report, the inclusion of microstructure in models for plasticity, crack nucleation, and crack propagation is critical to increasing the fidelity of these models. It is important that the microstructures used to develop and test these models be derived from actual experimental data. Unfortunately, experimental data that systematically changes the microstructure in metals and is appropriate for model development and testing is difficult to find. Many experimental papers only discuss a single grain size or crystallographic texture from a given heat treatment process. Experimental papers that do have a range of microstructures may use microstructures that are too complex for current level of plasticity models, e.g. multiphase materials, non-slip based deformation such as deformation twinning, etc.

This section of the report describes an effort to create a series of experimentally-derived microstructures that are designed to be used for model development. Cartridge brass (70 wt% copper, 30 wt% zinc) was chosen as the model system because of its crystallographic simplicity (face centered cubic), it phase simplicity (simple solid solution in the alpha phase), and its relative ease in processing for producing different grain sizes (cold rolled stock followed by annealing treatments). The brass material was processed such that a range of grain sizes from 1μm to almost a millimeter were produced.

In situ mechanical testing was performed on these brass samples to collect a series of data sets that tracked the microstructural evolution during plasticity for two different scenarios: monotonic, uniaxial tension and cyclic, uniaxial tension. A combination of *in situ* and *ex situ* electron backscattered diffraction (EBSD) were performed to track the change in the microstructure during the deformation. The resulting data sets can be used by plasticity, damage, and crack models to provide initial microstructures and to compare the results of the models with experiment.

4.3.2 Production of brass materials

Annealing treatments on cold-rolled, cartridge brass sheet-coil stock were used to produce a range of grain sizes and textures in the materials. The cold-rolled, cartridge brass stock (30% zinc) was procured from Eagle Brass Co. Individual sheets were cut from this stock and annealed in a combination of salt pots and furnaces to produce the annealing schedule found in Table 4.4. Tensile bars, as pictured in Figure 4.13 were cut from the annealed sheet using electro-discharge machining with the rolling direction along the tensile axis for all samples. The tensile bars were then prepared for EBSD-straining measurements by grinding and polishing both sides of the tensile bar to a modest finish level. One side of each sample was polished to at least a one micron finish. Some of the samples were then electropolished to achieve the best surface finish possible.

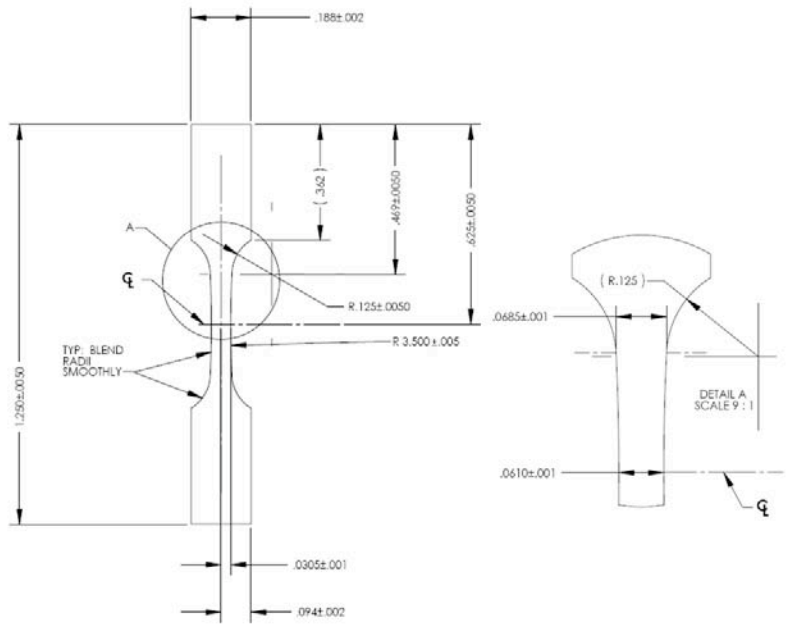

Figure 4.13. Drawing and image of tensile bar geometry. Dimensions are in inches.

The grain size of each sample was measured using EBSD. Lines scans were used for these measurements to ensure that a suitable number of grain segments, ideally greater than 500, were recorded. This goal was achieve for all but the largest two grain sizes which did not have a sufficiently large enough number of grains in the entire sample. The grain size data is also included in Table 4.11. In addition, this data allowed an assessment of the crystallographic texture in the samples. The recrystallized samples clearly had a texture with a s rolling plane and a <111> rolling direction. This texture became stronger as the grain size became larger. Examples of this recrystallization texture can be found in Figure 4.14.

Table 4.4 Heat Treatment Conditions and Grain Sizes for Tailored Brass Microstructures

Temperature	***Time***	***Grain Size (microns)***	
ºC	***hours***	***Mean with twins***	***Mean without twins***
400	***2***	***1.4***	***3.1***
400	***4***	***1.8***	***3.6***
425	***2***	***2.1***	***4.3***
450	***2***	***3.0***	***5.6***
450	***8***	***6.6***	***19.3***
450	***99***	***10.8***	***25.5***
600	***8***	***27.3***	***79.1***
800	***8***	***309.2***	***725.2***

450°C/8hrs

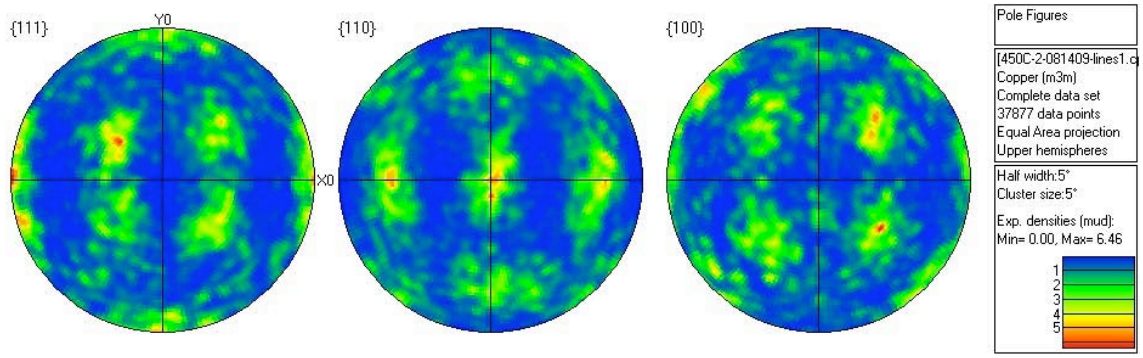

600°C/8hrs

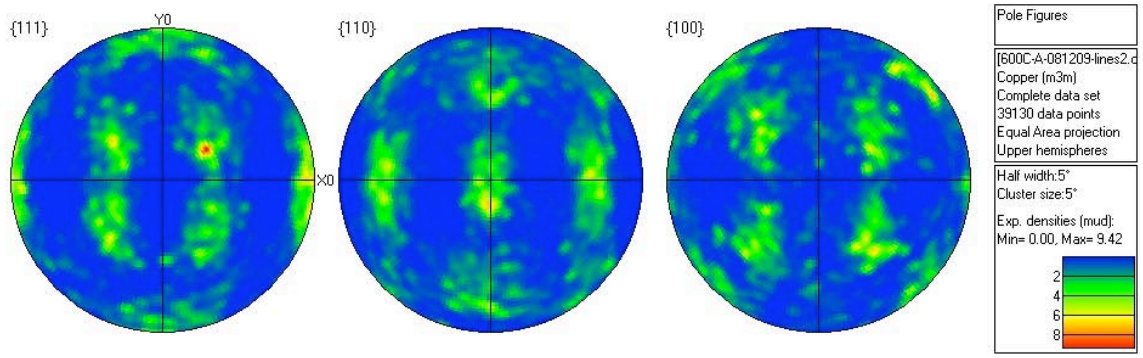

Figure 4.14. Pole figures from recrystallized brass as a function of grain size. (Note: x is the rolling direction and the tensile direction)

A uniaxial stress-strain curve was produced for brass bars at twelve different grain sizes. All of the models described in this report require a basic stress-strain curve to fit the parameters needed for the constitutive laws describing plasticity in the models. As would be expected, the yield strengths varied considerably over the range of grain sizes. This data was combined with the grain size data to generate a Hall-Petch plot (Figure 4.15) This plot displays the yield strength as a function of inverse square root of the grain size. Polycrystalline metals, in general, have a straight line behavior on a Hall-Petch plot. In Figure 4.15, this straight-line behavior is observed, but there are two different slopes depending upon whether the grain size measurements include twin boundaries or not.

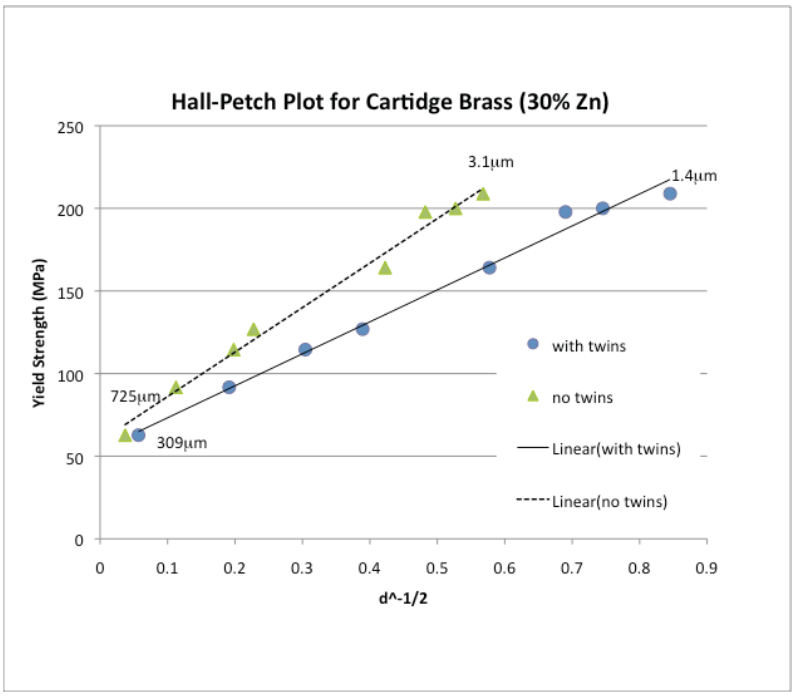

Figure 4.15 Hall-Petch plot for cartridge brass. The two sets of data represent grain size measurements taken with and without including twin boundaries.

4.3.3 Monotonic, uniaxial, tension experiments

In situ straining experiments were performed on three of the grain sizes from Table 4.4: 3.1, 5.6, and 25.5 microns (excluding twins). All of these experiments were performed using the new *in situ* straining stage described in section 2.1 on the Zeiss Supra 55 VP-FEG SEM using the HKL Channel 5 EBSD system. In all cases, the straining experiments were performed in a strain controlled manner, stopping at specified strain levels so that EBSD maps could be collected. The strain rate was nominally 10^{-3} at room temperature. The density of points was higher for the initial maps (at least 500x500 or 1000x1000 points) than for the maps at higher strain levels (200x200 to 500x500). The higher density of information in the initial maps was used to more faithfully recreate the microstructure in related simulations.

The systematic changes in the microstructure as a result of deformation are clear in the orientation and local intragrain misorientation maps (LIMIS) shown in Figure 4.16 and Figure 4.17, respectively. The interpretation of these maps has been discussed in more detail in section 2 of this report. The inverse pole figure maps in Figure 4.16 clearly show our ability to maintain the same area of the microstructure in the experiment as the strain level increases, although the total number of grain decreases as the strain increases as was previously discussed in section 2.3. While one can seem some rotation cause by the plastic deformation in Figure 4.16, other metrics are best used to visualize the deformation. The LIMIS metric used in Figure 4.17 is more sensitive to the amount of deformation-induced rotation on a grain by grain level. The LIMIS

metric is easily calculated for FEM results and may provide a good basis for quantitative comparison between experiment and simulation.

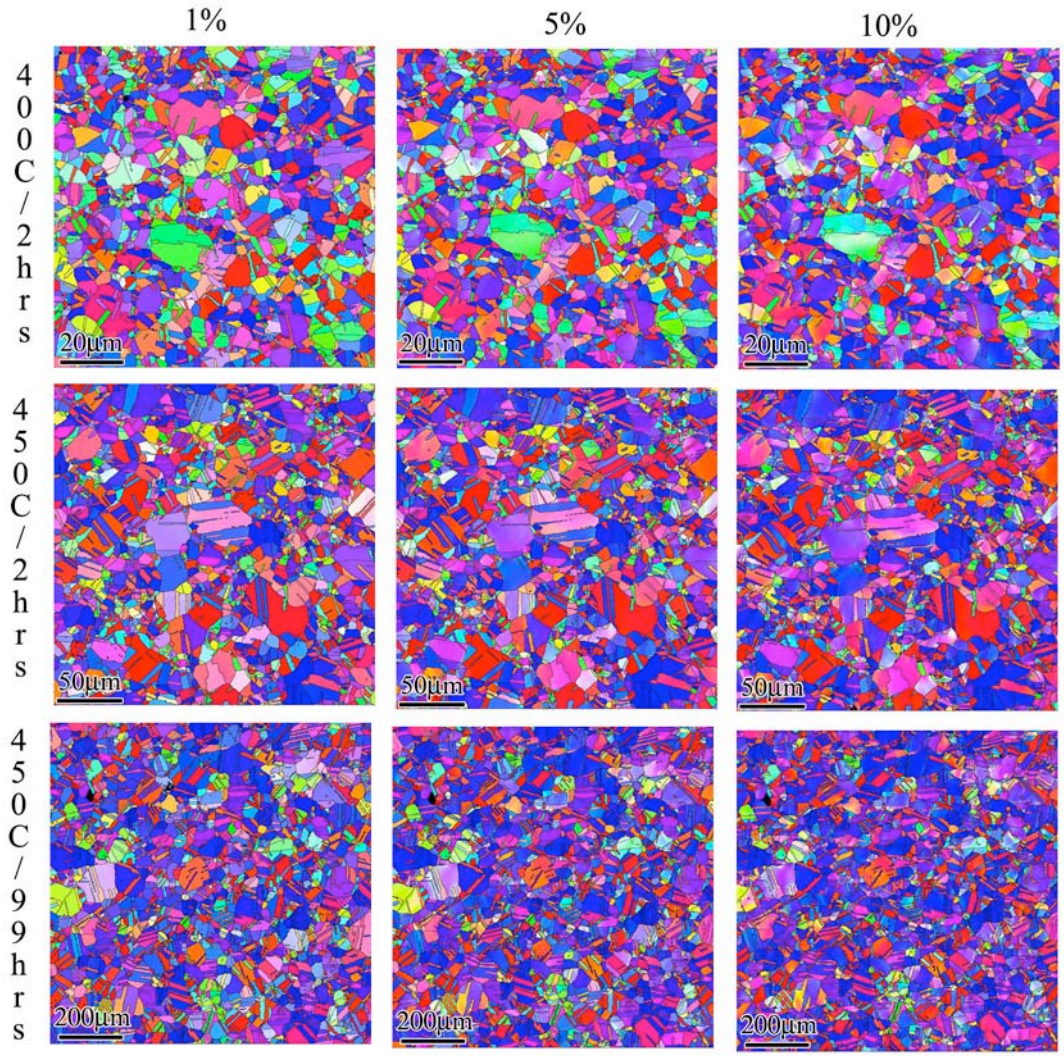

Figure 4.16 Inverse pole figure maps (with respect to x-tensile direction) for three grain sizes of brass strained to three different levels.

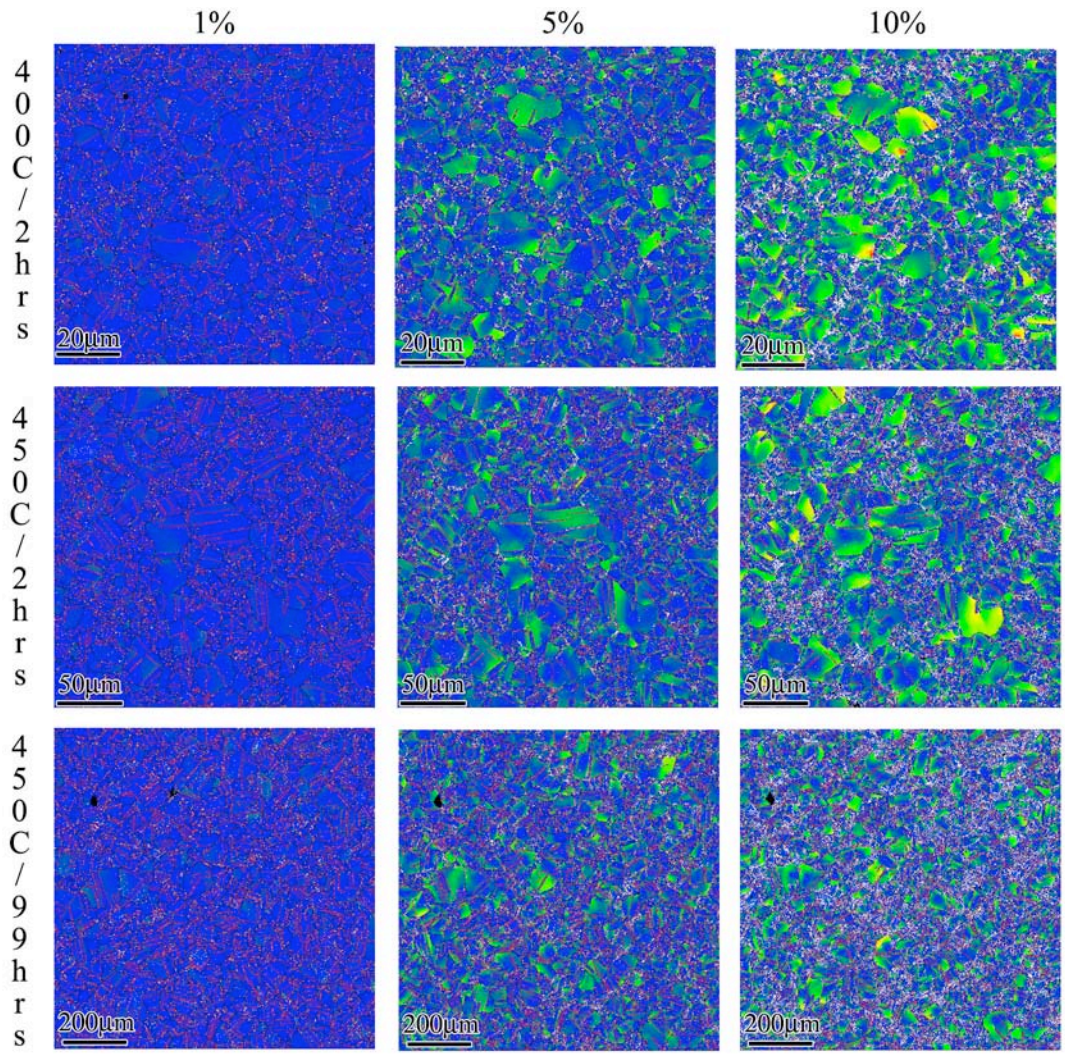

Figure 4.17 LIMIS plots for three grain sizes of brass strained to three different levels. For all figures, blue is 0º misorientation and red is 15º misorientation.

4.3.4 Cyclic, uniaxial, tension experiments

In order to examine the effects of cyclic deformation on the brass, polycrystalline microstructure, we performed ex situ mechanical tests combined with carefully coordinated microscopy. One of the primary manifestations of plasticity during cyclical loading is the development of slip steps on the surface of the sample. These steps grow as the cycles increase and can eventually lead to crack nuclei on the surface. Combined EBSD and atomic force microscopy (AFM) experiments have been used previously in the literature to examine step formation during cyclic loading. [33-35] For each of the grain sizes (3.1, 5.6, and 25.5 microns (excluding twins), samples were prepared by metallographic polishing, followed by electropolishing to achieve the smoothest surface possible. Three areas 100µm by 100µm were marked on each specimen using the FIB so that the same area could be examine before and after deformation (Figure 4.18). Orientation maps of the microstructure were collected from these marked areas prior to deformation. The samples were strained in uniaxial tension with a combination of cycles and strain amplitudes listed in Table 4.5. For all samples, the final strain

level was 5% engineering strain. After straining, the surfaces in the marked areas on each sample were profiled using AFM to measure the slip step heights and widths. (Figure 4.19) Finally, orientation maps were collected a second time on each marked area to examine the change in crystal orientation and misorientation after the straining experiment. (Figure 4.20)

The data from these elaborate experiments is still be analyzed, but we should be able to make strong connections between the change in microstructure (grain size and recrystallization texture), the change in the nature of the cyclic deformation (strain amplitude per cycle), and the resultant change in slip step formation. Because of the careful collection of microstructural and mechanical information throughout the process, we should be able to do simulations of the slip step formation on the surfaces of these microstructures in the future.

Table 4.5 Experimental Matrix for Cyclic Plasticity Experiments.

Grain Size (microns)	***Strain Amplitude (% strain) per Cycle x Number of Cycles***
3.1	***1 x 5***
5.6	***0.1 x 50***
25.5	***0.01 x 500***

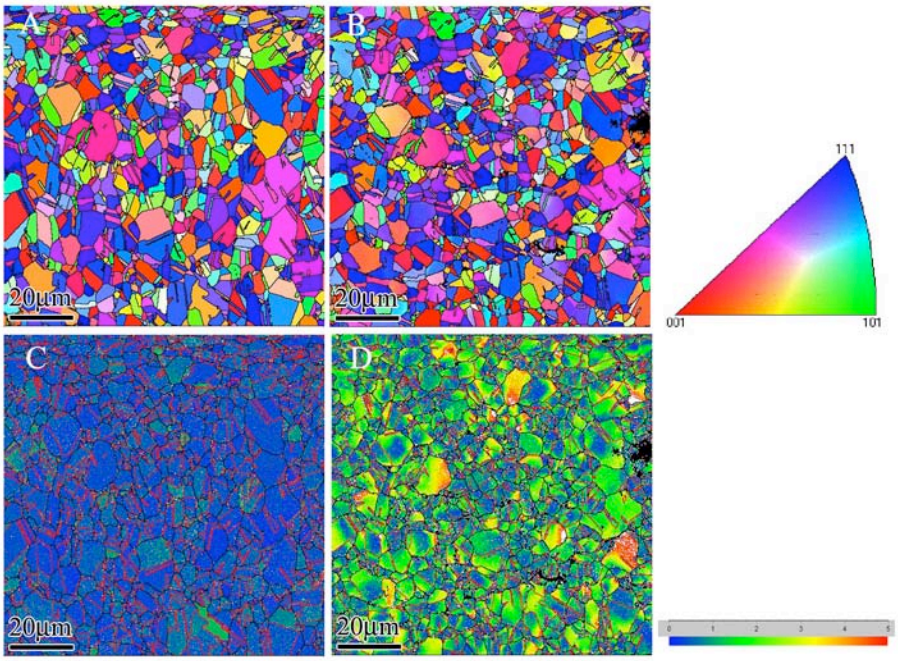

Figure 4.18 Orientation (inverse pole figure) and LIMIS maps for brass before (A and C) and after fatigue. The maps in this figure are for brass heat treated at 400ºC for 2 hours with 5 cycles at 1% strain per cycle for a total strain of 5%.

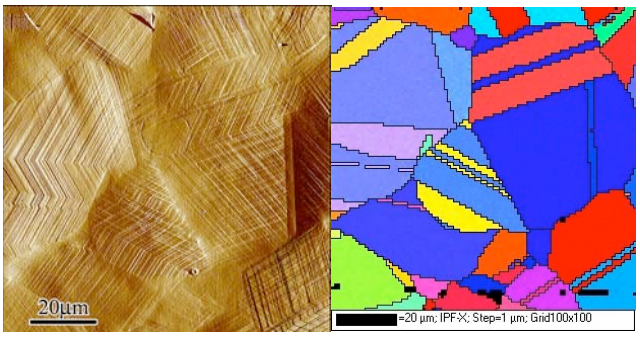

Figure 4.19 Combination of atomic force microscope (AFM) image (left, amplitude image) and EBSD orientation map (right, inverse pole figure) showing the same areas after fatigue of brass samples (450C, 2hrs) with 5 cycles at 1% strain per cycle.

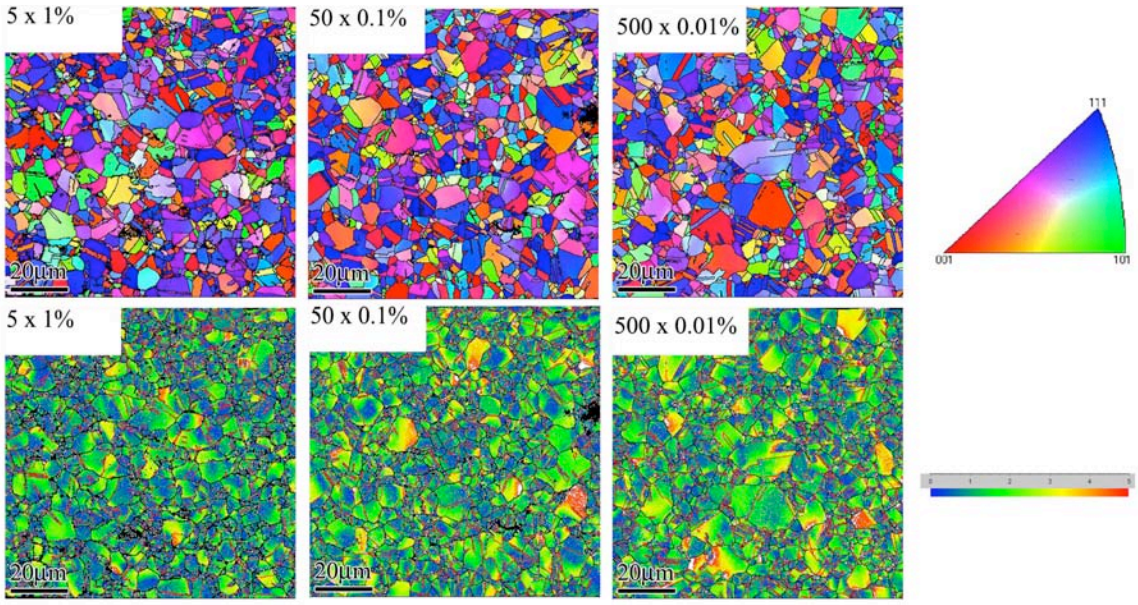

Figure 4.20 Orientation (inverse pole figure) and LIMIS maps for brass after fatigue. The maps in this figure are for brass heat treated at 400ºC for 2 hours.

Section 4 References:

1. Armstrong, P.J. and C.O. Frederick, A mathematical representation of multiaxial Bauschinger effect, in G.E.G.B. Report RD/B/N. 1966. p. 731.
2. Bari, S. and T. Hassan, Anatomy of coupled constitutive models for ratcheting simulation. International Journal of Plasticity, 2000. 16: p. 381-409.
3. Bari, S. and T. Hassan, Kinematic hardening rules in uncoupled modeling for multiaxial ratcheting simulation. International Journal of Plasticity, 2001. 17: p. 885-905.

4. Cailletaud, G. and K. Sai, Study of plastic/viscoplastic models with various inelastic mechanisms. International Journal of Plasticity, 1995. 11: p. 991-1005.
5. Chaboche, J.L., On some modifications of kinematic hardening to improve the description of ratcheting effects. International Journal of Plasticity, 1991. 7(661-678).
6. Chaboche, J.L. and D. Nouailhas, Constitutive modeling of ratchetting effects: Part I, Experimental facts and properties of classical models. Transactions of the ASME: Journal of Engineering Materials and Technology, 1989. 111: p. 384-392.
7. Dafalias, Y.E. and V.P. Popov, A model of nonlinear hardening materials for complex loading. Acta Mechanica, 1975. 21(173-192).
8. Kwofie, S., Cyclic creep behaviour described in terms of one parameter kinetic model. Materials Science and Engineering A, 2005. 392: p. 23-30.
9. McDowell, D.L., Stress state dependence of cyclic ratchetting behavior of two rail steels. International Journal of Plasticity, 1995. 11: p. 397-421.
10. Mroz, Z., On the description of anisotropic work hardening. Journal of the Mechanics and Physics of Solids, 1967. 15: p. 163-175.
11. Ohno, N. and J.D. Wang, Kinematic hardening rules with critical state of dynamic recovery: I. Formulation basic features for ratchetting behaviour. International Journal of Plasticity, 1993. 9: p. 373-389.
12. Sai, K. and G. Cailletaud, Multi-mechanism models for the description of ratchetting: Effect of the scale transition rule and of the coupling between hardening variables. International Journal of Plasticity, 2007. 23: p. 1589-1617.
13. Taleb, L., G. Cailletaud, and L. Blaj, Numerical simulation of complex ratcheting tests with a multi-mechanicsm model type. International Journal of Plasticity, 2006. 22: p. 724-753.
14. McDowell, D.L., Simulation-based strategies for microstructure-sensitive fatigue modeling. Materials Science and Engineering A, 2007. 468-470: p. 4-14.
15. Boyce, B.L., et al., Mechanical relaxation of localized residual stresses associated with foreign object damage. Materials Science and Engineering A, 2003. 349: p. 48-58.
16. Buchheit, T.E., G.W. Wellman, and C.C. Battaile, Investigating the limits of polycrystal plasticity modelling. International Journal of Plasticity, 2005. 21: p. 221–249.
17. Biffle, J.H., A three-dimensional finite element computer program for the nonlinear quasi-static response of solids with the conjugate gradient method, in SAND Report. 1987: Albuquerque, NM. p. SAND87-1305.
18. Flanagan, D.P. and T. Belytschko, A uniform strain hexahedron and quadrilateral with orthogonal hourglass control. International Journal for Numerical Methods in Engineering, 1981. 17: p. 597-609.
19. Holm, E.A. and C.C. Battaile, The computer simulation of microstructural evolution. Journal of Metals, 2001. 53: p. 20-23.
20. Dingreville, R., C.C. Battaile, and L.N. Brewer, Role of microstructure in multiscale crystal plasticity. International Journal of Plasticity, 2010: p. In preparation.
21. Sinha, S. and S. Ghosh, Modeling cyclic ratcheting based fatigue life of HSLA steels using crystal plasticity FEM simulations and experiments. International Journal of Fatigue, 2006. 28: p. 1690-1704.
22. Xie, C.L., S. Ghosh, and M. Groeber, Modeling cyclic deformation of HSLA steels using crystal plasticity. Transactions of the ASME: Journal of Engineering Materials and Technology, 2004. 126: p. 339-352.

23. Fisher, R.A. and Y. F., Statistical tables for biological, agricultural and medical research. 3rd ed. 1948, London: Oliver & Boyd.
24. Lemaitre, J. and J.L. Chaboche, Mecanique des materiaux solides. Dunod ed. 1985, Paris.
25. Suresh, S., Fatigue of Materials. 2nd ed. 1998, New York: Cambridge University Press.
26. Sofronis, P. and R.M. McMeeking, Numerical analysis of hydrogen transport near a blunting crack tip. Journal of the Mechanics and Physics of Solids, 1998. 37: p. 317-350.
27. Krom, A.H.M., Numerical modeling of hydrogen transport in steel. 1998, Delft University: Delft, The Netherlands.
28. Kumnick, A.J. and H.H. Johnson, Deep trapping states for hydrogen in deformed iron. Acta Metallurgica, 1980. 28: p. 895-911.
29. Oriani, R.A., The diffusion and trapping of hydrogen in steel. Acta Metallurgica, 1970. 18: p. 147-157.
30. Marin, E., On the formulation of a crystal plasticity model. 2006, Sandia National Laboratories: Livermore.
31. Gangloff, R.P., Critical issue in hydrogen assisted cracking of structural alloys., in Environment-Induced Cracking of Materials, S.A. Shipilov, et al., Editors. 2007, Elsevier. p. 141-165.
32. Dingreville, R., et al., The effect of microstructural representation on simulations of microplastic ratcheting. International Journal of Plasticity, 2009. Submitted.
33. Ma, J., AFM and OIM study of cyclic deformation behaviors of polycrystalline copper. Materials Science and Engineering a-Structural Materials Properties Microstructure and Processing, 2009. 501(1-2): p. 1-5.
34. Cretegny, L. and A. Saxena, AFM characterization of the evolution of surface deformation during fatigue in polycrystalline copper. Acta Materialia, 2001. 49(18): p. 3755-3765.
35. Frechard, S., et al., AFM and EBSD combined studies of plastic deformation in a duplex stainless steel. Materials Science and Engineering a-Structural Materials Properties Microstructure and Processing, 2006. 418(1-2): p. 312-319.

This page left intentionally blank.

5. CONNECTION TO THE FUTURE: INCLUDING MICROSTRUCTURAL PHYSICS INTO COMPONENT LEVEL PREDICTIONS USING PROBABILISTIC DESCRIPTIONS. (C.C. BATTAILE (01814), L.N. BREWER (01814), AND J.M. EMERY (01524))

This project has progressed the experimental and simulation tools sets used to study the evolution of the fatigue process at the microscale. While this project and recent research at other institutions has indeed increased our ability to include microstructures in predictions of plasticity, crack nucleation, and small crack growth; an important question remains:

What do we do with all of this data?

All too often those who work with microstructures are not able to connect their findings with those who study deformation and failure at the macroscale. There is an unfortunate barrier between those who study processes at the microscale and those who predict component behavior at the macroscale.

We suggest that the use of probabilistic descriptions of materials properties may provide a natural vehicle for transferring what is learned at the microscale to the macroscale in a way that can be effectively used for predicting damage and failure. Emery et al. have recently suggested a means for sampling flaw size statistically during a macroscale fatigue simulation. [1]

Recent work in a related late-start LDRD program (Battaile-138738) has performed proof-of-concept research to examine this approach. In this work, stress concentrators such as slots and cylindrical holes were placed into simulated tensile bars of brass with two questions in mind:

1.) How does the inclusion of a polycrystalline microstructure alter the predictions of stress and strain concentration from the predictions of continuum theory?
2.) How much does the local plastic response vary if many instances of the same parent microstructure are sampled?

As can be seen in Figure 5.1, the inclusion of a polycrystalline microstructure replaces the smooth, cosine-shaped lobes that would be expected at the ends of the slot with a plastic strain distribution that possesses an irregular pattern, manifesting in grains that are more suitably oriented for plastic deformation. This microstructurally influenced distribution will be comprised of strain levels that are higher and lower than expected by continuum theory. The result of these deviations from expectation is that predictions about phenomena such as crack nucleation will be incorrect.

Multiple realizations of the same microstructure will cause the extent of deviation from continuum theory to be probabilistic in nature. Any given, observed microstructure is only one sample from a parent, microstructural distribution. Parameters such as grain size distribution, orientation distribution, and misorientation distribution can be used to statistically characterize the microstructure. As these quantities are statistical, so will be the local plastic responses. Figure 5.2 shows the probability distribution for equivalent plastic strain generated by uniaxial tension on a plate with the strain concentrator pictured in Figure 5.1. The probability distributions were generated by performing the simulation many times (e.g. 50) with different,

but related microstructures. It is also clear from Figure 5.2, that changing the nature of the simulation in terms of hardening model (Voce or power law) or the boundary conditions applied (plane strain or bonded), results in a different probability distribution for the equivalent plastic strain generated. The fact that these changes in simulation parameters generate distinct distributions is particularly valuable because; using appropriate statistics, tests can be done do determine if the changes are statistically significant or not. In addition, one could perform sets of simulations using two different microstructures and then run statistical tests on the distributions to determine if the microstructural response is statistically different. This novel capability would add a much-needed dimension to the prediction of component response to a change in the underlying material.

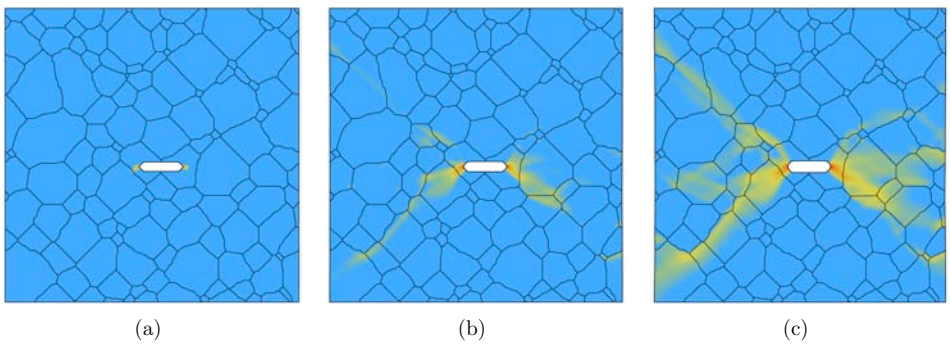

Figure 5.1. Distributions of local plastic strain in a slotted polycrystalline mesh deformed to a) 0.2%, b) 0.5%, and c)1.0% applied strain. The tensile axis was perpendicular to the length of the slot.

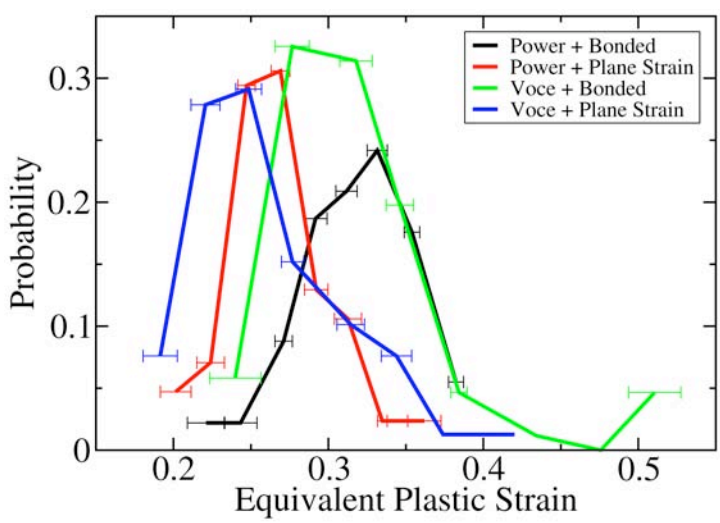

Figure 5.2. Histograms of the maximum plastic strain in a slotted polycrystalline mesh deformed to 1% applied strain. Simulations were performed using both plane strain and bonded boundary conditions (see text), and with both power law and Voce hardening equations. Each value of plastic strain corresponds to a distinct simulation with a random distribution of crystallographic orientations per grain.

Section 5 References:

1. Emery, J.M., et al., *DDSim: A hierarchical, probabilistic, multiscale damage and durabilty simulation system- Part I: Metholodgy and Level I.* Engineering Fracture Mechanics, 2009. **76**(10): p. 1500-1530.

This page left intentionally blank.

DISTRIBUTION

1	MS0346	E. David Reedy	01526
1	MS0346	James Cox	01524
1	MS0346	John Emery	01524
1	MS0372	Eliot Fang	01524
1	MS0431	John Pott	00511
1	MS0747	Timothy Bartel	06774
1	MS0885	Justine Johannes	01810
1	MS0886	Joseph Puskar	01822
1	MS0886	Bonnie McKenzie	01822
1	MS0889	Luke Brewer	01814
1	MS0889	Corbett Battaile	01814
1	MS1070	Channy Wong	01524
1	MS1411	Elizabeth Holm	01814
1	MS1411	Allen Roach	01814
1	MS1411	Christopher Weinberger	01814
1	MS9042	Jay Foulk	08246

2	MS9018	Central Technical Files	8944
2	MS0899	Technical Library	4536 (eletronic copy)
1	MS0123	D. Chavez, LDRD Office	1011

Sandia National Laboratories